ENGINEERING OF SURFACE MICROSTRUCTURE TRANSFORMATIONS USING HIGH RATE SEVERE PLASTIC DEFORMATION IN MACHINING

by

Sepideh Abolghasem

B.S., Sharif University of Technology, 2006

M.S., University of Pittsburgh, 2011

Submitted to the Graduate Faculty of

the Swanson School of Engineering in partial fulfillment

of the requirements for the degree of

Doctor of Philosophy

University of Pittsburgh

2015

UNIVERSITY OF PITTSBURGH

SWANSON SCHOOL OF ENGINEERING

This dissertation was presented

by

Sepideh Abolghasem

It was defended on

May 19, 2015

and approved by

M. Ravi Shankar, Ph.D., Associate Professor, Department of Industrial Engineering

Bopaya Bidanda, Ph.D., Ernest E. Roth Professor and Chairman, Department of Industrial Engineering

Roberto Zarama, Ph.D., Professor, Department of Industrial Engineering, Universidad de los Andes, Bogotá, Colombia

Jayant Rajgopal, Ph.D., Professor, Department of Industrial Engineering

Raha Akhavan-Tabatabaei, Ph.D., Associate Professor, Department of Industrial Engineering, Universidad de los Andes, Bogotá, Colombia

Youngjae Chun, Ph.D., Assistant Professor, Department of Industrial Engineering

Dissertation Director: M. Ravi Shankar, Ph.D., Associate Professor, Department of Industrial Engineering

ENGINEERING OF SURFACE MICROSTRUCTURE TRANSFORMATIONS USING HIGH RATE SEVERE PLASTIC DEFORMATION IN MACHINING

Sepideh Abolghasem, PhD

University of Pittsburgh, 2015

Engineering surface structures especially at the nanometer length-scales can enable fundamentally new multifunctional property combinations, including tunable physical, mechanical, electrochemical and biological responses. Emerging manufacturing paradigms involving Severe Plastic Deformation (SPD), for manipulating final microstructure of the surfaces are unfortunately limited by poorly elucidated process-structure-performance linkages, which are characterized by three central variables of plasticity: strain, strain-rate and temperature that determine the resulting Ultrafine Grained (UFG) microstructure. The challenge of UFG surface engineering, design and manufacturing can be overcome if and only if the mappings between the central variables and the final microstructure are delineated.

The objective of the proposed document is to first envision a phase-space, whose axes are parameterized in terms of the central variables of SPD. Then, each point can correspond to a unique microstructure, characterized by its location on this map. If the parametrization and the population of the datasets are accurately defined, then the mapping is bijective where: i) realizing microstructure designs can be reduced to simply one of tuning process parameters falling within the map's desired subspaces. And, inversely, ii) microstructure prediction is directly possible by merely relating the measured/calculated thermomechanics at each point in the deformation zone to the corresponding spot on the maps.

However, the analytic approach to establish this map first requires extensive datasets, where the microstructures are accurately measured for a known set of strain, strain-rate and

temperature of applied SPD. Although such datasets do not exist, even after the empirical data is accumulated, there is a lack of formalized statistical outlines in relating microstructural characteristic to the process parameters in order to build the mapping framework. Addressing these gaps has led to this research effort, where Large Strain Machining (LSM) is presented as a controlled test of microstructure response. Sample conditions are created using LSM in Face Centered Cubic (FCC) metals, while characterizing the deformation using Digital Image Correlation(DIC) and Infrared(IR) thermography. Microstructural consequences such as grain size, subgrain size and grain boundary responses resulting from the characterized thermomechanical conditions are examined using Electron Back-Scattered Diffraction (EBSD). Once empirical data is generated across the broad thermomechanical conditions, reliable microstructure maps are populated. This characterization can help understand surface microstructures resulting from shear-based manufacturing processes such as turning, milling, shaping, etc. that are created under analogous thermomechanical conditions.

Keywords: microstructure characterization, ultrafine grain microstructure, severe plastic deformation, high speed deformation.

TABLE OF CONTENTS

LIST OF TABLES

LIST OF FIGURES

PREFACE

To my mother, Azemat

I would never have been able to finish this work without the excellent guidance of Dr. Ravi Shankar and would like to express my deepest gratitude for his caring, patience, and providing me with a wonderful atmosphere for doing my research. I am genuinely grateful to Dr. Bopaya Bidanda for his warm support during the very hard times of this journey. His cares, even remotely, brought this work towards a completion. My special and heartily thanks to Dr. Roberto Zarama for his unreserved help, encouragement and direction. I am also very grateful to Dr. Raha Akhavan-Tabatabaei for her kind and insightful instruction. Moreover, thank you to Dr. Youngjae Chun and Dr. Jayand Rajgopal for being part of my committee, and inspirations in many ways.

I wish to convey my dearest regards to Albert Stewart for his help and patience while I was learning to work with Scanning Electron Microscope and X-Ray Diffraction machine. I am also indebted to my colleagues and friends for inspiring and supporting me in countless ways. Special thanks to Dr. Shashank Shekhar for endless help and inspirations during this time, to Dr. Saurabh Basu who as a good friend, was always willing to help and give his best suggestions and constructive advice. Thanks to Marzyeh Moradi, my dearest friend, for her support and assistance, even from long distance.

My most heartfelt thanks go to my family, my mother and two elder sisters. They were always supporting and encouraging me with their best wishes. I could not have finished the work without my mom's unconditional love and support. I will always be indebted to my father who motivated me to believe in myself, through good times and bad. I wish he were around to witness this.

1.0 MOTIVATION AND LITERATURE REVIEW

The microstructure resulting from Severe Plastic Deformation (SPD) is the critical element that manifests a suite of mechanical and functional properties of the final product in an array of conventional and emerging manufacturing processes, including surface generation by SPD in machining, Friction Stir Processing, Equal Channel Angular Pressing, etc. [83, 138, 140, 137]. The final microstructure includes enhanced mechanical and functional properties wherein, surface microstructure plays a principal role in determining product performances such as fatigue life, wear behaviour, or corrosion resistance that define the life-cycle of the components in an array of critical engineering applications. Henceforth, engineering material properties is typically accomplished by surface modification using extensive secondary processing to achieve the desired combination of the physical, chemical, biological and mechanical properties. Towards this effort, for example, discrete coatings of hard layers are used in metallic bone implants to enhance wear properties in joint replacements. Each year, an extensive deployment of such implant occurs in hip and knee replacements besides dental implants [1].

These enhanced mechanical and physical attributes are directly subjective to the resulting surface microstructures from SPD such as grain size, subgrain size, grain boundary characteristics, dislocation densities, etc. The followings will enumerate instances on how these microstructure characteristics will affect multifunctional properties in detail.

Recent discoveries are focused on materials at the Ultrafine Grain (UFG) scale, especially nano-meter length scales that have proved to include enhanced properties like tunable physical, mechanical, electrochemical and biological responses, comparing to the coarse grained counterparts. Consequently, efforts are made to modify the bulk microcrystalline materials in order to create integral regions of the UFG structure, within few tens of micrometers of the surface. It has been shown that a nanoscale grain size microstructure even at nominally smooth surfaces in biocompatible metals, for example in stainless steels and Ti alloys, improve performance for applications such as implants, without requiring any further surface treatments. This enhancement involves amplification of adhesion, spreading and interconnectivity of preosteoblasts [40, 87, 99, 39], osteoblasts [100], fibroblasts [139], mesenchymal stem cells [38], etc. in nanoscale materials comparing to coarser grained microcrystalline counterparts [50, 98, 63, 13, 86, 104, 106, 110, 93]. This discovery can be utilized as a substitution of traditional techniques that rely on complex surface modification following fabrication, including the integration of biocompatible coatings with difficult-to-control mechanical resilience. More specific enhanced properties of nanoscale materials are also proved as a result of grain refinement. For example, nanocrytalline Fe-Cr alloy with a nominal Cr content of 10 wt% has shown improved oxidation resistance from that of microcrystalline alloy of similar chemical composition [50]. Microstructure state is demonstrated to be a significant factor on corrosion rate of pure Mg as well and improves as a function of grain size, while at the same time enhancing mechanical properties [98]. As another example, ultrafine-grained (UFG) materials have shown enhance metabolic activity, which is investigated in austenitic stainless steel to enrich cellular response especially for bone growth [13]. Fatigue life is likewise proved to be improved for steel with nanograined layer less than 100 micrometers in thickness besides enhanced wear properties and decreased friction coefficient in nanostructured surface layer of Fe [106, 93]. Furthermore, improved characteristics resulted from grain refinement in the cellular response of the substrates at the nano scale and coarse scale are discussed as the enhanced characteristic in the biological responses such as cell-substrate interaction for preosteoblasts on nanostructured and ultrafine grained steels [86].It is demonstrated here that metallic materials with UFG structure and in particular nano-scale grains provide surfaces with different properties due to high fraction of grain boundaries with

high free energy. Such features help to amplify cell adhesion, viability and interconnectivity of preosteoblasts in cell cultures. Besides improved performance resulting from nano-scale grain surfaces in stainless steels and Ti alloys, considerable oxidation resistance of Fe-Cr alloys are conferred and validated in nanocrystalline structure [104]. Electrochemical passivity of nanograined surfaces is another advantage emerging from empirical experiments of engineering materials which is also relevant in transportation and energy industries due to durable reliability against environmental corrosion. These functional properties, improving hardness of nanograined materials, are result of Hall-Petch effect[118, 117] that enhance fretting and wear resistance [59]. Note that such newly discovered multifunctional properties are all inherited from UFG surface crystal/grain structure.

Furthermore, the microstructure of typical crystalline metals is primarily characterized by defect structures including grain boundaries, sub-grain boundaries and dislocation distributions, whose quantitative characteristics often determine strength [135], formability [73], electrochemical response, biological compatibility [97] and response to radiation. For example, strength of a material, represented by Hardness value, is inversely proportional to the square root of the grain size in accordance to the Hall-Petch relation [51, 102], which is supplemented by contributions from the subgrain hardening that is in proportion to the inverse of the subgrain size and is further enhanced by Taylor hardening as being proportional to the square root of the dislocation density [130]. Clearly, even something as simple as control of flow strength requires the delineation of the composite contributions from the various types of defect structures that emerge during plastic deformation. Analogously, manipulation of functional attributes such as electrochemical properties also requires precise control over the defect structure, which in turn determines the mechanisms of passivation, corrosion etc. [85].Also, recent results indicate that fraction of Low Angle Grain Boundaries (LAGBs) in deformed microstructure is related to the thermal stability of nanostructured materials (unpublished results) and further systematic studies are underway to provide concrete and conclusive evidence for the same. There are, however, other phenomena that are well known to be directly related to grain boundary characteristics, like diffusion, energy and mobility [55, 20, 124, 125, 56, 48]. It is known that diffusivity is much faster through High Angle Grain Boundaries (HAGBs) and much lower through LAGBs, while mobility

of HAGBs is much higher than LAGBs and this difference in properties can be exploited to design components with specific application in mind. For instance, if high diffusivity is required in a material, processing conditions can be set which provide HAGB dominated microstructure, which in turn will aid high diffusivity. This can be particularly useful in manufacturing components like gears, where carbon needs to be diffused on the surface for high strength. Thus, high diffusivity would allow better penetration of carbon and hence higher strength up to greater depths of the gear tooth, which can substantially increase its life and durability.

These discoveries about the superior properties of the deformed materials have motivated the pursuit of the present research study to engineer surfaces with tunable multifunctional properties. Manufacturing researchers have predominantly remained focused on the metrology and modelling of the surface geometry, roughness [133], mechanics of material removal, and the dynamics of the cutting forces [119] and there exists holistic data and knowledge gaps in understanding surface microstructures and crystallography. These gaps can be bridged by establishing a framework for surface microstructure control offering a powerful tool for engineering multifunctional UFG surfaces. Towards this objective, previous efforts have demonstrated that Severe Plastic Deformation (SPD) is an established direction to create fully-dense bulk UFG crystalline materials by imposing very large shear strains ($>> 1$). On the basics of principles of physical metallurgy, it can be concluded that SPD necessitates dramatic microstructure transformations involving the accumulation of abnormally high-defect densities in the deformation zone. These defects include large dislocation densities that rearrange into subgrain and grain boundaries to form ultrafine grains directly from the microcrystalline state [137]. Hence, the microstructure from SPD processes such as surface generation by SPD in machining is expected to be undergone high refinement to induce the accommodation of high defect densities [122].

Much of the SPD literature has often focused on the achievement of the greatest possible levels of grain refinement to maximize the weight specific strength [138]. However, it has become increasingly apparent that the spectrum of realizable microstructures is not just a function of the severe strains, but can be further broadened by probing a wide range of strain-rates and deformation temperatures. For example, Dynamic Plastic Deformation (DPD)

involving the imposition of large strains at high strain-rates in compression can achieve a switch-over from typical ultrafine grained microstructures to nanotwinned structures [151]. Similar behaviour has been observed in High-Rate Severe Plastic Deformation (HRSPD) in simple shear, which can result in microstructures that are either nanotwinned [28], have multimodal grain size distributions [123] or are with tunable grain boundary structure/energies as one-to-one functions of severe plastic strain, strain-rate, and temperature [121].

Microstructural response is relatively well understood under the imposition of low strain-rate ($< 10^2\ /s$), and moderate levels of strain ($<< 1$). Standard protocols have also been established for gauging the constitutive response in subsets of dynamic deformation regimes. These include the Hopkinson bar test (high strain-rate $> 10^3\ /s$, low strain < 1), and the hot torsion test (typically, moderate strain-rate $< 10^2\ /s$, high strain > 10) [132, 76, 79].In the regimes characterized by these established protocols, there have been several efforts aimed at understanding the trajectories of microstructure refinement across the strains, strain-rates, and temperatures [132, 78, 80, 65, 114, 108, 148]. However, there is a lack of understanding of the dynamic microstructure transformations in the process regimes excluded by these protocols, especially in the high strain (> 1), and high strain-rate ($> 10^2\ /s$) states. Bridging a knowledge-gap in this thermomechanical processing regime is particularly useful in manufacturing research, given its prevalence in surface generation by the ubiquitous metal cutting, machining processes as well as in emerging friction stir welding/processing technologies.

Surfaces from machining are inherited from a zone of SPD involving large strains (1–10) at high rates ($10 - 10^3\ /s$) and coupled temperature rise [119, 127] and according to literature [92, 144, 134, 8], SPD in machining can lead to UFG including nano-sale surfaces that manifest the recently discovered, aforementioned functionalities, such as enhanced biological, electrochemical and mechanical properties. Thus, it can be concluded that machining is a proper microstructure engineering tool to create UFG surfaces. However, despite such empirical anecdotes, due to complexity, when simultaneous severe shear strains, high strain-rates and temperatures are encountered, characterization of the central variables has proved to be limited and often obscured by poor process-structure-performance linkages hence offering the challenge of transcending these paradigms. For another reason, if the challenge of understanding the process-structure-performance relationships in this peculiar niche of

deformation is overcome, it may be possible to skip secondary processing steps to endow products with novel functional properties inherited from surface nanograined states, directly during the product fabrication steps.

Further to above shortcoming in understanding the complex trajectories following the interactive effects of severe shear strains, strain-rates and temperatures, is the hardening behaviour in this peculiar deformation range which is not yet clearly investigated. Work hardening stages based on dislocation storage and recovery mechanisms are almost thoroughly described at low strain (< 0.5) by dislocation theory, which are developed by Taylor [131], Seeger [113], Hirsch [15] and Kuhlmann-Wilsdorf [69] via numerical theories to establish the parabolic stress-strain curve. Constitutive models are proposed for low strain but high strain-rate processes such as those proposed by Harding [54], Follansbee and Kocks [41], Zerilli and Amstrong [150]). However higher plastic strains (> 2) are ensued by complex dislocation relations via formation of subgrains and inhomogenities [115] which are referred to as Stage IV of work hardening by Brown [23]. In this unique niche of deformation, the hardening behaviour is not completely investigated, which adds to the unanswered questions towards understanding of the deformation mechanism in high rate severe plastic deformation. It is anticipated that the current research work can help elucidating the hardening behaviour at high strain, high strain-rate and the coupled temperature, which would lead to fundamentally new insights in future.

2.0 PROBLEM STATEMENT

The microstructure evolution under interactive effects of severe shear strains, high strain-rates and the coupled temperature rises often follows complex trajectories, which have not been thoroughly examined to date. The essence of encapsulating the critical, yet overlooked process-structure linkages in this regime (high strain, high strain-rate) can easily be discernible by visualizing the opportunity to manipulate process and product outcomes. This advance can be generalized to processes that involve severe plastic deformation, including surface generation by SPD in machining, Friction Stir Processing, Equal Channel Angular Pressing, etc. For example, the surface that is left behind from machining-based processes such as milling, turning, drilling, etc. are inherited from a shear deformation field that is characterized by precisely such thermomechanical conditions. The functional and mechanical properties of the resulting ultrafine-grained (UFG) surfaces that encompass a vast majority of engineering components would then be directly impacted by the microstructural transformations characterizing these conditions.

Although it has been demonstrated that UFG surfaces with multifunctional properties can be created using SPD in machining, how the process parameters relate to these characteristics is still not completely understood. Therefore, if such a framework as for engineering UFG surfaces using machining-based manufacturing systems can be developed, the potential implications can be revealed seamlessly. For instance, this tool can be utilized to create surfaces with custom designed nanograins, favourable texture, and dislocation content and thus, enabling to directly engineer surfaces to exploit the unique phenomena operative at these desirable conditions.

Given this importance, the premise of current research is to resolve the dynamic microstructure transformations in the process regimes excluded by previously established pro-

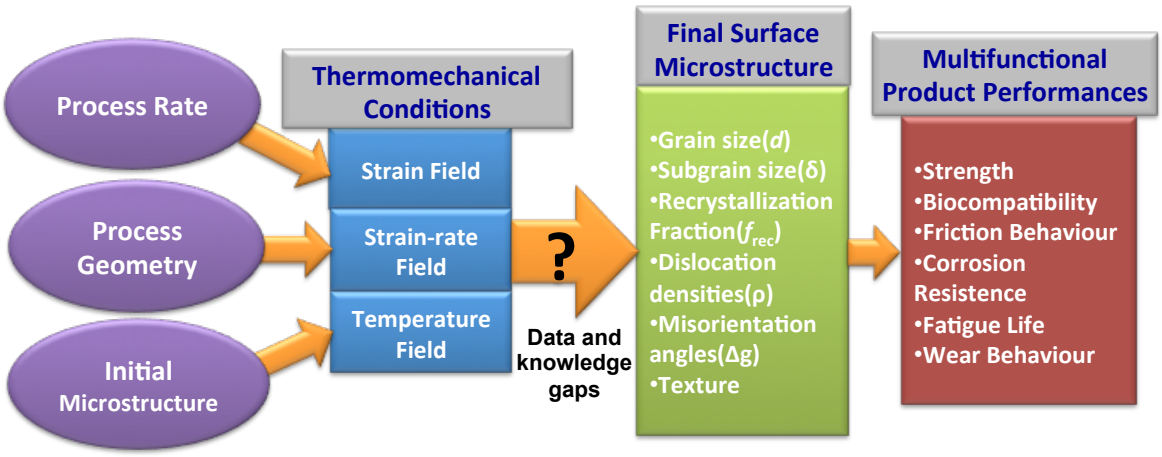

Figure 1: Conceptual links relating process parameters to product performance in machined components.

tocols, especially in the high strain (> 1), and high strain-rate ($> 10^2$ $/s$) states and their coupled temperature rises. We consider machining to be the solution here as it offers the exact required thermomechanical conditions besides the realizable potentials for creating UFG surfaces in manufacturing systems. Motivated by this, it is crucial to first develop a metrological framework for characterizing the resulting nature of machined surfaces, and secondly, create process-microstructure mappings that relate surface microstructures to machining parameters.

Towards this effort, a two-fold conceptual gap exists relating deformation parameters to the final microstructures in machined components as shown in Figure 1, data gap exists in providing a comprehensive set of empirical data as there is lack of quantitative studies of the UFG surfaces generated by machining. Apart from this, another gap exists in what is understood so far about the deformed surface microstructures following machining. Even on the limited empirical data available on the deformed surface created by machining; we lack a formalized framework for relating microstructural characteristics to the machining parameters.

While the machining process itself is a simple framework, characterizing the resulting surface using quantitative modern electron microscopy is complicated. Severe plastic defor-

mation imposed by machining, like all plastic deformation processes, is completely characterized by the four dynamically central variables: strain(ϵ), strain-rate($\dot{\epsilon}$), temperature(T) and the microstructural fields, which is uniquely defined as a function of deformation geometry, initial microstructure, and deformation rate. It is the complicate interactions among the deformation variables that result in the process outcomes which can be quantified if and only if the fields of the central variables are well defined. In next section, the research questions, associated with the proposed problem here, will be discussed in detail.

2.1 RESEARCH QUESTIONS

Performing SPD by machining as a tool for engineering UFG surfaces requires direct examination of the central variables, which is elusive when severe shear strains, high strain-rates and temperatures are simultaneously encountered in a small deformation region. This obstacle has complicated the understanding of microstructure transformation, resulting from such thermomechanics of deformation. Though, it offers the challenge to understand the underlying fundamental physical principles in the process-structure-performance triad. Such efforts will generate the subsequent **Questions**:

Q1: How to collect useful empirical data in machining response test on the resulting microstructure to develop the interconnections among the thermomechanics of deformation?

Q2: How to model the microstructure characteristics resulting from SPD in machining in order to be able to create the physical-based mappings?

Q3: What are the mappings among machining parameters and its thermomechanical SPD conditions to the resulting surface microstructure such as grain size (d), subgrain size(δ), recrystallization fraction (f_{rec}), dislocation density(ρ), misorientation angles (Δg), texture, and other multifunctional properties?

In order to adequately address above critical questions and to realize the substantial microstructural transformations in the peculiar niche of simple shear and high rate severe deformation through SPD in machining, a material response test is needed to be developed allowing for the following **Requirements**:

R1: Controllable experimental procedures, where we can assure that the geometry remains essentially isomorphic across the entire range.

R2: Convenient imposition of simple shear strains in the range of $1 - 10$ and strain-rates in the range of $10 - 10^3$ $/s$.

R3: Possibility to impose a wide-ranging temperature in the deformation zone - typically ranging from near ambient to above one-half of the melting temperature.

R4: As a reliable test method, the geometry of deformation should allow for a direct and *in situ* measurement of the strains, strain-rates and temperatures.

R5: Ability to measure and perform analytical microstructural characterizations, which offers subsequent analysis to understand the quantitative aspects of the resulting grain structure as a function of the thermomechanics of deformation.

2.2 OBJECTIVE AND SPECIFIC TASKS

According to above questions, the core objective of the present research can be summarized in the statistical characterization of the resulting microstructure to map machining parameters to multiple response variables. An alternative solution, presented here, is to create a phase-space, whose axes are parameterized in terms of the central variables of SPD: strain (ϵ), strain-rate ($\dot{\epsilon}$) and temperature (T) and material-dependent constants. Then, each point (or subspace) on this space would correspond to a unique microstructure, characterized by its location on this map. If the parametrization and the population of the datasets are accurately delineated, then the mapping is bijective where: (i) microstructure (X) prediction is directly possible by merely relating the measured/calculated thermomechanics at each point in the deformation zone to the corresponding spots on the microstructure maps as $X = F(\epsilon, \dot{\epsilon}, T, MDP)$ where X denotes the quantified final microstructure such as grain

size (d), subgrain size (δ), recrystallization fraction (f_{rec}), dislocation density(ρ), etc. It is notable that besides the central deformation variables, the final microstructure will change as a function of Material-Dependent-Parameters (MDP) and other unknown uncertainties due to for example tool wear, machining parameters uncertainties, etc., which will be considered in the developed models later in the presented work.

On the other hand, (ii) realizing microstructure designs can be reduced to simply one of tuning process parameters to fall within the map's desired subspaces, i.e. microstructure control through $(\epsilon, \dot{\epsilon}, T, MDP) = F^{-1}(X)$. To satisfy the aforementioned prerequisites and assure the necessity to perform further investigation in the context of the above research questions, the ensuing **Specific Tasks** are envisaged as:

T1: Directly measuring the thermomechanics of severe shear deformation, strain, strain-rate and temperature fields using high-speed Digital Image Correlation(DIC) and Infrared (IR) thermography.

T2: Measuring the mechanical properties using indentation as a function of the thermomechanics of deformation.

T3: Measuring the microstructural consequences of severe shear deformation including the grain and subgrain size, dislocation densities, misorientation and the details of the grain boundary.

T4: Statistical modeling of the microstructure responses as a function of thermomechanical conditions.

T5: Mapping the quantitative characteristics of the microstructural consequences to the thermomechanics of SPD in machining (using the measured data).

T6: Maximizing the metastability of nanostructured metals from Severe Plastic Deformation (SPD) in machining

T7: Uncertainty treatment in established models from Severe Plastic Deformation (SPD) in machining

The research effort outlined here is pursued according to these specific tasks and will be described in details in the following chapters. Task T1 is explained in Chapter 3 and tasks T2 and T3 are described in Chapter 4. Tasks T4 and T5 are accomplished for microstructure

responses of gain size, sub grain size, recrystallization fraction, and dislocation density which have led to three journal publications to date [120, 3, 2] and are explained in Chapter 5. Using the established mappings, task T6 will try to maximize the metastability of nanostructured microstructure, which is developed in Chapter 6. Finally, in Chapter 7, task T7 is described, where we try to address the existing uncertainties in the machining process using Bayesian statistics in the subgrain size model.

3.0 EXPERIMENTAL METHODS

To understand the microstructural consequences, it is necessary to choose a deformation configuration that allows for the measurable imposition of these deformation conditions, while simultaneously producing deformed samples that can be characterized using electron microscopy. Large Strain Machining (LSM) as shown in Figure 2, in the plane-strain state, is utilized which enables examination of strains ranging from $1 - 10$, strain-rates in the range of $10 - 10^3$ $/s$, and temperatures from near ambient to 470 K, in a simple shear configuration. This simple shear configuration, as shown in Figure 2, allows us to have a controlled framework for imposition of the favourable level of deformation (first requirement, **R1**).

Also, such configuration directly offers *in situ* measurements of thermomechanical conditions, where the uniform fields of various levels of strain, strain-rate and temperature are imposed in a narrow region (deformation zone). This uniformity is confirmed using a high speed camera and an infrared camera to measure and characterize the thermomechanics of the deformation so that the subsequent observations of the microstructural consequences can be reliably mapped to the SPD conditions. This is schematically illustrated in Figure 3. Also, since the deformation zone is not enclosed in a die (unlike other deformation configurations such as ECAP which is inside a deformation die), it allows for direct characterization of the mechanics of deformation using high speed visible light imaging and infrared thermography, to then allow an accurate elucidation of the microstructural transformations as a function of the thermomechanics of plasticity [120, 3, 2].

To understand the operative plasticity mechanism, we need to have a test of material microstructure. It is notable that the mechanics of deformation during chip formation under steady-state conditions in such a system entail uniform SPD for the chip and the surface

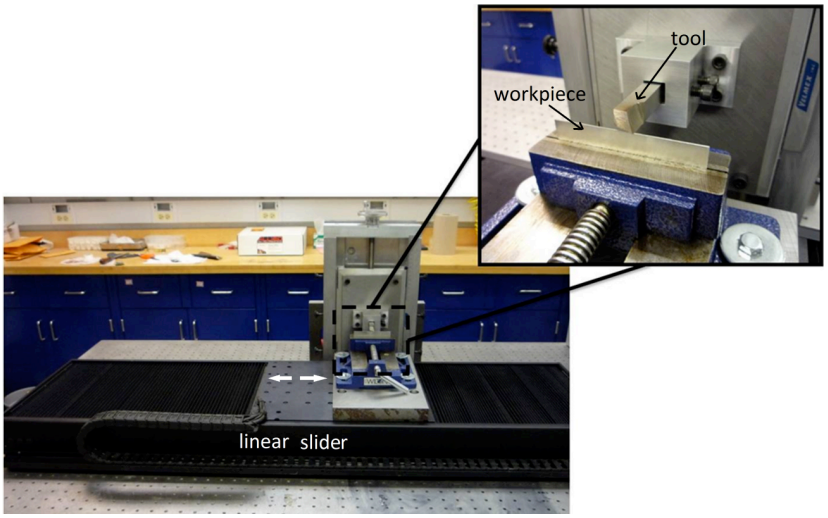

Figure 2: Schematic of Large Strain Machining (LSM).

in the direction of the cut. While the freshly created surface on the workpiece would be subjected to very large strains, the level of deformation would decline further into the bulk to ultimately converge with the characteristics of the undeformed microcrystalline material [120]. The deformation strains on the machined surface appear to converge very closely with that of the strains in the primary deformation zone through direct measurements on a similar prototypical deformation configuration [29]. This is probably not surprising in light of the geometric contiguity of the zone that is the progenitor of both the chip and the machined surface. It has been seen through *in situ* thermomechanical measurements that the deformation zone of machining extends into the surface. Due to this spatial continuity of the deformation zone that forms the chip and the fresh surface, the resulting microstructure in the fresh surface is very similar to that in the chip. Figure 4 illustrates a similarity between the chip and the machined surface in Copper. The Inverse Pole Figure (IPF), obtained by Electron Back-Scattered Diffraction(EBSD) analysis on the subsurface show the microstructure taken from the subsurface, very close to the machined surface which is comparable to that of the chip, imaged close to its midpoint, away from its underside, which would have undergone further deformation in the secondary deformation zone [34]. Hence, we have chosen

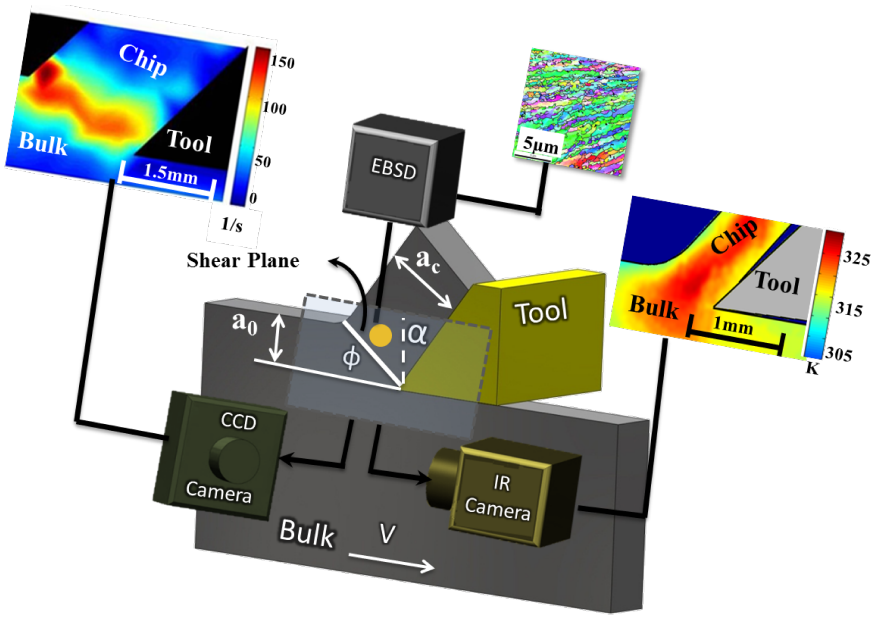

Figure 3: Deformation geometry during chip formation allowing for 2D orthogonal machining; High speed imaging of the deformation zone for DIC along with IR thermography and EBSD analysis of the deformation zone are illustrated.

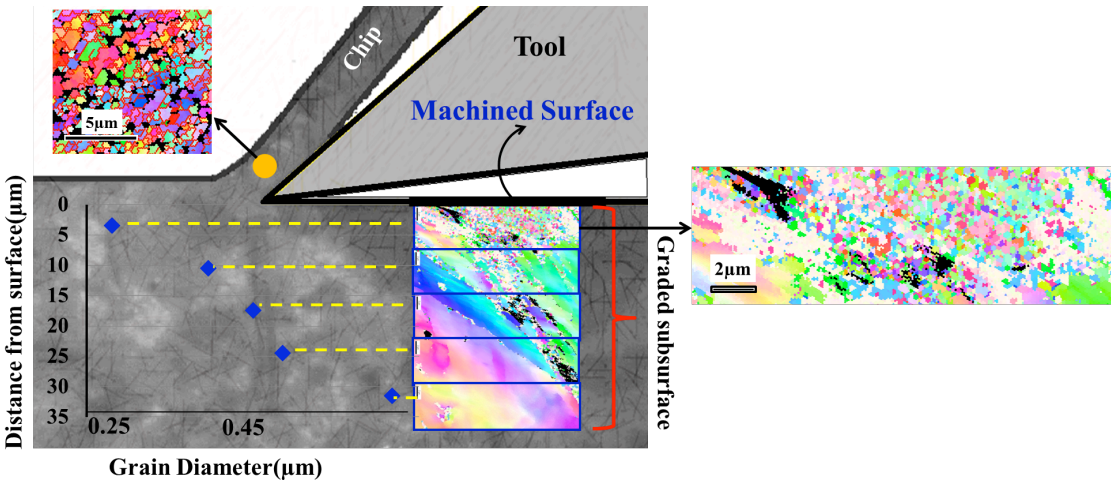

Figure 4: Comparison of OIM micrographs of Cu chip with that near the machined surface, where the subsurface OIM micrograph on the right is approximately $100\mu m$ below the freshly cut surface.

the chip as our microstructure response test to examine the surface microstructure transformations through enabling extensive quantitative microstructure characterizations. Also, the chip offers a much larger area to perform quantitative analysis of microstructures using electron microscopy as a major part of the chip undergoes uniform simple shear deformation.

3.1 MATERIAL SYSTEM

In this study, deformation of Oxygen-Free High-thermal Conductivity(OFHC) Copper is examined over strains ranging $1 - 10$, strain-rates ranging $10 - 10^3$ $/s$, and their coupled temperature rise ranging from ambient to 470 K to identify the mechanisms of microstructure transformation under these conditions. Note that these conditions are chosen to fill the continuum between traditional Hopkinson bar tests (low strain, high strain-rate state) and hot torsion tests (high strain, low strain-rate state). First, microcrystalline OFHC Cu was annealed at $700°C$ for 2 hours and deformed using LSM in a simple shear SPD configuration

as shown in Figure 3, which allows for the peculiar niche of deformation regimes we want to achieve, with the advantages of meeting the few first aforementioned requirements in section 2.1.

LSM imposes severe shear using a wedge-shaped cutting edge characterized by the rake angle (α) that advances against a workpiece and when the undeformed chip thickness, a_0 in Figure 3, is much smaller than the width in the third dimension, the deformation is predominantly one of plane-strains.

Cu in these experiments, in addition to being a useful prototype for Face Centered Cubic (FCC) materials also offers the advantage of undergoing uniform simple shear in this configuration to create "continuous chips" of significant cross-sections that can still be reliably characterized. Also, Cu with FCC crystal structure and absence of any phase transformations excludes the possible complexities that can occur in complicate crystal structure systems. Hence, the focal effort can be proficiently aimed at mechanisms of the microstructure optimization with minimum ambiguity. Further details of this experimental configuration can be found in [3]. Furthermore, based on the realization that the microstructure on machined surfaces is closely related to the chip microstructure, as both are derived from the primary deformation zone, this elucidation is expected to offer an approach to understand the surface microstructure inherited by the freshly generated surface [3]. It should also be noted here that due to such machining configuration, the obtained uniformity applies to both chip and the freshly cut surface, which is engendered from the steady state conditions of LSM.

3.2 STRAIN AND STRAIN-RATE MEASUREMENT

Various deformation conditions listed in Table 1 correspond to different LSM conditions (four rake angles $\alpha = 0°, 20°, 30°$, and $40°$) and various deformation speeds, V (viz. Low (L) = 50 mm/s; Med (M) = 550 mm/s; Med-High (MH): 750 mm/s, and High (H) = 1250 mm/s), which resulted in conditions corresponding to a wide range of strain, strain-rates, and temperatures (Table 1). The samples are denoted as 0L, 0M, 0MH, 0H, etc., where the numbers represent the rake angle and the alphabets L, M, MH, H refer to the

deformation speeds. These conditions resulted in effective strains in the range of $1 - 10$ calculated by:

$$\epsilon = \frac{\gamma}{\sqrt{3}} = \frac{\cos\alpha}{\sqrt{3}\sinh\phi\cos(\phi - \alpha)} \tag{3.1}$$

where ϵ is effective strain, γ is the shear strain, ϕ the shear plane angle, and α the rake angle (Figure 3). The shear plane angle is given by:

$$tan\phi = \frac{\frac{a_0}{a_c}\cos\alpha}{1 - \frac{a_0}{a_c}\sin\alpha} \tag{3.2}$$

in terms of the ratio of the undeformed material (a_0) to that of the deformed chip (a_c) as shown in Figure 3. In all the experiments, a_0 was chosen to be $0.17\ mm$ and the resulting a_c values were measured for the various conditions to estimate the strain value using Equations 3.1 and 3.2 as listed in Table 1.

The strain rate values ($\dot{\epsilon}$) in the deformation zone are known to scale as [5]:

$$\dot{\epsilon} = \frac{CV\cos\alpha\sin\phi}{a_0\cos(\phi - \alpha)} \tag{3.3}$$

Using Digital Image Correlation (DIC) analysis of high-speed images of the deformation zone as illustrated in Figure 3, the constant "C" in Equation 3.3 is determined. This was accomplished using a PCO1200HS camera system and performing DIC on a time series of high speed images for a range of machining conditions with known values of α, ϕ, a_0, and V. After this *in situ* determination, Equation 3.3 was used to back calculate "C" for a range of conditions to determine an average value of 2.77 for Cu (V in mm/s and a_0 in mm). This determination resulted in strain-rate accuracies better than 5% in calibration experiments [64]. The strain-rate values for various sample conditions are listed in Table 1 and a typical DIC image is illustrated in Figure 3.

Table 1: Deformation conditions (effective strain (ϵ), effective strain-rate ($\dot{\epsilon}$), measured temperature using IR camera (T_{exp}), calculated temperature at deformation zone using moving heat source model (T_{calc}) for the various machining parameters (rake angle (α) and cutting speed (V in mm/s)). Hardness values of the deformed chip material resulting from the various thermomechanical conditions are also shown (Vickers Hardness) and the hardness value for bulk Cu is 46 kgf/mm^2. Besides $ln(Z)$ and the parameter R (Equation 5.8) are listed [3].

Samples	V	α	ϵ	$\dot{\epsilon}$ $(1/s)$	T_{exp} (K)	T_{calc} (K)	$ln(Z)$	R	Hardness (kgf/mm^2)
0L	50	0°	8.7 ± 0.8	60	322 ± 4	363	69.3	4.15	154 ± 4.5
0M	550	0°	5.9 ± 0.6	940	-	454	59.1	4.30	147 ± 4.8
0MH	750	0°	5.6 ± 0.7	1240	-	464	58.2	4.31	-
0H	1250	0°	4.9 ± 0.5	2377	-	485	56.6	4.33	109 ± 4.3
20L	50	20°	5.9 ± 0.3	80	342 ± 3	346	72.9	4.08	163 ± 3.2
20M	550	20°	3.9 ± 0.4	1290	378 ± 7	412	64.7	4.16	161 ± 2.5
20MH	750	20°	3.6 ± 0.5	1740	-	416	64.4	4.16	-
20H	1250	20°	3.4 ± 0.8	3130	-	439	62.1	4.19	159 ± 3.1
30L	50	30°	4.0 ± 0.2	100	319 ± 2	332	75.9	4.01	-
30M	550	30°	2.6 ± 0.2	1740	-	379	70.0	4.04	154 ± 5.9
30MH	750	30°	2.5 ± 0.3	2290	-	385	69.3	4.05	-
30H	1250	30°	2.3 ± 0.7	4030	-	402	67.2	4.07	152 ± 4.7
40L	50	40°	2.6 ± 0.2	140	324 ± 1	321	78.8	3.96	158 ± 3.5
40M	550	40°	2.1 ± 0.4	1930	336 ± 2	367	72.2	4.00	157 ± 5.7
40MH	750	40°	2.0 ± 0.6	2520	339 ± 5	372	71.6	4.00	-
40H	1250	40°	1.8 ± 0.7	4680	-	381	70.6	4.00	155 ± 5.3

3.3 MECHANICAL TESTING

Vickers microhardness tests were also performed on the metallographically polished samples. Using a Shimadzu microhardness tester (HMV-2), hardness tests were conducted on different sample conditions. Samples were put in an epoxy mount and polished all the way down to 0.05 microns using alumina suspension. Then a force of 490.3 mN was utilized in these indentation experiments and the average value was taken as the hardness for a minimum of 10 replicates. The standard deviation was obtained less than 6% for all sample conditions. The values are listed in Table 1.

3.4 INFRARED (IR) THERMOGRAPHY

The characterizations of the mechanics of deformation can be complemented with the measurement of the temperature field in the deformation zone. To accomplish this, we used Infrared (IR) thermography which is a powerful tool to provide the temperature field close to a dynamic zone, where we cannot utilize thermocouples or other direct measurement techniques for this purpose. Analogous to DIC method, we performed calibrated thermography of the deformation zone for several conditions from the side of the deformation zone as illustrated in Figure 3 using an Infrared (IR) camera (FLIR 325A). To achieve a calibrated system, a calibration sample was first coated with black stove paint in order to standardize the emissivity. Then, the side of the sample was focused on the deformation zone by the camera. Calibration experiments were performed on a heated calibration-sample and a K type thermocouple was used to record the temperature values of the plate, while it was heated from 298 K to 473 K with a step size of 5 degrees. At each step, radiation values from the region of interest (ROI) were scanned using the FLIR software, ThermoVisionR ExaminIRTM, along with the temperature values from the thermocouple in order to create a calibration curve. This curve provided a one-to-one relation between the radiation measured by the camera and the temperature, which can be utilized to convert the radiation values, emitted from the workpiece during LSM experiments in various machining configurations,

to equivalent temperature values. Moreover, to ensure the steady state of radiation values, a minimum of 3 experiments along with a sequence of 7 frames (obtained from the middle part of the IR video) were conducted at each step of calibration procedure. Also, the camera was set to the maximum possible frame rate of 60 Hz to allow for maximum number of frames that could be obtained for a given machining speed (this setting was more critical for MH and H conditions). Furthermore, using different materials as the calibration sample, the curve is confirmed to be applied for at least Al, Ti, Cu, brass and Ni.

With the calibration curve in hand, copper workpieces were painted with the same stove paint before performing LSM. IR camera was placed in front of the sample and focused on the middle of the deformation zone, where DIC confirmed the imposition of uniform shear deformation, ahead of the tool tip while machining (Figure 3). Then, the radiation counts were recorded and the temperature near the deformation zone was obtained using MATLAB relating the radiation counts to the obtained calibrated curve. The measured temperatures, T_{exp}, for a various sample conditions of Cu are listed in Table 1.

It is notable that the current thermography is capable of the experiment for relatively low strain-rate conditions due to limited frame rate of the IR camera. Also, we should point out the low spatial resolution here, where each pixel on the camera thermograph corresponds to 20 $\mu m \times 20$ μm on the work-piece (note that the deformation zone itself is tens of micrometers in width).

3.5 ORIENTATION IMAGING MICROSCOPY

Following the characterization of the thermomechanics of deformation zone, we performed a quantitative analysis of the microstructure using electron microscopy. For this, we used Scanning Electron Microscope (SEM) for Electron Back-Scattered Diffraction (EBSD) based OIM in a Phillips XL-30 SEM equipped with the EDAX-Ametek EBSD detector featuring a Hikari Camera and TSL OIM software for data acquisition and analysis. To perform such analysis, we focused on the microstructure near the center of the chip, away from the tool-chip interface, where DIC and IR experiments confirmed uniform deformation conditions

with well-quantified strain, strain-rate and temperature conditions (Figure 3). This was important from the point of comparability of the microstructure consequences to the calculable thermomechanics of severe deformation in the primary deformation zone. Thus, after such verification, required data is offered to construct the mapping framework for deformation conditions for the resulting UFG-structured characteristics.

Complementing the characterization of the thermomechanics, the chips were examined in a Scanning Electron Microscope (Phillips XL30) using Electron Back-Scattered Diffraction (EBSD) analysis. The samples for this study were prepared by excising suitable sections of the LSM chip samples and then subjecting them to a series of metallographic polishing steps, followed by vibratory polishing. The regions close to the center of the chip, away from both the tool-chip interface and the free surface were focused on, where the subsequently delineated results from DIC and IR experiments showed uniform deformation conditions. The resulting EBSD micrographs were analyzed and the average subgrain size (δ_m), defined as domains with misorientation greater than 2°, along with their standard deviation ($SD(\delta_m)$) was measured for the various conditions. Also, the average grain size (d), defined as domains with misorientation greater than 15°, along with their standard deviation ($SD(d)$) were calculated.

In this context, we would like to clarify that the diameter of a particular grain is calculated by determining the area of a grain and then assuming the grain is a circle. The diameter is then equal to 2 times the square root of the area divided by π. The average subgrain size can be calculated in two ways using the OIM data collection, when considering values associated with grains. One way is Number Weighted Average which is the conventional numerical average and is calculated as $\delta_m = \frac{1}{N}\sum_{i=1}^{N}\delta_i$ (N is the total number of grains and δ_i is the diameter for grain i) and the other approach to averaging is to weight the value being averaged by the area of each grain. Depending on the parameter of interest (here the grain size), one averaging scheme may be more appropriate than the other. However, since the grain size is uniform here (as the scans in Figure 4), average grain diameters, calculated from either of the approaches, were close to each other and are listed in Table 2. It is no-

table that several scans for the various conditions resulted in sampling of several hundred subgrains and grains to yield reliable estimates for these samples. Transmission Electron Microscopy (TEM) was also performed on electrolytically thinned samples using a JEOL 200-CX microscope [3].

Additionally, the length of regular High Angle Grain Boundaries (HAGBs) ($> 15°$) defined as grains for which the interfaces between the two grains (Grain Boundary-GB) are misoriented by $> 15°$ and Low Angle Grain Boundaries (LAGBs) ($2° - 15°$), defined as grains for which the interfaces between the two grains are misoriented by $2° - 15°$ were used in determining Grain Boundary (GB) characteristics. In Table 3, the results from this analysis, such as the average misorientation angle for LAGB and HAGB, and the average fraction of HAGB (f_{HAGB}) are listed for various sample conditions.

Table 2: Microstructural consequences of deformation conditions listed in Table 1: Measured average grain size (d), average subgrain size (δ_m), standard deviation for measured grain size($SD(d)$) and subgrain size ($SD(\delta_m)$), calculated subgrain size at the initiation of Stage $IV(\delta_{IV})$, exact solution for saturated value of subgrain size(δ_s^{exact}), approximate solution for saturated value of subgrain size(δ_s^{appr}), subgrain size calculated using Equation 5.9 (δ_r).

Samples	d (μm)	$SD(d)$	δ_m (μm)	$SD(\delta_m)$	δ_{IV} (μm)	δ_s^{exact} (μm)	δ_s^{appr} (μm)	δ_r (μm)
0L	0.28	0.01	0.24	0.01	0.303	0.217	0.214	0.236
0M	0.35	0.02	0.25	0.02	0.316	0.236	0.221	0.327
0MH	-	-	-	-	0.314	0.238	0.222	0.334
0H	0.83	0.08	0.72	0.08	-	-	-	-
20L	0.43	0.07	0.33	0.07	0.295	0.209	0.210	0.311
20M	0.65	0.11	0.40	0.11	0.298	0.217	0.214	0.376
20MH	-	-	-	-	0.297	0.217	0.214	0.383
20H	0.74	0.09	0.46	0.09	0.299	0.221	0.215	0.392
30L	-	-	-	-	0.289	0.202	0.207	0.362
30M	0.75	-	0.4	-	0.286	0.205	0.208	0.406
30MH	-	-	-	-	0.286	0.205	0.208	0.410
30H	0.58	-	0.4	-	0.287	0.207	0.209	0.414
40L	0.53	0.08	0.4	0.02	0.284	0.197	0.204	0.401
40M	-	-	-	-	0.282	0.200	0.206	0.418
40MH	-	-	-	-	0.282	0.200	0.206	0.420
40H	-	-	-	-	0.282	0.200	0.206	0.427

Table 3: Grain boundary characteristics for various LSM samples as listed in Table 1. Average misorientation (for LAGB and HAGB), average HAGB fraction ($f_{HAGB} = 1 - f$), recrystallization fraction (f_{rec}) and the fraction calculated using data-fit via Equation 5.20 (f'_{rec}), are shown for various sample conditions. Critical strains (ϵ_{cr}) for the onset of GDRX as functions of both $ln(Z)$ and the parameter R (Equations 5.18 and 5.19) are also listed [3].

Samples	Average Misorientation $LAGB(< 15°)$	Average Misorientation $HAGB(> 15°)$	f_{HAGB} $(1 - f)$	f_{rec}	f'_{rec}	ϵ_{cr} $f(\ln Z)$	ϵ_{cr} $f(R)$
0L	7.2°	41.3°	0.79 ± 0.00	0.55 ± 0.10	0.55	2.65	3.1
0M	7.4°	41.0°	0.64 ± 0.01	0.36 ± 0.04	0.33	-	2.8
0H	8.0°	50.5°	0.87 ± 0.11	0.88 ± 0.02	-	-	2.7
20L	7.3°	40.7°	0.72 ± 0.03	0.40 ± 0.03	0.31	3.69	2.8
20M	6.9°	39.4°	0.49 ± 0.02	0.13 ± 0.09	0.16	1.33	2.6
20H	6.8°	39.1°	0.42 ± 0.02	0.12 ± 0.07	0.12	0.57	2.6
30M	6.5°	35.8°	0.22 ± 0.00	0.01 ± 0.00	0.10	2.84	2.6
30H	7.1°	37.5°	0.34 ± 0.00	0.02 ± 0.00	0.11	2.06	2.5

4.0 EXPERIMENTAL RESULTS

4.1 STRAIN AND STRAIN-RATE OF SPD IN LSM

The deformation zone effective strain and strain-rates are measured according to Equations 3.1 and 3.3 and the values are listed in Table 1. Note that the strain values increase for decreasing values of α to cover a swathe of values ranging $1 - 10$ (for effective strain). Furthermore, for a fixed rake angle, the strain values decrease with increasing cutting velocities. As we see the strain-rates are proportional to velocity (Equation 3.3) and they increase with increasing the cutting velocity for a fixed rake angle. Also, the values are increasing with increasing rake angle for a given velocity.

4.2 HARDNESS VALUES

Hardness values are measured as explained in section 3.3 and are listed in Table 1, which are all higher than bulk Cu for which the hardness value is 46 kgf/mm^2. Also, it is notable that the hardness values (Hv) for all various samples except 0H and 0M are approximately between $150 - 160$ kgf/mm^2 irrespective of the strain imposed on it. This point stands out the saturation of hardness values as a result of severe deformation in the chip.

The two outliers here, 0M with hardness of 147 kgf/mm^2 and 0H with 109 kgf/mm^2, highlight the presence of other elements influencing material properties. Hence, we expect to see a very different microstructure for these thermomechanical conditions in comparison with other sample conditions.

It should be noted that while hardness value may not offer the most sensitive framework for distinguishing their mechanical properties, this observed"stress saturation" is generally consistent with what is observed in SPD of Cu at large strains > 2, including by ECAP, HPT, etc. [138].

4.3 DEFORMATION ZONE TEMPERATURE

To complement the earlier characterizations of the mechanics of deformation, the temperature field in the deformation zone was measured using IR thermography. Figure 5a and 5b illustrate the typical temperature field in the deformation zone that was measured using calibrated IR thermography for two very different thermomechanical conditions corresponding to 30L ($\epsilon = 4$, $\dot{\epsilon} = 100/s$) and 40M ($\epsilon = 2$, $\dot{\epsilon} = 1930/s$), respectively. Both images show the uniformity of the temperature in the middle of the deformation zone (or shear plane in Figure 3), where the camera is focused. The average temperature in the deformation zone (T_{exp}) was measured for a range of LSM conditions and is listed in Table 1. Note that it would be misleading to draw any conclusions about the temperature in the regions of the image, other than at the middle of the deformation zone, considering that elsewhere the camera may be out of focus.

Note that not all LSM conditions could be taken for temperature measurement here due to limitation stated in section 3.4. However, temperature is one of the central elements of deformation mechanism and it is the complex interaction among strain, strain-rate and temperature that result in final microstructure, which highlights the critical need for elucidation of the temperature for all sample conditions. Hence, the temperature is calculated for various thermomechanical as following.

Imposition of SPD in orthogonal machining results in dissipation of plastic work which predominantly transforms into heat in the deformation zone and results in increased temperature of the work piece and the chip. The heat generation occurs in a characteristic "moving

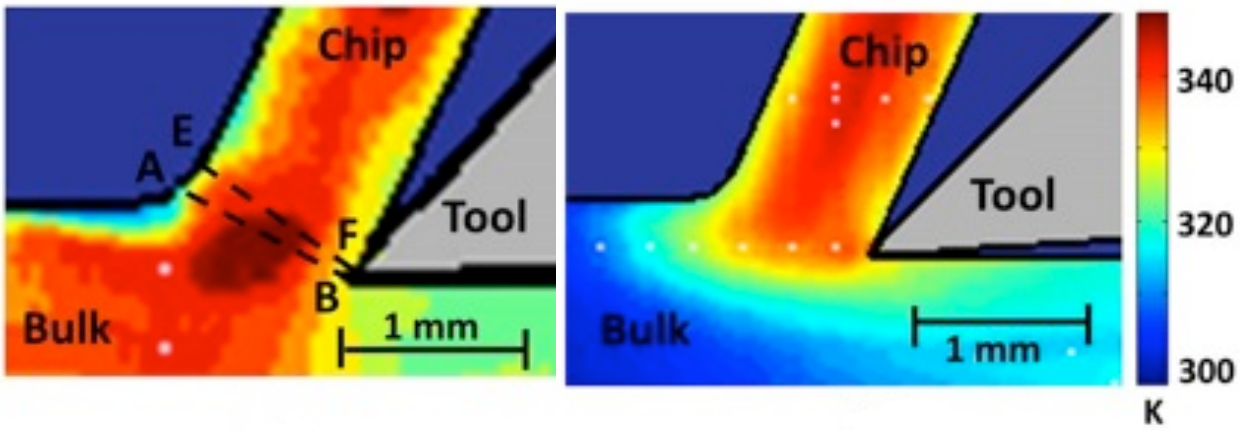

(a) (b)

Figure 5: Infrared thermographs showing the temperature in the deformation zone for a) 30L ($\epsilon = 4$, $\dot{\epsilon} = 100\ /s$) and b) 40M ($\epsilon = 2$, $\dot{\epsilon} = 1930\ /s$). The camera was focused on the center of deformation zone, i.e. the middle of the shear plane as illustrated in Figure 3.

heat source" configuration as a localized shear plane across which mass transport occurs. Using approaches as in Ref. [5], heat source can be conveniently calculated in plane-strain LSM. Both approaches, Oxley's extended model [5] and modified Hahn's model have been applied to LSM and the results are compared with experimental values. However, the results derived based on the approach in [5] were in much better agreement with measurement of IR thermography and thus is used for our further analysis here. Hence, the mathematical foundations of the calculations are explained here for Oxley's extended model. The following analytical route explains the derivation but more details can be found in Ref. [5] (it should be noted that a third temperature model is also derived based on material behaviour deformation which is in process).

To calculate the temperature of the deformation zone, we used Oxley's extended model, given in Ref. [5]. This modified Oxley's approach uses Johnson-Cook (JC) material model to calculate temperature in the deformation zone [64]. The temperature rise in the deformation zone occurs in response to the plastic work as a result of progressive accumulation of the large shear strains to convert the undeformed bulk into the "chip" material by LSM. Hence, for incremental increase in the strain $d\epsilon$, the temperature rise dT is given by:

$$\rho \; C_p \; dT = (1 - \beta) \; \sigma(\epsilon, \dot{\epsilon}, T) d\epsilon \tag{4.1}$$

where β is the partition parameter that determines fraction of heat transported by the bulk workpiece away from the chip and the deformation zone in the moving heat source configuration that typifies LSM in Figure 3. The partition parameter is calculated by:

$$\beta = \frac{1}{4\alpha} erf\sqrt{\alpha} + (1 + \alpha) erfc\sqrt{\alpha} - \frac{e^{-\alpha}}{\sqrt{\pi}} (\frac{1}{2\sqrt{\alpha}} + \sqrt{\alpha}) \tag{4.2}$$

where $\alpha = (V a_0 \tan\phi)/4\kappa$ and κ is the thermal diffusivity of Cu = 116 mm^2/s [101]. In Equation 4.1, ρC_p is the heat capacity of Cu=3.63 MJ/m^3 [101] and σ is the shear-flow stress. Based on the Johnson-Cook model [64] for describing $\sigma(\epsilon, \dot{\epsilon}, T)$, Equation 4.1 can be integrated to obtain the total temperature rise, which is given by:

$$\int_{T_W}^{T_{EF}} \frac{\rho C_p(T)}{(1 - \frac{T - T_r}{T_m - T_r})^m} dT = (1 - \beta) \left(A\epsilon_{EF} + \frac{B}{n+1} \epsilon_{EF}^{n+1} \right) \left(1 + C ln \frac{\dot{\epsilon_s}}{\dot{\epsilon_0}} \right) \tag{4.3}$$

where ρC_p is the heat capacity of the workpiece, T_W the temperature of the workpiece, T_r the room/reference temperature, T_m the melting temperature of the material, and $\dot{\epsilon_0}$ the reference strain-rate, which is taken as 1 $/s$. Values for $\rho C_p(T)$ which varies with temperature, were obtained by the method of least square fit, using cubic splines as given in Ref. [143]:

$$C_P(\frac{T}{100}) = a_0 + a_1 t + a_2 t^2 + a_3 t^3 \tag{4.4}$$

where $T_{min} \leq T \leq T_{max}$, $t = (T - T_{min})/100$ and the coefficients a_0, a_1, a_2, a_3 vary depending on the range of $T/100$. The values for the coefficients and the input data for the fit were obtained from Ref. [143]. In Equation 4.3, ϵ_{EF} is the strain EF which is the total strain in the chip [5] and $\dot{\epsilon_0}$ the strain-rate in the primary shear zone, which is assumed to be constant throughout the deformation zone. Based on this model, as shown in Figure 5 the plane trace EF represents the plane, where full strain (as calculated in Equation 3.1) is expected to have been accumulated (ϵ_{EF}) and plane trace AB, as shown in Figure 5, represents the region of deformation zone where the accumulated strain(ϵ_{AB}) is approximately half that of the final strain value. Therefore, $\epsilon_{AB} =^1_2 \epsilon_{EF}$ and since we are considering the total strain in the chip for the uniform region, temperature at the trace EF (T_{EF}) is compared with the measured temperature(T_{exp}) in the deformation zone. In other words, T_{EF} is the maximum temperature to which the chip was exposed to and this is the temperature rise that results in microstructural changes in the freshly formed chip, hence it is reasonable to compare the above temperature, T_{EF}, with the experimental values obtained using IR thermography. In above equation A, B, C, m and n are parameters for Johnson-Cook model for Cu which were obtained from Ref. [64].

Solving this integral for material constants yields estimates of the temperature rise associated with the LSM process that compares well with the IR measurements. The calculated values are listed in Table 1 for various LSM parameters(taking T_{EF} as T_{calc}). It is clear from the table that the experimentally measured values agree reasonably well with the calculated values, especially given that the temperature varies significantly in a very narrow deformation zone ($\sim$ few 10s of microns). We can say that for narrower deformation zones, measurement error is greater. However, the values are within 6% average error and the close match between the theoretical calculations and the experimental values, highlight the validity of the thermal model used above for calculation of temperature in the deformation zone. Across the spectrum of the strains and strain-rates considered here, deformation temperatures ranging from close to ambient to 400 K were estimated. These T_{calc} (T_{EF}) values that show good corroboration with the IR measurements will be used in the subsequent modeling of the microstructure evolution obtained from SPD in LSM (Table 1).

From Table 1, we see that temperature in the deformation zone increases with increasing strain and strain-rate, as expected. Moreover, the temperature in the deformation zone is found to be more sensitive to strain values than strain-rate. For all the sample conditions that were considered for this study, the deformation zone temperature is below 500 K, the highest being 483 K for 0H. This fact combined with the knowledge that 0H had the lowest hardness value, indicates that this sample condition underwent recrystallization (RX) under high stress and high strain-rate condition [12]. This is confirmed by the EBSD micrograph, misorientation distribution plot and grain size distribution plot in section 4.4.

The sample with the next highest temperature is 0M which has a deformation zone temperature of 452 K and from the hardness value, we know that this is the softest amongst the rest of the sample conditions. However, micrographs and misorientation distribution (section 4.4), do not suggest any kind of recrystallization (RX) taking place in this sample condition. From the small but statistically significant softening of 0M, it can be construed that recrystallization of copper chips starts at some temperature between 452 K and 483 K. Hence, coarse-grained low-hardness machined surface can be obtained by utilizing orthogonal machining conditions which induces deformation zone temperature close to or higher than 483 K. If, however, fine-grained high-strength material is necessitated, then it is imperative that orthogonal machining conditions should not induce temperature values higher than 452 K in the deformation zone.

4.4 MICROSTRUCTURE CHARACTERIZATION

Imposition of large shear strains is known to entail progressive refinement of the microstructure. The microstructures for a widely spread thermomechanical conditions are illustrated in Figure 6a, b, and c qualitatively, which shows a highly refined, sub micrometer-scale structure. The inset in this figure shows the orientation associated with various colors in the figures. The black lines depict the grain boundaries with misorientation greater than 15°. These samples depicted here correspond to three widely spaced thermomechanical conditions to present a snapshot of the variety of the microstructures that emerged from LSM. The 0L

condition ($\epsilon = 8.7$, $\dot{\epsilon} = 60\ /s$) involving the highest levels of strain at the smallest strain-rate (Table 1), is characterized by the finest subgrain size. The 20M sample on the other hand, is characterized by higher strain-rate and smaller levels of strain ($\epsilon = 3.9$, $\dot{\epsilon} = 1290\ /s$). Also, at this higher deformation rate, the coupled temperature rise is also higher. Intuitively, it is reasonable to expect a much coarser microstructure in this condition than in the 0L case and this is indeed found in Figure 6 and in comparing the subgrain size values in Table 2. The third sample illustrated in Figure 6c is the 30H case that was generated at much smaller levels of strain, but high strain-rates ($\epsilon = 2.3$, $\dot{\epsilon} = 4030\ /s$) and temperatures. This corresponds to a predominantly subgrain dominated microstructure that is not as refined as the 20M or the 0L sample. The Inverse Pole Figure (IPF) maps from EBSD illustrate a subgrain structure that is found to closely resemble the TEM images for each of the conditions [3]. The black lines in the EBSD micrographs demarcate high angle grain boundaries that are characterized by misorientations $> 15°$. Additionally, the TEM images illustrated varying dislocation contents across the various conditions [3]. As expected, the highly strained 0L case shows a structure that is remarkably free of dislocations in the interiors of the refined subgrains. The 20M case shows a greater dispersion of dislocation tangles and the 30H case shows significant dislocation content in the interiors of the subgrains. It should be noted that the result from EBSD analysis of 0H condition in [120, 3] proves the low-hardness equi-axed microstructure of 0H, which is conspicuous compared to the elongated grain structures of rest of the samples [120, 3]. Even the grain boundaries of 0H are sharply aligned - very unlike a deformed sample - while other samples have serrated grain boundaries which are a direct outcome of the severe plastic deformation that these samples were subjected in LSM. For the various microstructures, the average grain size, average subgrain size and their standard deviation are measured from the EBSD scans and listed in Table 2. More examination of the IPF images on the sample conditions is explained in chapter 5.

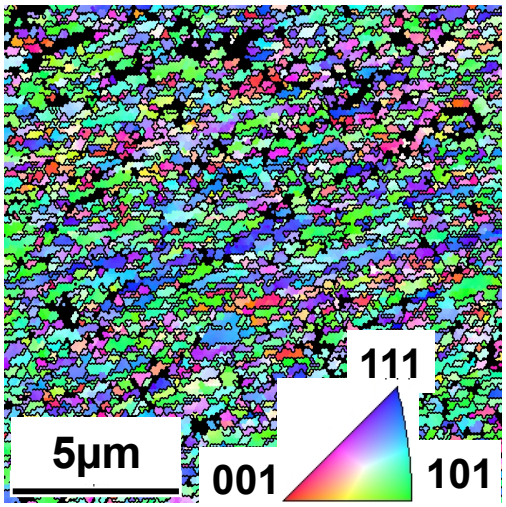

(a) 0L: $\epsilon = 8.7$, $\dot{\epsilon} = 60/s$

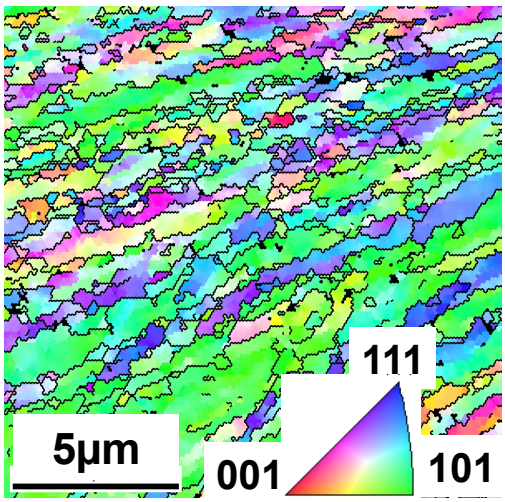

(b) 20M: $\epsilon = 3.9$, $\dot{\epsilon} = 1290/s$

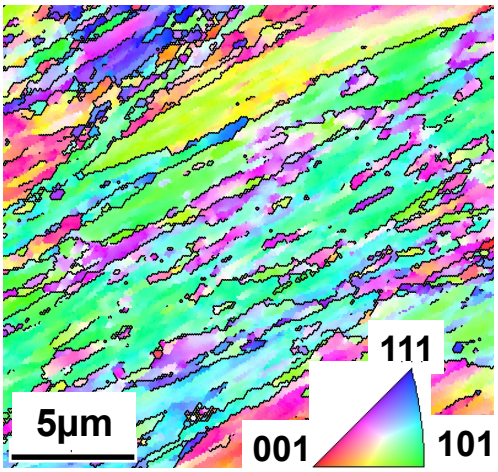

(c) 30H: $\epsilon = 2.3$, $\dot{\epsilon} = 4030/s$

Figure 6: Microstructures for three widely spaced LSM conditions elucidated using EBSD analysis. Inverse Pole Figure (IPF) maps are shown for three widely spaced themomechanical conditions. Black lines indicate the high-angle boundaries.

4.5 GRAIN SIZE AND MISORIENTATION ANGLE DISTRIBUTIONS

TSL software which analyzes the data obtained from OIM enabled us to obtain misorientation distribution and grain size distribution for various sample conditions. The misorientation plots are illustrated in Figure 7a-h and the grain size distributions are plotted in Figure 8a-h. The quantitative aspects of the microstructure viz. average grain size, average High Angle Grain Boundary (HAGB) misorientation, average Low Angle Grain Boundary (LAGB) misorientation, fraction of LAGB and fraction of large grains are summarized in Table 3. In line with conventional characterization, LAGB is defined as grain boundaries with misorientation angles between 2° and 15° while HAGB is defined as grain boundaries with misorientation angles greater than 15°.

Misorientation plots illustrate the wide variety of distributions that can be accomplished by varying the deformation conditions. 0L sample shows a strongly HAGB dominated distribution, while 0H shows a strongly twin-dominated distribution. 0M and 20L show a mixed distribution with almost even proportions of low angle boundaries and high angle boundaries. 20M, 20H, 30M and 30H, on the other hand, show a very strong low angle boundary dominated distribution. 30M and 30H in particular, have negligible high angle boundaries as illustrated in the Figure 7g and 7h.

The various samples studied also displayed a myriad of grain size distribution possible by merely manipulating strain and strain-rate values (Figure 8a-h). From the plots, we see that 0L and 20L have the smallest average grain sizes while 30M and 30H have the largest average grain sizes. All the samples, other than 0H have a significant fraction of small grains, while 0H is composed mainly of large grains, which is also evident from EBSD image in [120]. Moreover, we see from the figure that some of the distributions are unimodal, while others are multimodal. The dash-dot lines were drawn to schematically represent the trend of the distribution. The unimodal distribution for sample conditions 0L, 0H and 20L is obvious, while 0M is mildly multimodal. 20M, 20H, 30M and 30H, on the other hand, are strongly multimodal. Detailed information about larger modes could not be obtained due to the small size of our scans which was limited due to the persistent problem of drift in SEM.

In Table 3, we see that average LAGB for all the sample conditions is $\sim 7^{\circ}$, while the average HAGB misorientation is $\sim 40^{\circ}$, with the exception of 0H. The average LAGB misorientation for 0H is $\sim 8^{\circ}$ and average HAGB misorientation is $\sim 50^{\circ}$. Since the average LAGB and HAGB misorientation values are so uniform across the various sample conditions, they alone, do not provide much insight into the characteristics of the microstructure. In order to extract more information from the misorientation distribution, we calculated the fraction of LAGB, which was defined as the length of LAGB divided by the total length of all grain boundaries. This value varies significantly across different sample conditions and can provide more insight about differences in various microstructures. Since, the respective averages of LAGB and HAGB are approximately same for various samples (with the exception of 0H) and also the shape of their distributions is similar, it also implies that the misorientation distribution of various samples can be completely characterized by single parameter: fraction of LAGBs, f. The values for $1 - f$, representing the fraction of HAGB are listed in Table 3.

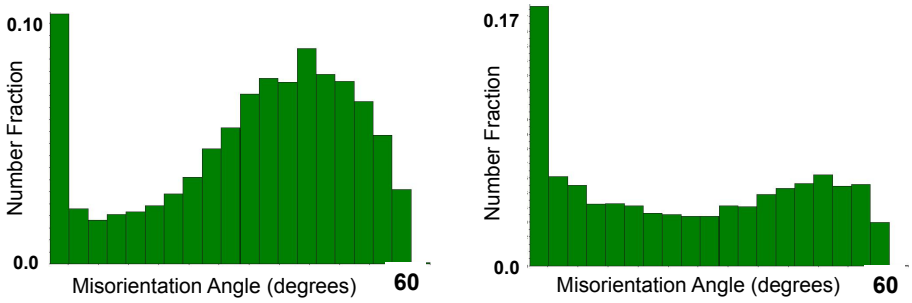

(a) 0L: $\epsilon = 8.7$, $\dot{\epsilon} = 60\ /s$

(b) 0M: $\epsilon = 5.9$, $\dot{\epsilon} = 940\ /s$

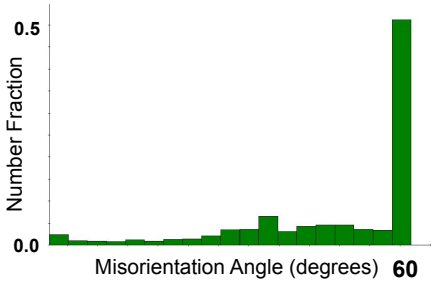

(c) 0H: $\epsilon = 4.9$, $\dot{\epsilon} = 2377\ /s$

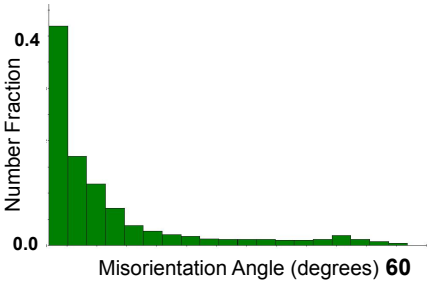

(d) 30M: $\epsilon = 2.6$, $\dot{\epsilon} = 1740\ /s$

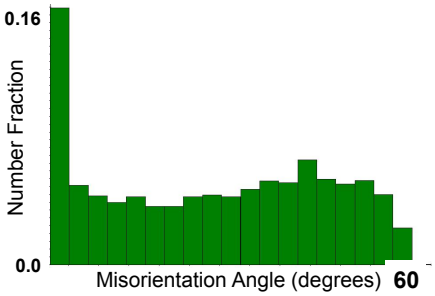

(e) 20L: $\epsilon = 5.9$, $\dot{\epsilon} = 80\ /s$

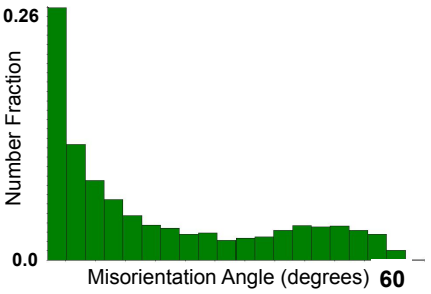

(f) 20M: $\epsilon = 3.9$, $\dot{\epsilon} = 1290\ /s$

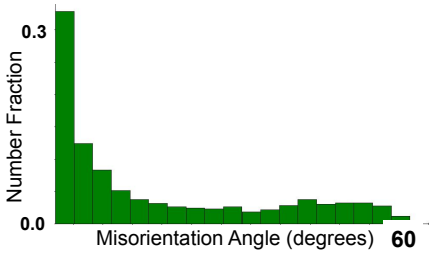

(g) 20H: $\epsilon = 3.4$, $\dot{\epsilon} = 3130\ /s$

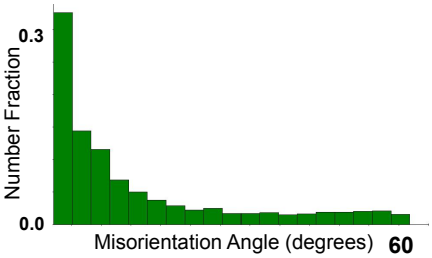

(h) 30H: $\epsilon = 2.3$, $\dot{\epsilon} = 4030\ /s$

Figure 7: Misorientation distribution plots for various sample conditions: 0L is strongly HAGB dominated. 0H is strongly twin-dominated. 0M and 20L have even distributions of LAGB and HAGB. 20M, 20H, 30M and 30H are strongly LAGB dominated. (Note: Total misorientation is 62.8°, hence each block represents $62.8°/19 \sim 3.3°$).

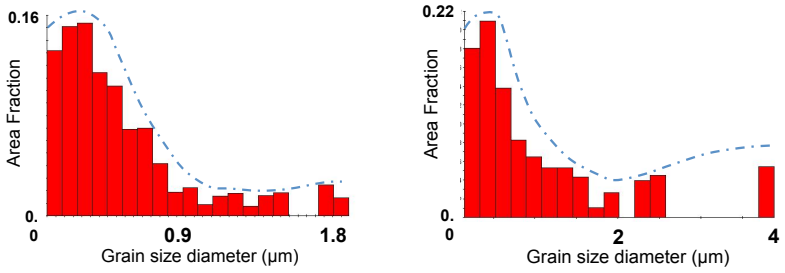

(a) 0L: $\epsilon = 8.7$, $\dot{\epsilon} = 60\ /s$

(b) 0M: $\epsilon = 5.9$, $\dot{\epsilon} = 940\ /s$

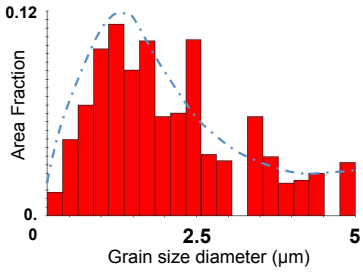

(c) 0H: $\epsilon = 4.9$, $\dot{\epsilon} = 2377\ /s$

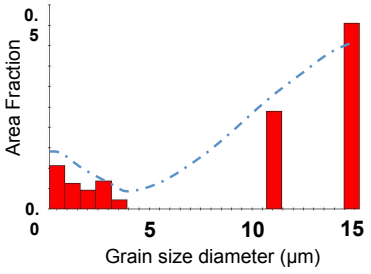

(d) 30M: $\epsilon = 2.6$, $\dot{\epsilon} = 1740\ /s$

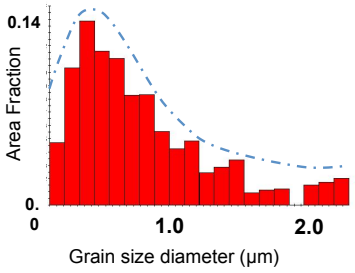

(e) 20L: $\epsilon = 5.9$, $\dot{\epsilon} = 80\ /s$

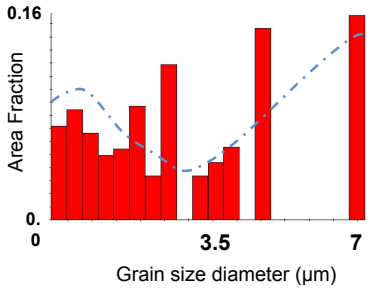

(f) 20M: $\epsilon = 3.9$, $\dot{\epsilon} = 1290\ /s$

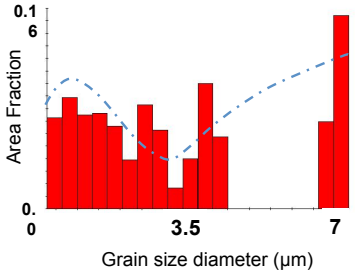

(g) 20H: $\epsilon = 3.4$, $\dot{\epsilon} = 3130\ /s$

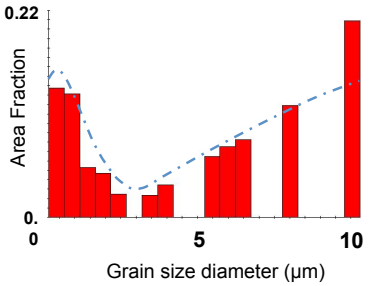

(h) 30H: $\epsilon = 2.3$, $\dot{\epsilon} = 4030\ /s$

Figure 8: Grain size distribution plot for various sample conditions. The dash-dot line show the general trend of the distribution and illustrates the unimodal distribution in 0L, 0H and 20L, small fraction of multimodal grain distribution in 0M and strong multimodality in 20M, 20H, 30M and 30H.

5.0 ESTABLISHED RATE STRAIN MICROSTRUCTURE (RSM) MAPS

Characterization of the thermomechanics of deformation by *in situ* measurements of strain, strain-rate and temperature of shear deformation in our experiments with LSM, was complemented with quantitative analysis of microstructures in the resulting chip. In our preliminary set of experiments we examined a broad spectrum of strain, strain-rate and temperature ranging from $(1-10)$, $(10-10^3\ /s)$ and ambient to $\sim 500\ K$ in Cu. Confirming the uniformity of the shear deformation in the chip material through DIC and IR approaches, this zone was studied for microstructure characterization in electron microscopy. Microstructure evolution across this spectrum of thermomechanics involves interactive effects of temperature with the large strains and strain-rates. However, little is known how these interactions result in the final microstructure and when seeking to understand this range of microstructure, the absence of any "phase-space" is notable. Hence, the development of such space is critical on which the various microstructural characteristics can be projected, one-to-one. In this section, the obtained results towards this delineation are presented.

5.1 GRAIN SIZE AND MISORIENTATION ANGLE MAPPING

Mappings of grain size and misorientation angle is accomplished by developing a new semi-log Rate-Strain-Microstructure (RSM) space, with x-axis as the Zener-Hollomon (Z) parameter [74], an Arrhenius-type rate equation and y-axis as the effective strain [120]. The idea is to populate this phase-space such that the deformation parameters will be the defining vehicle for the resulting deformed microstructure characteristics. In the deformation zone ahead of the tool-tip, the average strain-rates ($\dot{\epsilon}$) and temperatures (T) correspond to Z parameter

values as: $Z = \dot{\epsilon} \exp(Q/RT)$ where R is the gas constant and Q the activation energy taken to be that for self-diffusion in Cu which is $\sim$ 195 $kJmol^{-1}$ [77] (since in nanocrystalline and UFG materials volume density of interfaces is very high and thus even at very high temperatures it can be expected that most of the material transport will occur through Grain Boundary(GB) diffusion, and hence GB diffusion will be the operative mechanism for deformation processes in nanocrystalline and UFG materials).

In contrast to the well-established role of strain on the resulting deformed microstructures, the effect of Z parameter which clubs together the effects from two very different parameters [149], strain-rate and temperature is less direct. Z parameter occurs as a critical variable in models of dislocation storage and recovery [95, 96]. A big portion of the microstructure transformation during SPD in orthogonal machining occurs as a direct result of storage and rearrangement of dislocations [92, 107]. It then follows that utilizing Z may indeed offer a viable vector on a phase-space that intends to map deformation parameters to the resulting microstructures. Growing from this rationale, we will show the 2-D RSM mappings composed of Z parameter and strain, demarcated by the regions of varying microstructure characteristics such as grain sizes and misorientation variations. The use of Z parameter to pin-point microstructural and constitutive response is not new. Z parameter has been used extensively in SPD, especially in relation to Friction Stir Welding. The seminal work on this was done by Jata and Semiatin [60], and others have contributed as well [25, 42]. The Z parameter has also been used in the study of recovery and recrystallization (RX) phenomenon [49, 91] and it is clear from the above studies that lower Z values and higher strain-values promote recrystallization [147, 84]. This conclusion is expected, given that low Z values imply higher temperature, which is favourable for recrystallization (RX).

The entangled effect of temperature and strain-rate on microstructure is obvious from the results on the final microstructure as listed in Table 1 and 2 and in order to make better sense of these two elements, Z parameter is calculated to merge the influence of strain-rate and temperature under one parameter. Furthermore, this parameter gives us the opportunity to present three dimensional information on a 2D plot with the strain and the Z parameter as the two main variables of the phase-space. Note that this effort envisages the use of orthogonal machining as a microstructure response test for extreme

deformation for delineating a Rate-Strain-Microstructure (RSM) framework that uniquely maps one-to-one the nanostructural characteristics to the strain and Z (i.e. strain-rate and temperature combined together into an Arrhenius-type rate equation). Recall that once this is accomplished, it would offer a generic framework for microstructure control and design, not just on the machined surface which results from SPD under high strain-rates, but also in processes such as Friction Stir Welding/processing, Equal Channel Angular Pressing (ECAP) and other high strain/strain-rate metal forming operations. Using the equation mentioned above, the Z values are calculated for a range of strain and strain-rate conditions and the values are listed in Table 1.

In order to make this framework applicable as a predictive tool, statistical regression analysis is utilized here to demarcate sections on the map that denote regions of distinct grain size distribution and misorientation distributions. In this investigation, 0H sample was intentionally left out of the regression analysis, as drastic transformations occur at 0H conditions. In our recent study [2], the thermomechanical conditions of this sample are shown to result in a fully recrystallized microstructure and consequently for strain, strain-rate condition or strain-Ln(Z) conditions, which result in temperature higher than that for 0H, we can expect to have a similar coarse grained recrystallized microstructure. Hence, we focus our study here on the deformation conditions below this temperature, where we see interesting combination of grain size and misorientation distribution for different range of strain and strain-rate conditions.

Statistical regression analysis as a model building method is performed considering grain size as d and LAGB fraction as f as the responses (obtained from quantitative electron microscopy) and rake angle as α and orthogonal machining speed as V as predictors (critical deformation parameters). The statistical analysis software Minitab was used to obtain a simple linear regression analysis to generate grain sizes and LAGB fractions in terms of the above mentioned predictors:

$$d = 0.292 + 0.00445\alpha + 0.000323V \tag{5.1}$$

$$f = 0.19764 + 0.00751\alpha + 0.00021956V \tag{5.2}$$

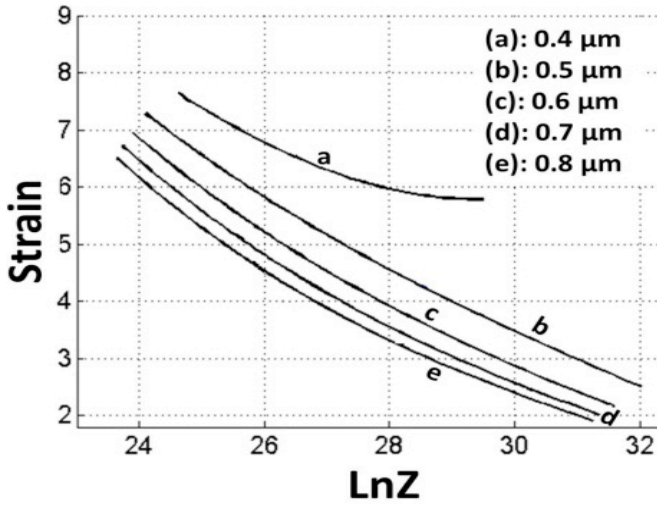

Figure 9: Equi-average grain size contours on RSM space for Cu.

where α is in degrees and V is in mm/s and grain-size, d, is in micrometers. Equation 5.1 can be used to obtain the required velocity for a determined (desirable) grain size for various rake angles. Since we are able to characterize the strain-rate field (based on DIC data), the strain measurements using Equation 3.1 and the temperature filed (based on calculations summarized earlier), it is then possible to delineate the grain size and LAGB fractions in terms of $\ln(Z)$ and strain. The latter is accomplished by utilizing our data on strain and strain-rate as a function of the cutting speed that we had gathered for the various conditions, and building a second layer of regression analysis that related the deformation parameters to the strain and the strain-rate values. These statistical analyses enabled us to create suitable contours for equi-grain size and the equi-fractions of LAGBs on the Rate-Strain-Microstructure maps (Figure 9 and Figure 10 respectively).

Figure 9 demarcates the different processing conditions that can be used to obtain very fine grains or coarse grains. Fine grains can be expected to provide higher strength but lower ductility, while coarse grained microstructure can be expected to provide lower strength with higher ductility. Moreover, this map can help locate regions, where significant multimodal grain size distribution can be obtained. Multimodal grain size distribution has been shown to provide high ductility along with high strength [142, 152, 136]. Furthermore, we observe that

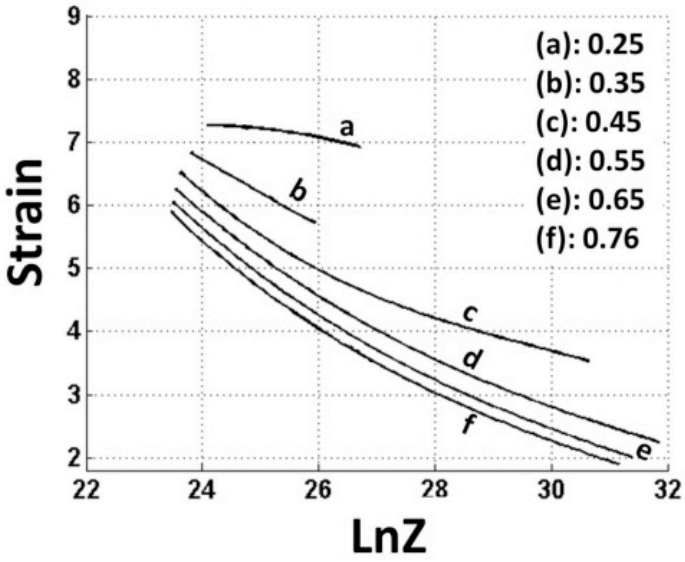

Figure 10: Equi-low angle grain boundary fractions on RSM space for Cu.

the degree of multimodality, defined as fraction of grains in larger modes, varies significantly across the sample conditions. This can be a very powerful tool in design of materials, since it is known that fraction of large grains plays a very important role in determining the mechanical properties of the materials, especially its ductility [146, 52, 116]. Such intricate information can be instrumental in designing a material, especially given that only surface microstructure needs to be altered to influence the overall mechanical characteristics of the material.

Figure 10 illustrates the variation of LAGB-fraction across the RSM map. As noted earlier, since the average LAGB and HAGB misorientations were very similar for all the sample conditions (other than 0H), we utilized LAGB-fraction as a parameter to describe misorientation distribution for the various sample conditions. Relative fraction of HAGBs has been shown to be related to the strength of the material [153]. Our recent results indicate that fraction of LAGB is related to the thermal stability of nanostructured materials (unpublished results) and further systematic studies are underway to provide concrete and conclusive evidence for the same. There are, however, other phenomena that are well known to be directly related to grain boundary characteristics, like diffusion, energy and mobility [55,

20, 124, 125, 56, 48]. It is known that diffusivity is much faster through HAGBs and much lower through LAGBs, while mobility of HAGBs is much higher than LAGBs and this difference in properties can be exploited to design components with specific application in mind. For instance, if high diffusivity is required in a material, processing conditions can be set, which provide HAGB dominated microstructure, which in turn will aid high diffusivity. This can be particularly useful in manufacturing components like gears, where carbon needs to be diffused on the surface for high strength. Thus, high diffusivity would allow better penetration of carbon and hence higher strength up to greater depths of the gear tooth, which can substantially increase its life and durability.

The results from this work is summarized in Figure 11, which shows a "process parameter map" using the RSM framework that can be used for relating various microstructural characteristics to the processing parameters and thereby providing the ability to predict material properties. Strains below the value of 2 do not result in SPD, consequently do not produce significant changes in microstructure and hence, were ignored in this map. Strain and strain-rate conditions that result in temperature as high as or higher than that for 0H can be expected to result in recrystallization. High strain and high $\ln(Z)$ condition can be seen to be resulting in finer grain structures while lower $\ln(Z)$ and strain values result in coarse grain structures. This is along the expected lines since high $\ln(Z)$ implies lower temperature and hence, not enough thermal agitation for the grains to grow, while lower $\ln(Z)$, on the other hand, implies higher temperature and higher tendency for the microstructure to coarsen. The contour, which was obtained from equi-grain size of 0.4 μm is utilized as a transition between very fine grains from not so refined grains. And the contour, which was obtained for 0.7 μm grains demarcates region, which produces relatively coarse grains. The region in between the two contours will have gradual change in the grain size from 0.4 μm to 0.7 μm.

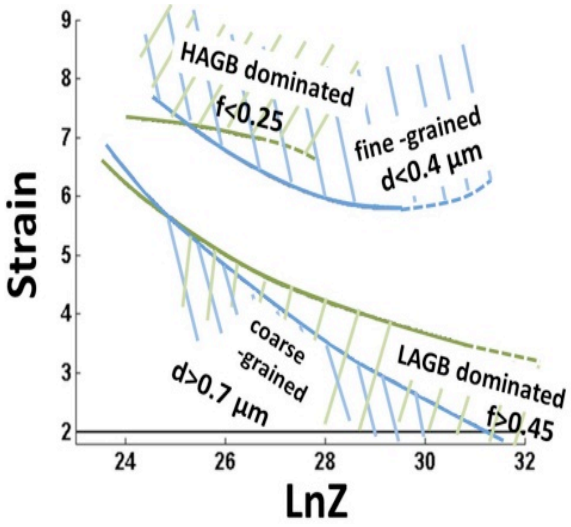

Figure 11: RSM map of d: grain size and f: fraction of low-angle grain boundaries($f = 1 - f_{HAGB}$) delineating qualitative aspects of microstructures for Cu (HAGB: High Angle Grain Boundary).

On similar lines, high $\ln(Z)$ and high strain conditions are expected to generate LAGB dominated microstructure, however its variation with respect to $\ln(Z)$ is different from that of fine grained structure and this can lead to interesting medley of microstructures. The equi-LAGB plot with value of 0.25 and 0.45 are drawn to define LAGB dominated and HAGB dominated regions. The region above $f = 0.25$ can be interpreted as region dominated by HAGBs, while region below $f = 0.45$ can be seen as being dominated by LAGBs and in between, we have mixed microstructure. The suitability of these plots to predict material properties is at once obvious when we realize that all the samples with multimodal grain size distribution lie in one corner of this plot, namely the region of intersection of high LAGBs coarse-grain microstructures.

It is imperative to keep in mind that the current maps were obtained using just 8 data points. However, note that the RSM maps, at this stage of its development are essentially empirically-derived response maps. It is reasonable to anticipate that like any other regression-type mapping, it will capture the behaviour fairly accurately in the vicinity of the

data-points. As more extensive data-sets become available, these mappings will become increasingly more accurate. The accuracy of the maps can be dramatically enhanced especially, when more fundamental crystal-plasticity-based models become available to accurately predict the nanostructural characteristics from SPD in machining. Taken as a whole, this map potentially offers both a process design guide to understand as well as a tool to predict the myriad of microstructures that can be obtained from SPD across a wide range of conditions.

5.2 SUBGRAIN SIZE MAPPING

In this section we will focus on the subgrain size resulting across the broad spectrum of conditions examined here. The underlying premise is that this would offer a step towards microstructure control in SPD configurations that involve the superposition of large strain-rates, such as those encountered by machined surfaces that characterize most prevalent engineering components.

In LSM, the accumulation of strain occurs progressively in a single deformation pass in a deformation zone characterized by strain-rates and temperatures listed in Table 1. Here, SPD is imposed in simple-shear to various final values, starting from the undeformed state ahead of the cutting tool's edge as illustrated by the DIC micrograph in Figure 3. As the material is being progressively subjected to the various final strains listed in Table 1 ($\sim 1 - 10$), it transitions through the different work-hardening stages in the narrow deformation zone, for each sample. For final strains > 2 considered here, all samples can be reasonably assumed to have transitioned through to the Stage IV of work hardening, albeit with microstructural characteristics unique to the individual thermomechanical conditions [68, 94]. Note that much of the current understanding of SPD microstructures is based on low strain-rate studies, which may be confounded by the superposition of the higher strain-rates considered in this study. And, to the best of our knowledge, we are not aware of a framework for encapsulating the microstructural characteristics resulting from the broader array of strains, strain-rate and temperature combinations. But, in several low strain-rate studies that are reviewed in [68], by extracting work hardening coefficients (Θ) in deformation experiments that measured the

flow stress (τ) for strains up to ~ 9, onset of Stage IV was detected as a characteristic "kink" in the $\Theta - \tau$ curves, typically in the vicinity of ~ 2 for Cu. While, it is not analogously possible to resolve the transitions through the various stages of work hardening in the narrow deformation zone of LSM, such earlier observations further our expectation that the subgrain-dominated microstructures observed here, are a consequence of progressive deformation to Stage IV.

As a starting point in this work, we focus on relating the subgrain size to the deformation thermomechanics, towards which, we begin by examining them within the context of established models of Stage IV subgrain microstructures developed from low strain-rate SPD studies akin to that in Ref. [94]. These models predict a progressive refinement of subgrain structures with strain that is dynamically limited by recovery processes, and often culminates in the achievement of a saturation of the microstructure refinement to limit the smallest achievable subgrain sizes from SPD. It is reasonable to expect a similar interplay of recovery and refinement mechanisms here. We make an assumption here that the subgrain sizes in our regime of large strains, strain-rates and temperatures can be captured as a "semi-empirical analytic continuity" of the traditional models that explain the behaviour at the smaller strain-rates. To accomplish this, we will first examine how our experimental observations across the broad strain/strain-rate/temperature regimes correlate with predictions of the conventional models of Stage IV microstructures. From this, we will extract suitable parameters as functions of strain, strain-rate and temperature to encapsulate the observed subgrain sizes across the spectrum of conditions studied here. Naturally, this leads to the accomplishment of the other critical aim of this study, to map the thermomechanics of deformation to the resulting subgrain size, thus offering a microstructure prediction and design tool relevant to shear deformation processing across a broad range of strain, strain-rates and temperatures. While semi-empirical in nature, such analysis can offer insights on microstructures from SPD configurations such as LSM, where materials are subjected to large strains, progressively in a single deformation pass and in a narrow deformation zone.

The current understanding is that microstructure refinement is not merely a monotonic function of strain, but is often dynamically limited by two competing mechanisms. In the athermal limit (corresponding to the 0 K limiting case) and at large strains > 2 that is nominally in Stage IV , the refinement of subgrain size (δ) is known to follow [94]:

$$\frac{d\delta^-}{d\epsilon} = -\frac{\sqrt{3}b^{1/2}}{\phi^{3/2}\delta_{IV}^2 K_{IV}}\delta^{5/2} \tag{5.3}$$

where b is the Burgers vector (0.256 nm for Cu) [94], ϕ_{IV} is Stage IV average sub-grain boundary misorientation for which, the reasonable value $\phi_{IV} = 3°$ is used and the constant K_{IV} for copper was calculated to be 30.87 [94]. δ_{IV} is the subgrain size at the initiation of Stage IV, albeit calculated using models validated with low-strain SPD [94], that we are using as a starting point in our analysis. The calculated values are listed in Table 2. Equation 5.3 has its origins in detailed considerations of "principle of scaling" or similitude, which posits that microstructure refinement via the development of a substructure, in the absence of dynamic recovery, would essentially scale in a self-similar manner as a function of the deformation strain [94].

However, in reality, this refinement is dynamically counteracted by thermally-induced coarsening, according to [94]:

$$\frac{d\delta^+}{dt} = \dot{\epsilon}\frac{d\delta^+}{d\epsilon} = \nu_D b^2 B_\delta \sqrt{\rho}(\exp -\frac{U_{SD}}{kT})2sinh\frac{PV_a}{kT} \approx \nu_D b^2 B_\delta \sqrt{\rho}(\exp -(\frac{U_{SD} - PV_a}{kT})) \tag{5.4}$$

where ν_D is the Debye frequency, B_δ a pre-exponential constant associated with thermal activation of subgrain growth equal to 2×10^4 [94] and ρ is the density of dislocations. U_{SD} is the activation energy for self-diffusion in Cu $= 3.271 \times 10^{-19} J/atom$ [71], k the Boltzmann's constant and T the deformation temperature. $V_a \cong b^3/\phi$ is the activation volume(ϕ is sub-boundary misorientation) and P is the driving pressure given by $P = 4\gamma_{sb}/\delta$ (the sub-boundary energy) [94]. Note that the hyperbolic term in the Equation 5.4 is often simplified to an exponential function for the deformation conditions and the resulting microstructures observed here. This expression is generally applicable to well-defined subgrain structures observed in Stage IV deformation, such as those observed here in Figure 6, to describe the coarsening response [94].

The microstructure evolution is a superposition of Equations 5.3 and 5.4 as:

$$\frac{d\delta}{d\epsilon} = \frac{d\delta^{+}}{d\epsilon} + \frac{d\delta^{-}}{d\epsilon} \tag{5.5}$$

It has been argued that at very large strains, typically in Stage IV of work hardening, the subgrain size eventually reaches a "saturation value", δ_s, such that the subgrain size (δ) is no longer sensitive to progressive levels of deformation strain (ϵ) i.e. $d\delta/d\epsilon = 0$ at $\delta = \delta_s$. This criterion can be written out as [94]:

$$\sinh \frac{4\xi_\delta G b^4}{\delta_s kT} = \sqrt{3}\frac{\delta_s^3}{\delta_{IV}^2 b K_s}\left(\frac{\dot{\epsilon}}{\nu_D}\right)\exp\left(\frac{U_{SD}}{kT}\right) \tag{5.6}$$

where, ξ_δ is considered to be 50 for Cu, G is the shear modulus equal to 47 GPa [94] and $K_s = \phi_{IV}^2 B_\delta \kappa^{1/2} K_{IV}$. The solution for the implicit Equation 5.6 can be evaluated numerically for the various deformation conditions we had considered. These exact solutions, δ_s^{exact}, are listed in Table 2. Surprisingly, when we plotted the ratio of δ_m/δ_s vs. ϵ, we noticed a correlation in Figure 12 that illustrates a gradual convergence towards the "saturated grain size" with increasing levels of strain, across a range of deformation conditions. Recall, that the strain-invariant, saturated subgrain size is essentially a function of the strain-rate and temperature and is a limiting case. The 0L condition corresponding to the largest strain and the smallest strain-rate (Table 1) appears to converge to the saturated subgrain size. Also, note that this convergence does not appear to be a simple function of the strain, but appears to follow a more complex trend over a swathe of the map-space in Figure 12. This is likely the effect of the interactive effects of the large strains with the strain-rate and temperatures that complicate the trajectories of microstructure refinement.

Nonetheless, from the distribution of the data points in Figure 12, it is evident that the strain and the limiting grain-size for a given strain-rate and temperature, may offer the elements for the parametrizations aimed at capturing the resulting subgrain sizes. From here, we were motivated to hypothesize a map-space that is parameterized in terms of the deformation parameters onto which the various severely deformed microstructures map to, one-to-one. A scheme presented here, uses the y-axis as the effective deformation strain that essentially encapsulates the "athermal" refinement with progressive deformation (i.e.

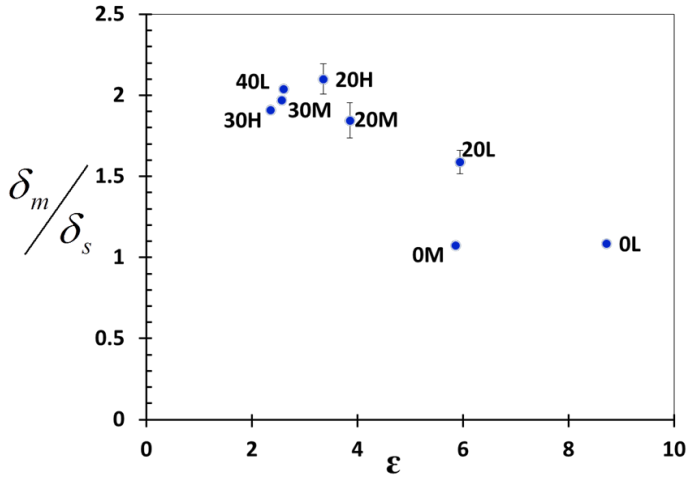

Figure 12: Variation of the ratio average subgrain size to saturated subgrain size (δ_m/δ_s) with deformation strain (ϵ) for various samples.

Equation 5.3). That is, when we move along the y-axis we will be scanning the limiting case, where refinement is not modified by dynamic coarsening. The x-axis, which would be orthogonal to the y-axis, should then encapsulate the "strain-invariant" characteristics of the microstructure. That is, when we move along the x-axis, we should be scanning along the limiting case, where the microstructure is essentially independent of the strain (i.e. y-axis). Orthogonality between x and y axes is strictly accomplished if and only if, along the x-axis, $d\delta/d\epsilon = 0$, which is essentially that corresponding to the saturation grain size (δ_s). All real samples created at finite temperatures and that are not at the grain size saturation, can then be expected to be interspersed on a map-space bound by these two limiting cases as their axes. Unfortunately, the expression for δ_s, is the implicit Equation 5.6, that does not allow a viable parametrization in terms of the strain-rate and the temperature.

But, Equation 5.6 does undergo a very useful simplification, wherein by taking logarithms on both sides and dropping the $\delta \ln \delta$ term, Equation 5.6 can be approximated by Equation 5.7, as below, that still provides comparably accurate approximations of the saturation grain size, δ_s^{appr}. The $\delta \ln \delta$ term is a weak function that remains nearly a constant across the various conditions considered here and adding a constant correction term "η" compensates for it, while allowing for a desirable separation of variables in Equation 5.6. Table 2 illustrates the accuracy of this approximation.

$$\delta_s^{appr} = C_0 \left(\frac{Gb^3}{kT} + \eta \right) \left(\frac{1}{\ln C_1 + \ln Z} \right) \tag{5.7}$$

where $\eta = 190.43$ is the correction factor, $Z = \dot{\epsilon} \exp(\frac{U_{SD}}{kT})$, $C_0 = 4\xi_\delta b$ and $C_1 = \frac{\sqrt{3}}{\delta_{IV}^2 b K_s \nu_D}$ for which the values are obtained as $C_0 = 51.2\ nm$, and $\ln C_1 = 14.77$. Multiplying C_1 and dividing the dropped term by suitable unit measures, the product $C_1 Z$ is rendered unitless and dimensionally consistent. Note that in approximating C_1, the value for δ_{IV} has been considered to be constant $\sim 0.284\ m$, given its insensitivity to the deformation conditions in the regime studied here (see Table 2).

Given the correlation we had already observed in Figure 12, this approximation for the "saturated grain size" reveals a viable parametrization for the x-axis as:

$$R = \left(\frac{Gb^3}{kT} + \eta \right) \left(\frac{1}{\ln C_1 + \ln Z} \right) \tag{5.8}$$

which can be considered a temporally-dependent "rate" function. We note parenthetically that the parametrization for R is roughly analogous to the empirical correlations that have been observed between subgrain size (δ) and $\ln(Z)$ in hot working of Al alloys as: $\delta \propto 1/(a + b \ln(Z))$ [24, 32], where a and b are empirically fitted values. This coincidence in the functional form further motivates us to pursue this parametrization to define the Rate-Strain-Microstructure (RSM) space for projecting the sub-grain sizes, where the x-axis is the R parameter in Equation 5.8 and y-axis is the effective strain.

On this space, Equation 5.9 captures the variation of subgrain sizes across the swathe of thermomechanical conditions on the RSM space:

$$\delta_r = 0.25 - 0.030\epsilon + 0.058R + 0.0003\epsilon R \tag{5.9}$$

Table 2 lists the subgrain sizes calculated using this equation, δ_r, for the various conditions. Note the close correspondence of this equation to the measured values δ_m. Figure 13 illustrates via a contour map, the variation of the subgrain sizes on the parameterized RSM space across a wide-range of strains, strain-rates and temperatures with the experimental measurements overlaid on it for a better perspective.

The choice of the form of Equation 5.9 is of course guided by the fact that it can be considered as a Taylor series expansion function for the subgrain size (δ), i.e. an analytic continuity written as a function of two variables R and ϵ. That is:

$$\delta_r = \delta_0 + \frac{\partial \delta_r}{\partial \epsilon}\epsilon + \frac{\partial \delta_r}{\partial R}R + \frac{\partial^2 \delta_r}{\partial \epsilon \partial R}\epsilon R \tag{5.10}$$

with $\partial^2\delta_r/\partial\epsilon^2$ and $\partial^2\delta_r/\partial R^2$ taken to be zero by ignoring second order effects in ϵ and R.

Comparing Equation 5.9 with Equation 5.10 also indicates the nature of the interactions of ϵ with R in determining the trajectories of refinement. Due to the role of the large strains in refining the grain size, for a constant R, we should expect in Equation 5.10:

$$\frac{d\delta_r}{d\epsilon}|_{R=const} \approx \frac{\partial \delta_r}{\partial \epsilon} + \frac{\partial^2 \delta_r}{\partial \epsilon \partial R}R < 0 \tag{5.11}$$

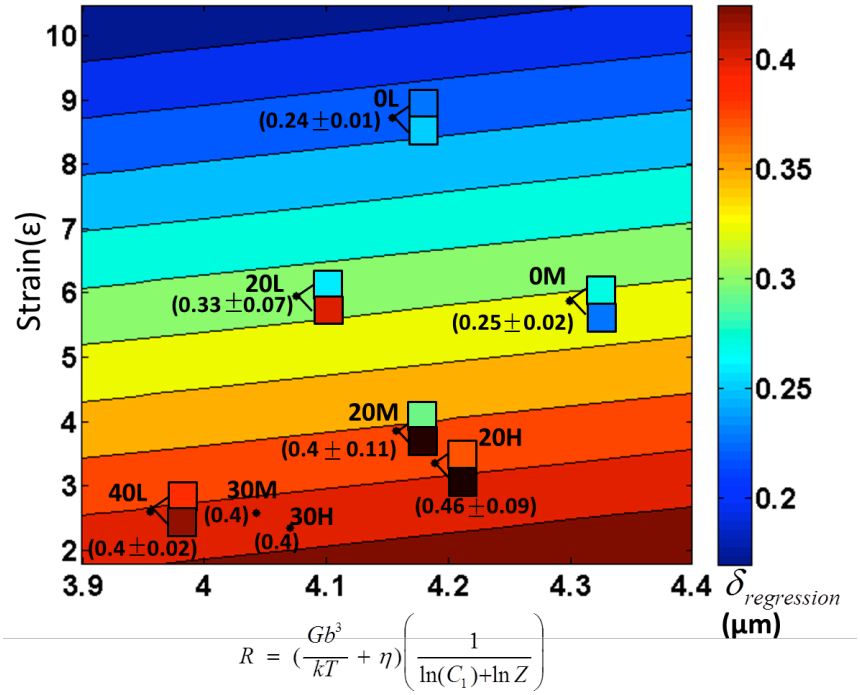

Figure 13: Map of the subgrain size, δ_r, on the RSM space as a function of effective strain (ϵ) and R. Values of average subgrain size and its standard deviation from experimental conditions are marked on the plot. Also, at each experimental point, the mean + standard deviation and mean - standard deviation are shown using the same color-coding scheme as the contour-map to illustrate the fidelity of Equation 5.9 in capturing the mean subgrain size across the various thermomechanical conditions.

Substituting the coefficients in Equation 5.11, we obtain:

$$\frac{d\delta_r}{d\epsilon}|_{R=const} = -0.030 + 0.0003R \tag{5.12}$$

which for our range of R is consistently negative, implying the expected monotonic refinement with increasing strain. In Equation 5.8, we note that with increasing temperature, R usually increases across the conditions considered here and this is found to correlate with an increasing saturation subgrain size, δ_s (Equation 5.7). Therefore, for a constant strain, we should expect:

$$\frac{d\delta_r}{dR}|_{\epsilon=const} \approx \frac{\partial\delta_r}{\partial R} + \frac{\partial^2\delta_r}{\partial\epsilon\partial R}R > 0 \tag{5.13}$$

Substituting from Equation 5.9 reveals that:

$$\frac{d\delta_r}{dR}|_{\epsilon=const} = 0.058 + 0.0003\epsilon \tag{5.14}$$

which is positive for all values of strain. Complementing these effects is the role of interactive effects involving the effect of finite temperature, strain and strain-rate that is manifested in the final, second-order cross-term on the right hand side in Equation 5.9. This term, encapsulates the oft-recognized effect that rate of grain refinement as a function of strain becomes more sluggish (or a less negative derivative with respect to strain) with increasing deformation temperature, i.e. $\frac{d\delta_r}{d\epsilon}|_{T=T_1} > \frac{d\delta_r}{d\epsilon}|_{T=T_2}$ if $T_1 > T_2$. Given that increasing T implies an increasing R over the range of conditions examined here, we can conclude that $\frac{d}{dR}(\frac{d\delta_r}{d\epsilon}) > 0$ or $\approx \frac{\partial^2\delta_r}{\partial\epsilon\partial R}$. Indeed, in Equation 5.10 we find that $\frac{\partial^2\delta_r}{\partial\epsilon\partial R} = 0.003 > 0$.

It is anticipated that analogous parametrizations can be accomplished for other microstructural characteristics, including that for dislocation densities to delineate two orthogonal axes, from a mechanism-based analysis akin to that illustrated here. Here, we still anticipate the "athermal" y-axis to still be the effective strain, although the parametrization for R for dislocation densities would likely differ from that for the subgrain size. Such elucidation that is explained in section 5.4, can help examine the congruence and deviation from

expectations of correlated behaviours between dislocation densities (ρ) and subgrain sizes (δ) of the form $\delta\sqrt{\rho}$ equal to constant that have been reported in [19]. Additionally, modeling of mechanical strength as a superposition of contributions from the grain size, subgrain size and dislocation densities can lead to delineation of property mappings that are essentially functions of the microstructure maps. This can also be performed for stored energies etc. to ultimately utilize such mappings to encapsulate the process-structure-performance triad for a broad spectrum of SPD conditions.

5.3 RECRYSTALLIZATION FRACTION MAPPING

Traditionally, SPD focuses on imposing high strains, typically under conditions involving low strain-rates and moderate temperature rises to create an ultrafine grained (UFG) or a nanostructured material characterized by high strength [83, 118, 67]. However, high strain deformation often involves recrystallization (RX) phenomena that are particularly active in the presence of elevated temperatures [11, 90]. Such recrystallization (RX) can become a central determinant of final microstructure, which directly influences the mechanical properties, resulting formability, while simultaneously affecting other physical properties such as electrical resistivity [47, 27]. Recrystallization (RX) phenomena occurring during deformation are termed Dynamic Recrystallization (DRX) and are characterized by mechanisms that either involve outright grain boundary migration or evolutionary transformations of subgrain boundaries to high angle grain boundaries [107, 91, 109]. Understanding the interplay of DRX with strain-induced microstructure refinement is critical for achieving microstructure control in SPD processes, especially those involving the superposition of large strains, strain-rates, and temperatures [12].

Anecdotally, it has been recognized, over a small swathe of the regime being studied here, typically involving strain of ~ 2 and strain-rate of about 10^3 $/s$ that the coupled thermomechanical state leads to rampant DRX phenomena that directly impact the achievement of refined microstructures [12, 82]. Bridging a knowledge-gap in this thermomechanical processing regime is particularly useful in manufacturing research, given its prevalence in surface

generation by the ubiquitous metal cutting, machining processes as well as in emerging Friction Stir Welding/processing technologies. The functional and mechanical properties of the resulting surfaces that encompass a vast majority of engineering components would then be directly impacted by the microstructural transformations characterizing these conditions; DRX phenomena being preeminent among them. Motivated by this, we resolve the mechanism of DRX in the shear deformation regime of strains > 1 and strain-rates $> 10^2$ $/s$ and their coupled temperature rises [126]. To understand the microstructural consequences, Large Strain Machining (LSM) in the plane-strain state as in Figure 3 is utilized enabling the examination of favourable thermomechanical ranges as in previous sections.

Characteristics such as distribution and fraction of recrystallized/deformed grains and the possible texture transformation are critical in the study of microstructure evolution involving DRX. Several methods can be utilized to determine the fraction of recrystallization. Traditionally, Optical Microscopy (OM) was utilized as the most direct approach to discriminate between recrystallized and deformed microstructure [7, 53] providing the added advantage of directly investigating a large area for an increased sample size. However, OM will not suffice in the case of heavily deformed samples presenting challenges in differentiation between recrystallized and deformed fractions. Micro-harness measurements are used in [7] and expected to decrease during the early stage of recrystallization as a marker for identifying the onset of these phenomena. X-ray diffraction analysis is also a useful method to study the recrystallization process in Copper [45].

Electron Back-Scatter Diffraction (EBSD) in the Scanning Electron Microscope (SEM) has been shown to provide accurate information for discriminating between recrystallized and deformed grains [88, 128, 103, 58]. EBSD analysis facilitates study of both the individual grains and their crystallographic relationship with neighbouring grains [88]. Furthermore, Grain Orientation Spread (GOS) through EBSD analysis [112, 33, 75] can help estimate recrystallization fraction utilizing intra-granular orientation variations. Deformed grains are characterized by high GOS values due to higher Geometric Necessary Dislocation (GND) content in them; recrystallized grains on the other hand have low GOS values as they are relatively free of internal dislocation. The GOS approach was found to be effective for Al [141, 10, 14] and Ni [88, 128, 89, 88] in providing a rigorous framework to quantify

recrystallization characteristics. In the present work, we adapt this technique to characterize the progression of dynamic recrystallization (RX) phenomena across the thermomechanical conditions of interest. This work has been published in [2], where a suitable GOS cut-off threshold is obtained to distinguish recrystallized and non-recrystallized grains. The GOS is then utilized to gauge the extent of microstructure transformation during DRX. Using this analysis, we identify Geometric Dynamic Recrystallization (GDRX), which is a subset of DRX phenomena as the primary vehicle for the microstructure evolution under the range of deformation conditions considered here.

Moreover, in the paper [3], we had shown that the evolution of the subgrain size under such conditions is captured from two parameters: the strain and the parameter "R" that is a function of the strain-rate, temperature and material constants. In this work, we have focused on parametrization of subgrain size to capture its evolution. The idea behind this elucidation is to offer a microstructure variable that can lead to delineation of other microstructural characteristics. For example, the subgrain size is often found to co-vary with the dislocation density in consonance with expectations of similitude or the mechanical strength can be modelled as superposition of contributions from grain size, subgrain size and dislocation density [69, 94, 70]. Furthermore, the onset of GDRX is closely tied-in with the evolution of the subgrain size [107] and here, we will utilize our earlier model for subgrain size to evolve a model for identifying the criterion for the Dynamic Recrystallization (DRX) mechanism as well.

LSM was used to impose a wide spectrum of strains $(1 - 10)$, strain rates $(10 - 10^3\ /s)$ and deformation temperatures ranging from ambient to $\sim 470\ K$ in OFHC (Table 1) to elucidate their effect on the microstructure and in particular, to then quantify the onset and progression of Dynamic Recrystallization (DRX) phenomena. It is known that the formation of recrystallized regions during deformation strongly depends on the coupled temperature rise generated in the primary deformation zone [12, 127, 30, 31]. Therefore, it is important to accurately measure the temperature in the deformation, which was accomplished and listed in Table 1.

5.3.1 Microstructure Evolution as a Function of Thermomechanics of Deformation

Progressive microstructure refinement during Severe Plastic Deformation (SPD) leads to creation of refined interfaces with increasing levels of misorientation which become effective barriers of dislocation slip to strengthen the material. Usually, increasing levels of strain are also found to lead to refined, dislocation-free domains that are encompassed by high-misorientation angle boundaries that characterize the dynamically recrystallized portions of the microstructure. Understanding the overall mechanical behaviour of the materials and the subsequent thermal stability of the ultrafine grained microstructure is strongly related to the extent and fraction of dynamic recrystallization phenomena during SPD. A few subsets of machining-relevant conditions have been studied before, such as the qualitative studies at examining the Dynamic Recrystallization (DRX) phenomena in the moderate-strain ($\gamma \approx 3-4$) at high strain rate ($10^4\ /s$) regime [12]. However, an understanding of the Dynamic Recrystallization (DRX) in the peculiar thermomechanical regime characterizing LSM in particular and machining in general, remains to be examined.

When copper is subjected to large plastic strain ($1-10$), high levels of strain rates ($10-10^3\ /s$), and the coupled temperature (ambient to 470 K) by LSM, a refined microstructure with subgrain sizes of the order of $0.23\ \mu m - 0.43\ \mu m$ is produced [120, 3]. It is reasonable to expect that under these conditions, such refinement occurs in conjunction with Dynamic Recrystallization (DRX), whose progression is a function of the deformation strain, strain-rate, and temperature. The progressive refinement of the microstructure with increasing strain is illustrated in the first row of Figure 14, where highly refined sub micrometer-scale structures are depicted as a function of strain. The top row images in Figure 14, are the Inverse Pole Figures (IPF) maps of the scan area, which are selected from the multiple scans obtained by EBSD analysis to represent the microstructure for the various LSM conditions, Table 1. The middle row in Figure 14, depicts the deformed fraction and the third row in Figure 14, the recrystallization fraction as a function of strain. The acquisition of these filtered images and the delineation of the progression of recrystallization fraction will be discussed in subsequent subsections. Looking at the first row images in

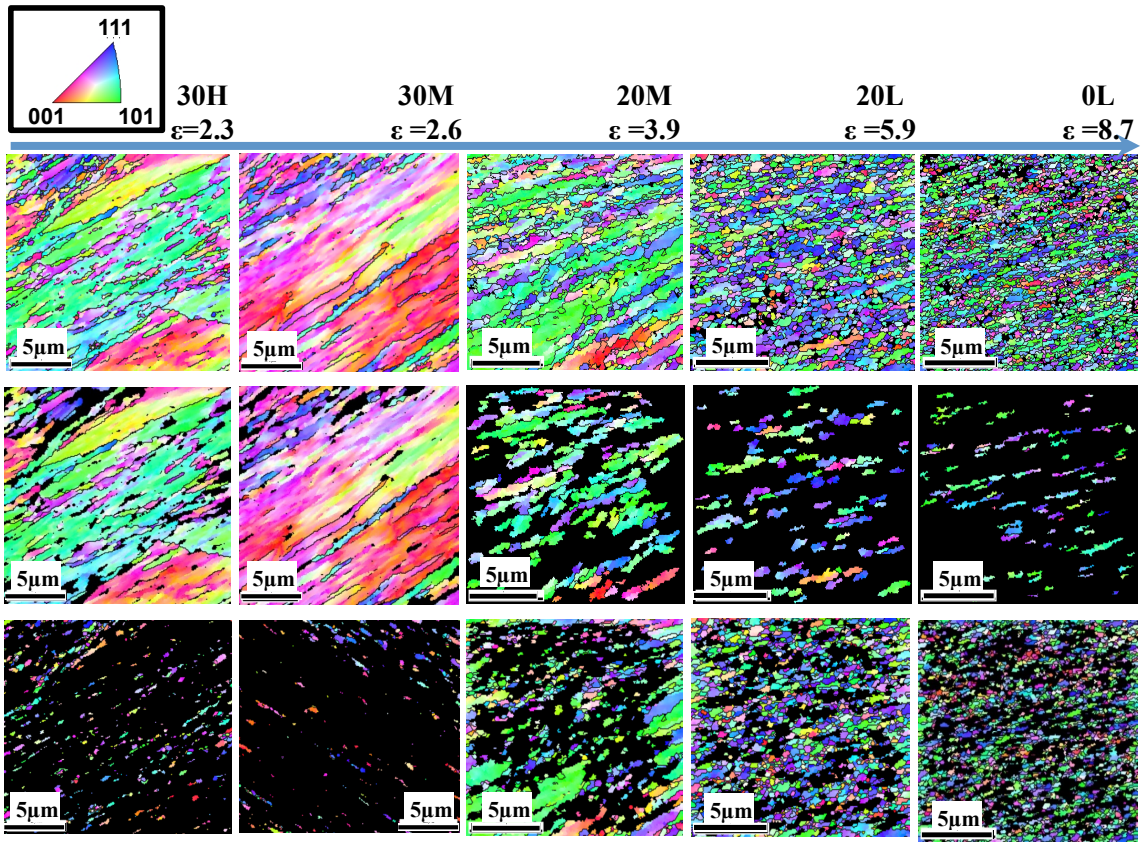

Figure 14: Microstructure evolution with increasing strain. Inverse Pole Figure (IPF) maps of whole scan area (top row), the deformed fraction (middle row) and the recrystallization fraction (bottom row) as a function of strain at the top of the images. The black area represents the corresponding second fraction and the color code orientation on top left associated with the IPF map is inserted as well. Scale bars are 5 μm in length.

Figure 14, left to right, we see with higher levels of strain to the right, microstructure becomes finer, as expected. The 0L condition ($\epsilon = 8.7$), which entails highest levels of strain at the smallest strain-rate and moderate temperature rise (Table 1) is characterized by the finest microstructure. Note that for all these ranges of strain levels, the hardness values as listed in Table 1, appears saturated at $\sim 155\ kgf/mm^2$. This is quite typical of materials that have been subjected to large strains, where hardness measurements become rather insensitive indicators of the refined microstructures resulting from severe deformation.

Realizing that such earlier mean-field approaches did not include Dynamic Recrystallization (DRX) phenomena, we focus our efforts here to quantify this as a function of the deformation conditions. Quantifying the characteristics of deformed microstructures is performed using Electron Back-Scattered Diffraction (EBSD) based Orientation Imaging Microscopy (OIM) data. These include the measurement of the grain size, subgrain size, the distribution and fraction of the recrystallized grains in specimens and a characterization of the crystallographic textures. Also, it can help distinguish the relationship between the neighboring grains and subgrains, which can provide information about the relationships that indicate the onset of microstructural transformations [105, 112].

Data from EBSD analysis can be used in a variety of ways to distinguish quantitatively, the differences between portions of the microstructure that have undergone recrystallization vs. those that are merely severely deformed. For example, severely deformed grains and subgrains that have not been affected by dynamic recrystallization contain a high density of dislocations, including a substantial Geometrically Necessary Dislocation (GND) [43] content. Microstructural domains characterized by these features demonstrate high local crystallographic misorientation/distortion and low Image Quality (IQ) in EBSD. On the other hand, recrystallized regions are characterized by lower dislocation content and concomitantly lower local misorientation and higher value of IQ. Approaches for exploiting such differences between deformed and recrystallized grains include IQ, Grain Average Misorientation (GAM) and Grain Orientation Spread (GOS) methodologies. Although the IQ and GAM approaches seem to suggest useful information in this investigation, they are often too insensitive to distinguish recrystallized grains [88, 103]. The GOS method has been shown to work successfully in previous studies [128, 103, 88, 14], which is our preferred methodology here. Often, utilizing these approaches requires the establishment of the base-line for recrystallization (usually a sample characterized by rampant grain growth) against which, inhomogeneous microstructures comprised of mixtures of deformed and recrystallized regions can be characterized.

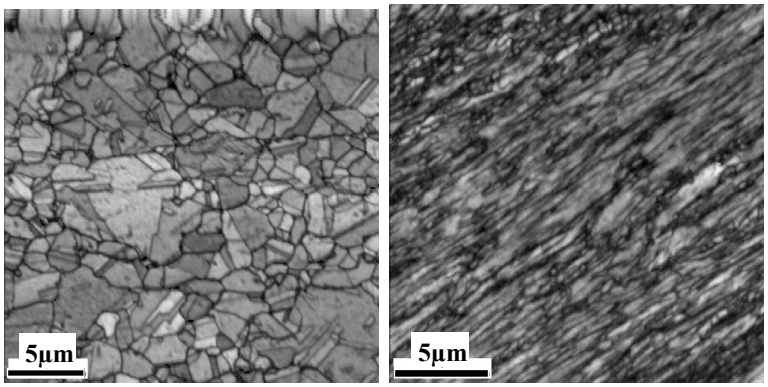

(a) (b)

Figure 15: a) IQ microstructure map of 0H showing coarser, predominantly defect-free grains, b) microstructure of the 30M sample showing a defect-ridden low IQ microstructure.

Here, we identify the 0H sample (Table 1) that underwent SPD at a deformation temperature of 485 K as the base-line. We found that this sample had a low hardness and a very coarse microstructure, likely resulting from rampant Dynamic Recrystallization (DRX) [107]. It is also apparent from the IQ map in Figure 15a) that the 0H sample is characterized by significantly lower defect content and a coarser microstructure than a typical deformed microstructure like that in 30M sample, Figure 15b. It is notable that the deformed microstructure in 30M sample has led to the low quality IQ image in Figure 15b where the haziness of the image is due to large defect densities.

5.3.2 Grain Orientation Spread (GOS)

Grain orientation spread (GOS) has been used to discriminate the deformed and recrystallized grains by providing information on the distribution of misorientations within the grains [128, 89]. GOS is defined as the average misorientation among all the points within the grain with its value based on the orientation (g) for N=number of pixels, for which the matrix g is measured from EBSD as [75]:

$$GOS = \frac{1}{N-1}\frac{1}{N}\sum_{i=1}^{N}\sum_{j=1}^{N}\triangle g_{ij}(g_i, g_j), i \neq j \tag{5.15}$$

It is known that the higher the level of deformation, the higher would be the misorientation within a grain resulting from the stored dislocation content. Onset of recrystallization can lead to the decline of these values resulting from the introduction of relatively defect-free grains amongst the deformed matrix. The threshold of the GOS value [75] that distinguishes the local microstructural state (deformed or recrystallized) needs to be identified, which can then be used on the EBSD scans to partition the respective regions for the materials created under a range of thermomechanical conditions. As a qualitative starting point, we studied the variation of the GOS value [125] in the microstructures of the samples. Figure 16 shows the GOS map, where the colors represent the GOS values of the various regions of the microstructure.

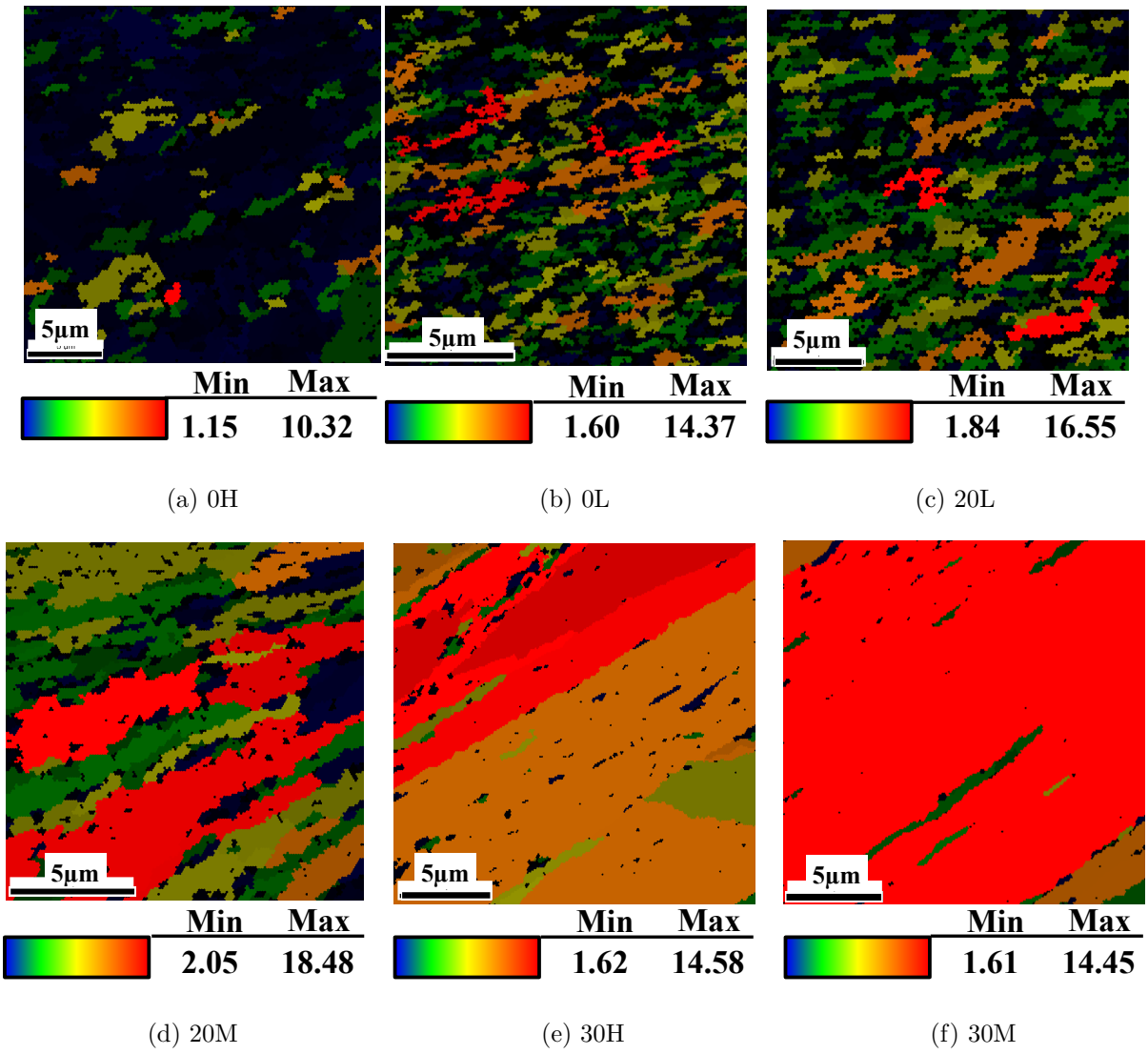

(a) 0H (b) 0L (c) 20L

(d) 20M (e) 30H (f) 30M

Figure 16: Grain Orientation Spread (GOS) maps with grains shaded associated to GOS values in degree (The maximum value represents red color).

It is immediately apparent that significant portions of the various microstructures resulting from severe strains show a low value of GOS that are interspersed by regions that show a high GOS value. Among the various microstructures, Figure 16a illustrates the microstructure for the 0H sample that was created from severe strains, but also a high temperature rise (Table 1), which is characterized by predominantly low values of GOS. Figure 15a and results of optical microscopy and electron microscopy showed that this sample has undergone rampant Dynamic Recrystallization (DRX) to result in a fully-coarsened, micro-scale grain structure [120, 5]. In contrast to this sample, the 30M sample (Figure 16f) shows predominantly high values of GOS that indicates a highly-defected microstructure that is likely unaffected by DRX phenomena.

For establishing a base-line, we use the microstructure in the 0H sample as one representing the fully dynamically recrystallized condition and for this condition we calculated the GOS distribution in Figure 17. In this figure a strong peak is discernible corresponding to the dominant orientation spread of a small GOS value. On this plot, the tail of the peak seem to be initiated roughly in the range 2° to 3°, which is essentially the cut-off value for the distribution that characterizes the 0H sample.

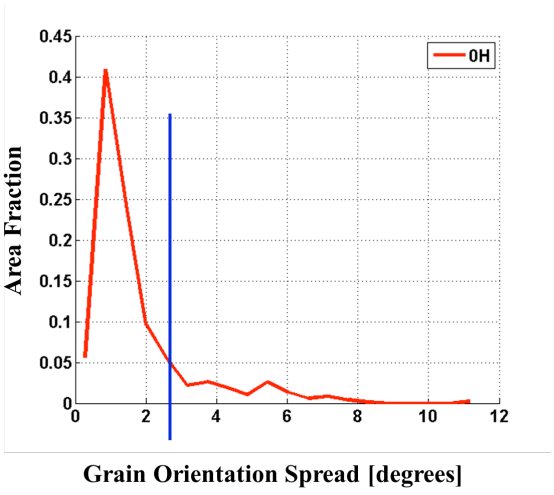

Figure 17: Grain Orientation Spread (GOS) distribution of 0H sample. The vertical line indicates the partitioning value.

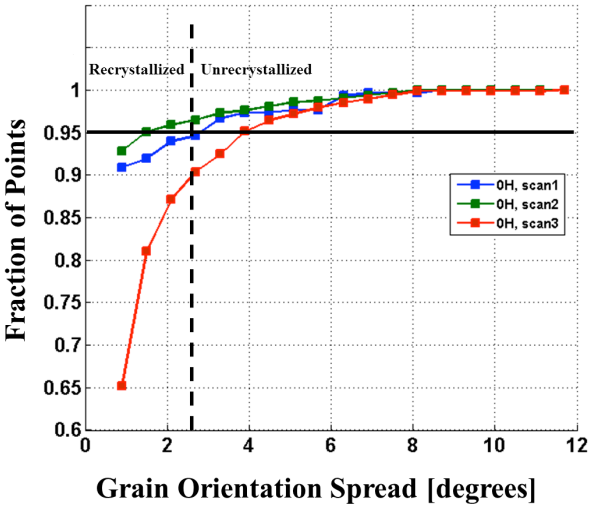

Figure 18: Variation of cumulative distributions of Grain Orientation Spread (GOS) for independent replicates 0H sample.

Figure 18 illustrates the cumulative distribution of the GOS for independent scans of three 0H samples. Setting a threshold of 95% as the threshold of transformation (see Refs. [45, 61, 9]) for this sample, it shows an average GOS threshold value (dashed line) of 2.6° that distinguishes the dynamically recrystallized portions of the microstructure from those that are not. This number is also quite consistent with that observed qualitatively in Figure 17. This GOS threshold is then used as a criterion to filter the microstructure scans to delineate the images of recrystallized and deformed grains which are depicted in Figure 16 second and third rows. In the second row in Figure 16, the IPF images depict the deformed grains for which the original scans are filtered to entail GOS values greater than 2.6°. Similarly, the third row images in Figure 16, show the recrystallized grains as a function of strain value comprising the GOS value less than 2.6°.

5.3.3 Quantifying Progression of Dynamic Recrystallization

A first step to measure the fraction of the dynamically recrystallized portions of the microstructure (f_{rec}) is by evaluating the area fraction of microstructure from EBSD having the GOS value less than 2.6°. The average value of the dynamically recrystallized fractions and the standard deviations were calculated for various scans/sample replicates across the different thermomechanical conditions and are listed in Table 3. 0H sample, as expected, has the highest value while the 30M sample has the lowest fraction. A plot of recrystallization fraction vs. strain is shown in Figure 19 for various conditions indicating a predominantly monotonic relation between the two parameters except for 0H sample, which was an outlier in this analysis. The insets in Figure 19, [insets (a), (b), (c)], show the evolution of grain boundaries as deformation progresses. This dependence is also evident from the IPF images in Figure 14, which are filtered to delineate the recrystallized portions of the microstructure using the aforementioned GOS-based approaches.

Analogous to Figure 19, we also sought to explore the role of strain-rate and temperature in determining the progression of dynamic recrystallization by plotting the recrystallization fraction as a function of $\ln(Z)$ parameter. However, a very weak correlation seemed to exist between these two parameters, at least in the range of empirically achievable LSM conditions examined here. Hence, we moved forward to examine the recrystallization fraction behaviour versus another analogous parameter "R" [3], a function of $\ln(Z)$ and material constants in the present work (Equation 5.8).

Traditional Discontinuous Dynamic Recrystallization (DDRX) is understood to proceed via the formation of new grains (often nucleated at grain boundaries), whose boundaries migrate to consume the driving force that is aided by the stored dislocation densities made available by the deformation. The growth ceases when the driving force declines or by the nucleation of mitigating grain boundaries [107]. We notice from an observation of the microstructures across the swathe of thermomechanical conditions considered here that predominantly, the grain structures for most of the conditions are ultrafine-grained, while that for 0H is a clear outlier, characterized by a coarse microstructure. It is likely that the high temperature involved during its formation lead to rampant DDRX, which is feasible, given

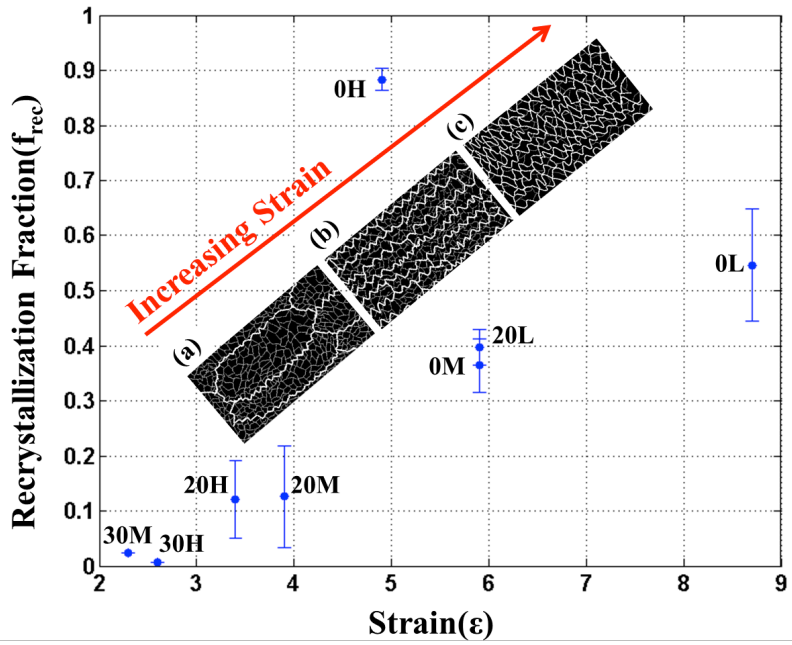

Figure 19: Recrystallized fraction increasing with effective strain (ϵ) for the various LSM samples listed in Table 1. The schematic insets show the mechanism of progression of Geometric Dynamic Recrystallization (GDRX). a) As deformation evolves, the increasing strain leads to progressive thinning of the grains which is accompanied by the serration of the original HAGB (thick white lines), b) Eventually these serrations meet and, c) result in a microstructure composed of refined grains encompassed by HAGB.

the mobility that is allowable under these temperature conditions. It has also been recognized that Dynamic Recrystallization (DRX) can occur via a more continuous evolution of high angle grain boundaries in a microstructure in ways other than the nucleation and growth of grains at pre-existing boundaries [107][85]. Such processes generally are often identified as Continuous Dynamic Recrystallization (CDRX). It should be noted that dynamic recrystallization need not necessarily be exclusively DDRX or CDRX, but a composite manifestation of both, depending on the deformation conditions. Nonetheless, CDRX is more typical in materials with low mobility of grain boundaries and high Stacking Fault Energy (SFE), while DDRX is more common in low to moderate SFE. However, CDRX does depend on the purity of the metals in addition to the deformation conditions and SFE [91]. It is known that the presence of the solute atoms and second phase particles which reduce the mobility of both dislocations and high angle grain boundaries lead to a preponderance of CDRX. Here, we should point out that OFHC copper used in machining is not ultrapure and it is not unreasonable to expect CDRX. Also, a continuum of microstructures is discernible across the various ultrafine structures in Figure 14, excepting the 0H condition and there does not appear to be recognizable discontinuous evolution associated with "nucleation" and "growth" characterizing DDRX [107].

To further understand the evolution of DRX, we measured the length fraction of High Angle Grain Boundaries (HAGB) for the microstructures using the OIM data for samples resulting from the various conditions. This fraction (f_{HAGB}) is calculated and averaged for different scans in each sample condition and are summarized in Table 3. When we plot the HAGB fraction (f_{HAGB}) as a function of the recrystallized fraction (f_{rec}) in Figure 20, we note a monotonic increase. This indicates that as the recrystallization fraction increases, the resulting regions are likely to be predominantly surrounded by HAGB. This apparently smooth trend across the various thermomechanical conditions further implicates an underlying mechanism that involves a more continuous microstructure transformation akin to that identified with CDRX [107]. Note that the microstructure transformation occurs smoothly and jumps to 0H sample on this plot with highest value of HAGB and recrystallization fractions, although the strain level in 0H is not at the highest among the samples considered here. This aspect of 0H sample is in line with our earlier hypothesis of it being a result

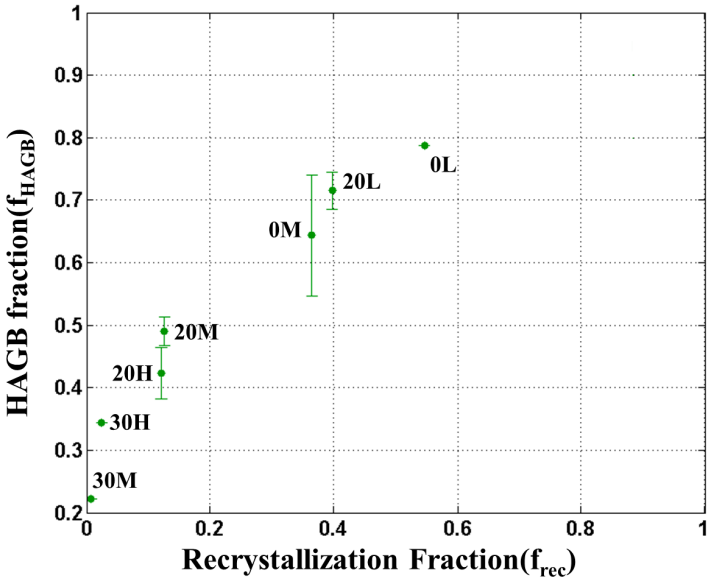

Figure 20: Correlation between the recrystallized fraction and the High Angle Grain Boundary (HAGB) fraction for different sample conditions as listed in Table 1.

of DDRX under the high temperature deformation conditions. Taken together, it appears that a majority of the samples appear to undergo a continuous transformation and accumulation of recrystallized regions as a function of the deformation, until high temperatures are introduced (0H sample), where DDRX appears predominant. This conclusion is somewhat analogous to that in a related study of dynamic recrystallization of copper deformed to moderate strain ($\gamma \approx 3-4$) at high strain rate (10^4 $/s$), which partly coincide with the conditions examined here [12].

5.3.4 Geometric Dynamic Recrystallization Advances (onset of GDRX)

An important attribute distinguishing CDRX and DDRX is the difference in the evolution of the textures following their progression. DDRX is characterized by a strong deformation texture transformation, while in CDRX the texture change is gradual in general and is often retained [37, 62]. Detailed texture analysis of the samples from LSM is ongoing to provide further validation to the ideas presented here [107, 6]. Two overarching classes of CDRX

have been considered [107]. One is as Geometric Dynamic Recrystallization (GDRX) and the other process involves formation of new grains with high angle boundaries by gradual rotation of subgrains with little accompanying boundary migration, i.e. rotational recrystallization, which has been recognized in geological minerals and in metals such as magnesium and aluminium alloys [107].

GDRX occurs during deformation involving elevated temperatures and typically proceeds in a manner as shown in the insets (a), (b), and (c) in Figure 19 [107]. During deformation the original grains usually become increasingly thin and flattened [Figure 19, inset (a)]. The progressive flattening/pancaking or the original grain boundaries leads to a decreased thickness with increasing strain values. However, with interplay of dynamic recovery involving losses of dislocation densities, the boundary tensions of the intermediary subgrain walls that coax local grain boundary migration can lead to a simultaneous serration of these grain boundaries [107]. Note that as the deformation progresses, the original HAGB that are now serrated and depicted by thick lines in Figure 19, inset b, become closer. However, the subgrain sizes shown by thinner gray lines that evolve in response to the thermomechanical conditions remain characteristically constant in size [107]. Eventually the serrated HAGB's impinge on each other and lead to the creation of a microstructure composed increasingly of high angle boundaries [Figure 19 inset (c)]. In effect, the grains will pinch into new smaller grains as depicted in Figure 19. Another characteristic of this mechanism is that because the wavelength of the serrations are comparable to the intervening subgrain structure, the DRX grains composed of HAGB that result from "pinching-off" of the original grain are essentially of a size that is comparable with the subgrain size [107].

This mechanism of GDRX will be dependent on the initial grain size (δ_0) in addition to the deformation parameters. It has been argued that the necessary condition for the GDRX [107] as: the grain impingement occurs when the subgrain size (δ) is equal to the width of the grain. Therefore, the critical strain (ϵ_{cr}) for the process is in this form:

$$\epsilon_{cr} = \ln\left(\frac{K_1\delta_0}{\delta}\right) \tag{5.16}$$

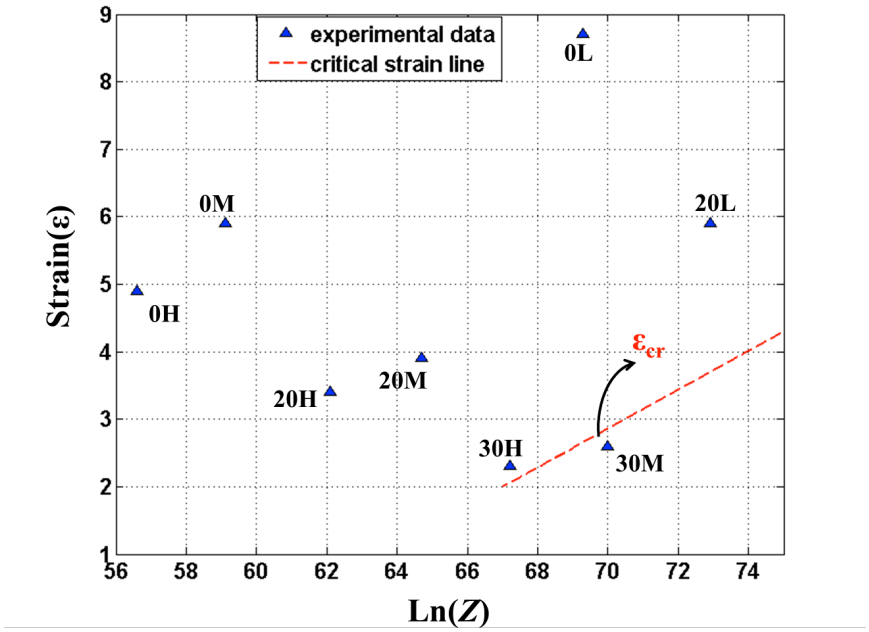

Figure 21: Critical strain (Equation 5.18) for the onset of GDRX shown on ϵ-ln(Z) space with the experimental conditions overlaid as listed in Table 1.

where K_1 is a constant. It has been argued in [107], using the relationship between the flow stress, the Zener-Hollomon parameter (Z), subgrain size and Equation 5.16 that the critical strain for onset of GDRX is:

$$\epsilon_{cr} = \ln\left(Z^{1/m}\delta_0\right) + K_3 \tag{5.17}$$

where m and K_3 are constants. Noting the linearity of the relationship between the critical strain and ln(Z), it is useful to investigate the overlap of this criterion with the empirical data in this study, by examining the results as a function of the strain (ϵ) at which they were created and the ln(Z) value corresponding to that in the deformation zone (Table 1). Unfortunately, the constants for Cu in the deformation regime characterized by LSM are unavailable. Therefore, we sought to utilize our empirical data to identify these constants that characterize the existing GDRX modeling framework. Figure 21 illustrates the thermo-mechanical conditions corresponding to the various experimental parameters on a space with

the x-axis as $\ln(Z)$ and the effective strain (ϵ) as the y-axis. Table 3 reveals that among the various samples, the 30M and 30H samples are characterized by the lowest fractions of recrystallization (f_{rec}) values determined using OIM. The neighbouring 20M and 20L samples are characterized by substantially greater f_{rec} values. Therefore, we take the 30M and 30H samples to form the critical threshold for GDRX and use the thermomechanical conditions associated with these samples in Equation 5.17 to back calculate the parameter m to be 3.47 and K_3 as -7.4. The line corresponding to this critical threshold, i.e. Equation 5.17 is then plotted in Figure 21. Also, note that to enable this analysis, the original grain size (δ_0) needs to be determined. Here, we measured the initial grain size using Heyn intercept method [4] applied to images obtained from optical microscopy of machined copper samples being polished and then etched from which the value is obtained as 50 μm. Thus, Equation 5.17 can be written as:

$$\epsilon_{cr} = \ln\left(Z^{1/3.47}0.00005\right) - 7.4 \tag{5.18}$$

and accordingly, the critical strains for sample conditions are listed in Table 3.

The fidelity of the framework for identifying the threshold for GDRX can be improved using models for subgrain sizes resulting from LSM-relevant deformation conditions. One such a model is proposed by our earlier study [3] which encapsulated the variation of subgrain sizes (δ) as a function of the effective strain (ϵ) and the parameter R defined as in Equation 5.8 and as it was shown, the subgrain size varies as in Equation 5.9 [3]. The knowledge of this functional variation offers a direct route for defining the criterion for onset of GDRX using Equation 5.16:

$$\epsilon_{cr} = \ln\left(\frac{K_1'\delta_0}{0.25 - 0.030\epsilon_{cr} + 0.058R + 0.0003\epsilon_{cr}R}\right) - 7.4 \tag{5.19}$$

where K_1' is considered as a constant here to avoid confusion from Equation 5.16. Equation 5.19 of course, is an implicit equation, and by assuming that the 30M sample is the condition that is the threshold for the onset of GDRX, we obtain . Then, the critical strains for the onset of GDRX were calculated for the various deformation strain and temperatures

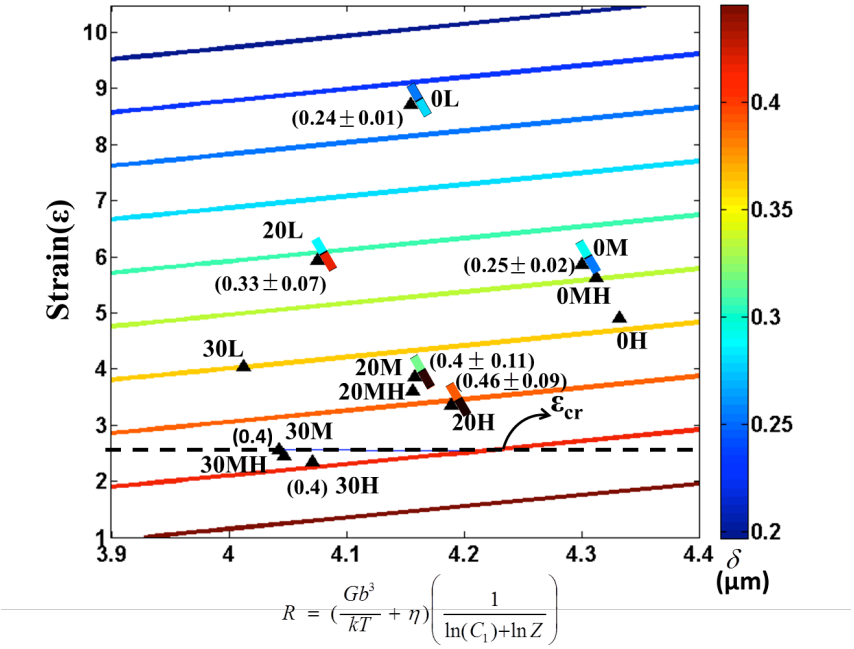

Figure 22: Critical strain for onset of GDRX evaluated using Equation 5.19 shown on ϵ-R space with the experimental data overlaid [3]. Average subgrain sizes along their standard deviation for the experimental conditions are marked beside the data points. Also, at the various points, the mean + the standard deviation and mean − standard deviation are depicted in the same color code associated with subgrain size contours.

using the corresponding R values (Table 1). In our approach, R can be thought to become a more empirically validated analogue of $\ln(Z)$ (the merits of both parameters are discussed in detail in Refs. [120] and [3]). Also, note that Equation 5.19 required fitting for only K_1', unlike the adaptation of existing GDRX model from Ref. [107]. Comparing the variation of R values to $\ln(Z)$, we notice that the parameter R shows a very weak sensitivity to changes in thermomechanical conditions in the GDRX context as well while $\ln(Z)$ values varies more strongly across the conditions considered here.

The critical strains using R values from Table 1 are used to delineate the line on a ϵ-R space in Figure 22, onto which the experimental data of subgrain sizes from our recent investigation [3] is also overlaid. Comparing Figures 21 and 22, we notice that both criteria

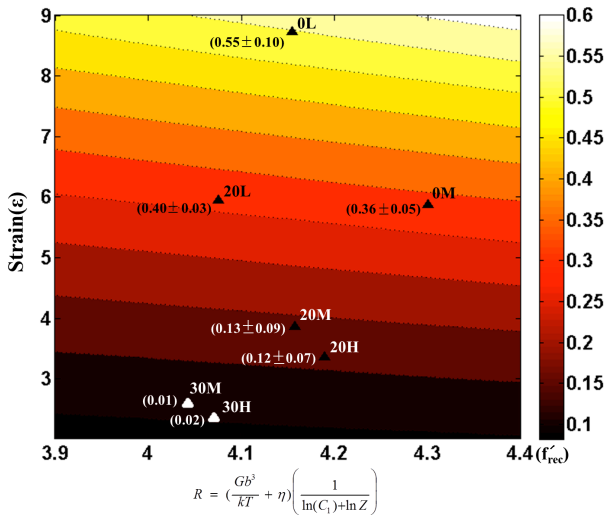

Figure 23: Contour map of the recrystallization fraction (f'_{rec})as a function of effective strain (ϵ) and R. Values of average recrystallization fraction and its standard deviation from experimental conditions are marked on the plot. At each experimental point, the mean measured f_{rec} + standard deviation and − standard deviation are shown.

appear fairly consistent in terms of determining the criterion for GDRX among the examined sample conditions. Although, our derivation is based on our subgrain size model, while that in Figure21 is obtained from a more traditional approach to examining hot deformation. We also sought to encapsulate the variation of the recrystallization fraction (Table 3) in relation to the threshold for GDRX on the ϵ-R space, which essentially captures the extent of progression of the formation of the low GOS, HAGB-dominated, defect-free structures amongst the deformed matrix. We find that Equation 5.20, with coefficient of determination of $R^2 = 0.913$ offers a good approximation of the variation of the recrystallization fraction across the range of thermomechanical conditions here:

$$f'_{rec} = 0.05R^{1.498}\left(\exp(0.095\epsilon) - 1\right) \tag{5.20}$$

The recrystallization fraction calculated using this equation (f'_{rec}) is listed in Table 3, which except for low strain conditions (specially 30M and 30H) has a close correspondence with the empirically measured values (note that we have excluded 0H sample in this approximation because of our expectation that it is a product of DDRX under the substantially elevated deformation temperatures associated with its formation). The contour map corresponding to Equation 5.20 is illustrated in Figure 23 and the experimental measurements are overlaid along with the standard deviation in parenthesis. This equation provides an empirical fit, whose choice is driven by the consideration that at a constant temperature, we expect the fraction to increase with strain and equate to zero when there is no deformation ($f'_{rec}|_{\epsilon=0} = 0$). Complementing this is the interactive effects of temperature and strain-rate that are coupled via the parameter R, where R usually increases with increasing temperature for the range of deformation conditions here. We expect the recrystallization fraction to increase as the temperature increases, which is captured via a power-law fit in Equation 5.20.

5.4 DISLOCATION DENSITY MAPPING

Evolution in microstructure of materials undergoing plastic deformation happens through multiplication and storage of dislocations. While this phenomenon has been studied for various deformation condition ranges, a knowledge gap remains in determining dislocation density evolution at high strain ($(\epsilon \sim (1 - 10))$ and high strain-rate ($\dot{\epsilon} \sim (10 - 10^3\ /s)$ deformation conditions.

Dislocation densities are measured using peak profile broadening analysis using X-ray diffraction (XRD) in a Bruker X-ray diffractometer equipped with a Lynx Eye detector having a resolution of 0.037°. This technique is based on quantification of broadening of X-Ray Diffraction (XRD) peaks of crystallographic planes, which happens due to dislocations introduced during deformation and the finite crystallite size effect [66]. To do this, XRD patterns from bulk and machined samples were obtained around the (220) crystallographic plane of Cu, using a Phillips PW 1830 powder X-Ray diffractometer. The (220) plane was chosen for analysis as this is the most prominent peak in the XRD profile of Cu and would

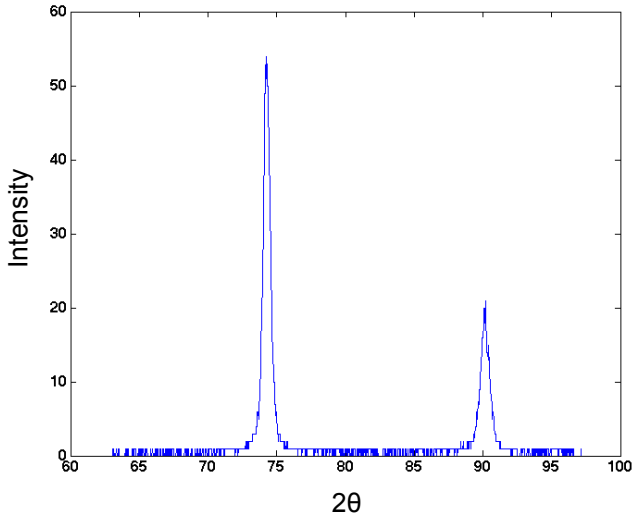

Figure 24: XRD profile of Cu chip sample. The peak around 2θ value of 74.5° signifies the (220) crystallographic plane.

therefore provide better signal to noise ratio. A source with X-ray wavelength $\lambda = 1540\ nm$ was used with a scan step size of 0.03°. Figure 24 shows the X-ray diffraction profiles of the 30L chip around a 2θ value of 74.5° corresponding to the (220) plane of copper from which the $K\alpha 2$ peak has been stripped. The resulting scans were utilized to calculate the dislocation densities ρ in the previously defined machined samples using various machining parameters (cutting velocities and tool rake angles). To calculate dislocation densities, the asymptotic parts of the second and fourth moments of the $I(q)$ vs. q curve were fitted to the following pre-determined forms of the moments [21] according to [145] and [22]:

$$M_2(q) = \frac{1}{\pi^2 \epsilon_F} q - \frac{L}{4\pi^2 K^2 \epsilon_F^2} + \frac{\Lambda \langle \rho \rangle \ln(q/q_0)}{2\pi^2} \tag{5.21}$$

$$\frac{M_4(q)}{q^2} = \frac{1}{3\pi^2 \epsilon_F} q + \frac{\Lambda \langle \rho \rangle}{4\pi^2} + \frac{3\Lambda \langle \rho \rangle \ln(q/q_1)}{(2\pi)^4 q \epsilon_F} + \frac{3\Lambda^2 \langle \rho^2 \rangle \ln^2(q/q_2)}{4\pi^4 q^2} \tag{5.22}$$

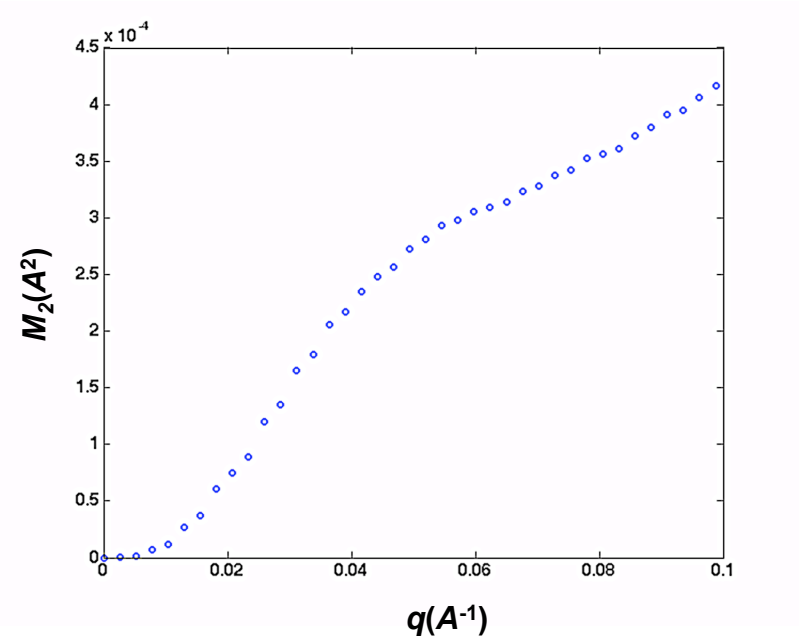

Figure 25: 2^{nd} order restricted moment (M^2) in Cu, 0L sample condition.

where, $M_k(q) = \int_{-q}^{q} q'^k I(q')dq' / \int_{-\infty}^{\infty} I(q')dq'$ with $I(q)$ being the XRD peak intensity at $q = \frac{2}{\lambda}(\sin\theta - \sin\theta_0)$, where θ_0 is the Bragg angle, θ is the diffraction angle and λ is the wavelength of the X-ray. The (220) XRD peak was used giving $\theta_0 = 74.5°$ for (220) peak of Cu. Here, $\langle\rho\rangle$ and $\langle\rho^2\rangle$ are the average dislocation density and squared average dislocation density, respectively. K is the Scherrer constant ($K \sim 1$), ϵ_F is the crystallite size and q_0, q_1, and q_2 are the fitting parameters [22]. The dislocation densities are obtained by fitting Equation 5.22 to the asymptotic part of $M_4(q)/q^2$. This method provides a level of verification as that value of dislocation density is chosen for which the 2^{nd} and 4^{th} order of the moments produce the same crystallite sizes (from Equations 5.21 and 5.22 respectively). This X-ray diffraction analysis was performed for both the severely deformed chip.

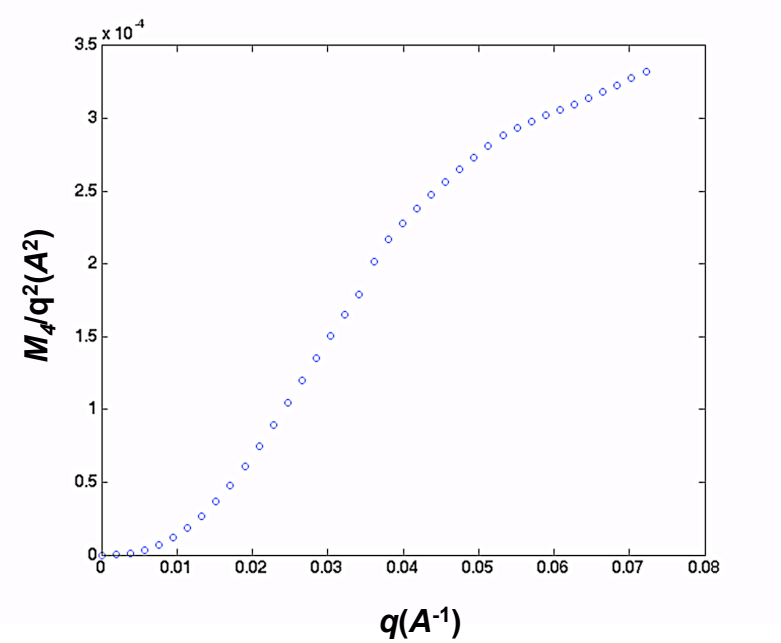

Figure 26: 4^{th} order restricted moment divided by q^2 (M^4/q^2)in Cu, 0L sample condition.

The second and fourth moments are plotted in Figures 25 and 26 respectively. Dislocation densities were measured using X-Ray peak profile broadening analysis and were calculated using the method of moments. This was done by calculating $M_2(q)$ and $M_4(q)/q^2$ from the profile and fitting to the right hand side of Equations 5.21 and 5.22 to the asymptotic part of the curves (Figures 25 and 26) respectively so that both equations produced the same crystallite size. The resulting dislocation densities are listed in Table 4.

It is well known that increasing amounts of plastic deformation in metals entails progressively higher density of dislocations. This is readily visible in the ρ values obtained from the chip. For example, conditions corresponding to comparable strain-rates, i.e., 20L ($\epsilon = 5.9$, $\dot{\epsilon} = 80\ /s$) possessed $\rho = 7.4 \times 10^{15}\ /m^2$ while 30L ($\epsilon = 4.0$, $\dot{\epsilon} = 100\ /s$) shows $\rho = 4.5 \times 10^{15}\ /m^2$, which show increased amount of dislocation density for higher deformation. In a similar comparison 40L ($\epsilon = 2.6$, $\dot{\epsilon} = 140\ /s$) has $\rho = 3.3 \times 10^{15}\ /m^2$, which has a lower dislocation density value comparing with the value for 20L. An outlier in this investigation is 0L condition ($\epsilon = 8.7$, $\dot{\epsilon} = 60\ /s$). Although the level of strain is the

maximum among all sample conditions, it is noticeable that the value for the average total dislocation density is not the highest. Surprisingly, the dislocation density for this condition is even lower comparing with 20L condition ($\epsilon = 5.9$, $\dot{\epsilon} = 80\ /s$) which includes lower strain but comparable strain-rate. This unexpected observation can be rooted in high fraction of HAGB in 0L condition as shown in Figure 20. As reported in Ref. [57], the very small and lenticular shaped subgrains are nearly dislocation free volumes, surrounded by medium to high angle boundaries, that fill spaces that are external to the cell blocks.

Another criterion affecting storage/annihilation of dislocation is the strain-rate during LSM deformation. Of course, in the thermomechanically coupled state characterizing LSM, a higher strain-rate also leads to a higher rate of dissipation of plastic work as heat resulting in higher temperature rise in the primary deformation zone and the freshly generated surface, that annihilate stored dislocations. For example, the sample conditions 40L ($\epsilon = 2.6$, $\dot{\epsilon} = 140\ /s$), and 40M ($\epsilon = 2.1$, $\dot{\epsilon} = 1930\ /s$), exhibit significantly different dislocation densities ($\rho = 3.3 \times 10^{15}\ /m^2$ and $\rho = 1.2 \times 10^{15}\ /m^2$ respectively), while undergoing similar strains, wherein the higher strain-rates that involve correspondingly higher temperatures in the deformation zones (Table 1), lead to lower dislocation densities. The same rule exists for 0M and 20L(Table 1 and 4). This is characteristic of the rampant dynamic recovery phenomena that often characterize such deformation conditions.

To understand the thermomechanical phenomena underlining microstructure refinement during SPD in LSM, we sought to develop a suitable space to encapsulate the observed variation of the dislocation densities as a function of the central deformation variables: $\epsilon, \dot{\epsilon}$, and T. In deformation at elevated temperatures, the effect of strain-rate and temperature couple together via the Zener-Hollomon (Z) parameter. Further, we derive from our previous work [3], in which subgrain sizes (δ) resulting from SPD are mapped in a space where the y-axis is the effective strain and the x-axis is the parameter R being a function of the form $R \propto (\frac{a}{T} + b)(\frac{1}{c+\ln Z})$, according to Equation 5.8.

In this space [3], the subgrain size (δ) is shown to be positively correlated to R as $\delta \propto R$. Now, based on the principle of scaling, in accordance with microstructural view, similitude results in $\rho_i \propto 1/\delta^2$ [94], where ρ_i is the dislocation within the cells. The density of stored dislocations, ρ, is the total dislocation, calculated from the dislocation within the cells (ρ_i) and dislocations in cell walls (ρ_b) as $\rho = (1-f)\rho_i + f\rho_b$, where f is the volume fraction of boundaries consisting the cell structures considered as 0.2 [94].

The result of XRD experiments will render the total stored dislocations (dislocations in cell walls (ρ_b) besides dislocations within the cells (ρ_i)) and since the total dislocation densities correlate with the dislocations within the cells according to $\rho = (1+f(q_b^2-1))\rho_i$ [94], it can be concluded that $\rho \propto 1/\delta^2$ (Note that q_b is a microstructure scaling parameter as $q_b = \sqrt{\rho_b/\rho_i}$ equal to 5, the value of which is discussed in [94]). We therefore expect the stored dislocation density to be correlated with a parameter of the form $\rho \propto 1/R^2$. Following a regression analysis, we populated a phase-space here where the y-axis is the effective strain and the x-axis is $1/R^2$ according to the following equation:

$$\rho_r = 1.75 \times 10^{13} + 1.12 \times 10^{15}\epsilon + 11632\frac{1}{R^2} \tag{5.23}$$

Implicitly, such an effort envisages a bijective map-space for projecting the microstructure response as a function of LSM thermomechanical parameters. Creating such RSM map, would essentially map each point on this space to deformed microstructural characteristics in a one-to-one manner, thus offering a simple framework for predicting microstructure response for intermediary conditions once such mappings are adequately delineated. Figure 27 illustrates this idea for dislocation densities.

For the range of LSM parameters in Table 4, Equation 5.23 captures the variation of dislocation densities across the thermomechanical conditions as a function of ϵ and $1/R^2$, which form the elements of the RSM framework. Using this equation, the total dislocation densities (ρ_r) for various conditions as listed in Table 4, are in reasonable agreement with measured values. Note that this estimation has excluded the 0L condition since as mentioned above, the thermomechanical parameters of this sample has shown to be an outlier.

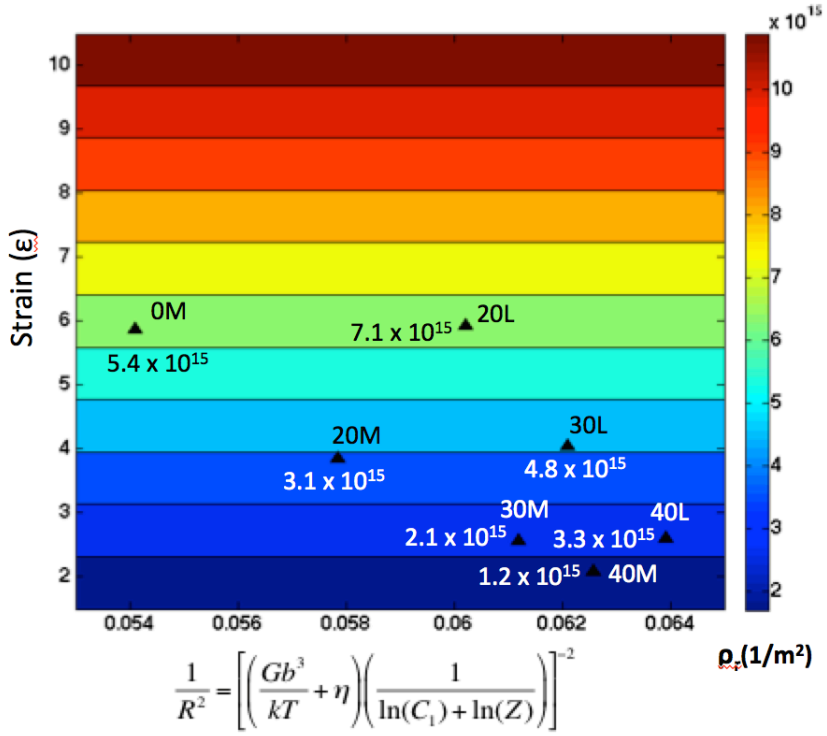

Figure 27: RSM Map of the dislocation density, ρ_r as a function of effective strain (ϵ) and $1/R^2$ using Equation 5.23. Values of average dislocation densities for experimental conditions are marked on the plot.

In Figure 27 contour maps of dislocation densities depict the variation over the range of strains, strain-rates and temperatures according to Equation 5.23. Note that on this space, experimentally measured values for chip dislocation densities are shown for the corresponding deformation conditions. Note the positive correlation with the strain term in Equation 5.23, which matches the expectation of higher dislocation densities with increasing levels of deformation strains (ϵ). Furthermore, with decreasing deformation temperature, R usually increases across the conditions considered here and therefore for a constant value of strain, Equation 5.23 should manifest a positive correlation to ensure an increasing dislocation density with decreasing deformation temperature.

Using the values of total dislocation density (ρ_r), the dislocation within cells, ρ_i, is also estimated and listed for different sample conditions. Finally, the results for similitude is calculated and shown in Table 4 as well. In Figure28, the results of similitude across the strain values for various sample conditions are plotted. According to the principle of scaling the microstructure is "self-similar" for various strain levels excluding for the scale [94]. Interestingly, the results in this plot agree well with the values reported in [94] where the reasonable values for microstructural scaling relationship of the form $\delta\sqrt{\rho_i}$, is considered in the range 5 to 10 which coincide quite well with the values obtained for the sample conditions in Table 4. However, as it is noticeable from the plot, it appears to follow a monotonic trend with increasing level of strain of the sample conditions. Ongoing research of this analysis is under study.

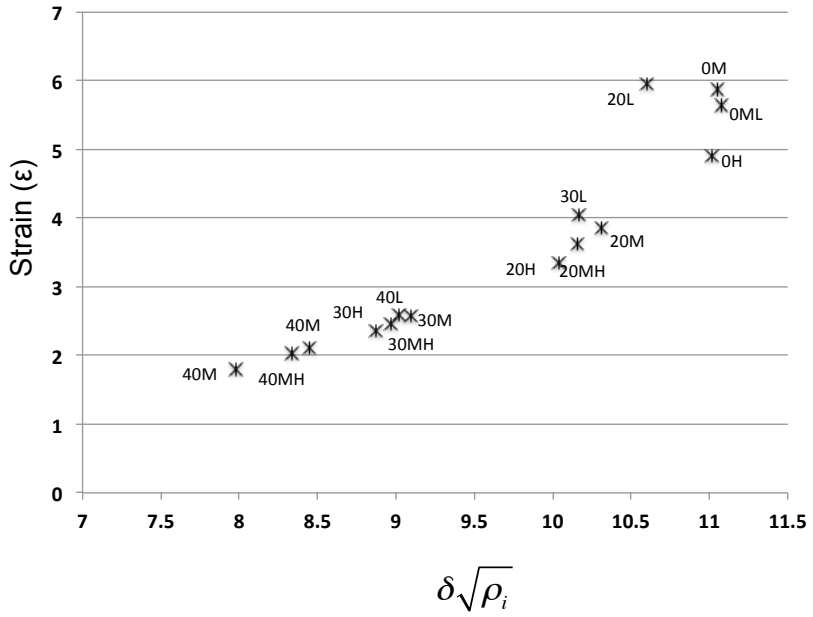

Figure 28: Results of similitude relationship, $\delta\sqrt{\rho_i}$, accros the strain values for different sample conditions.

Table 4: Deformation conditions (effective strain (ϵ) and $1/R^2$), and the measured dislocation densities (ρ_m) for the various machining samples. The dislocation densities are calculated using Equation 5.23 as ρ_r. Using ρ_i the results of similitude are listed.

Samples	ϵ	$1/R^2$	ρ_m $1/m^2$	ρ_r $1/m^2$	ρ_i μm	$\delta\sqrt{\rho_i}$ $1/m^2$
0L	8.7	0.058	$(4.7 \pm 0.3)E + 15$	-	-	-
0M	5.9	0.054	$(5.4 \pm 0.7)E + 15$	6.6E+15	1.1E+15	11.05
0MH	5.6	0.054	-	6.3E+15	1.1E+15	11.08
0H	4.9	0.053	-	5.5E+15	9.5E+14	11.02
20L	5.9	0.060	$(7.4 \pm 0.9)E + 15$	6.7E+15	1.2E+15	10.60
20M	3.9	0.058	$(3.1 \pm 0.6)E + 15$	4.3E+15	7.5E+14	10.31
20MH	3.6	0.058	-	4.1E+15	7.0E+14	10.16
20H	3.4	0.057	-	3.8E+15	6.5E+14	10.03
30L	4.0	0.062	$(4.5 \pm 0.3)E + 15$	4.5E+15	7.8E+14	10.17
30M	2.6	0.061	$(2.1 \pm 0.2)E + 15$	2.9E+15	5.0E+14	9.10
30MH	2.5	0.061	-	2.8E+15	4.8E+14	8.97
30H	2.3	0.060	-	2.7E+15	4.6E+14	8.87
40L	2.6	0.064	$(3.3 \pm 0.4)E + 15$	2.9E+15	5.1E+14	9.01
40M	2.1	0.063	$(1.2 \pm 0.5)E + 15$	2.4E+15	4.1E+14	8.44
40MH	2.0	0.062	-	2.3E+15	3.9E+14	8.34
40H	1.8	0.062	-	2.0E+15	3.5E+14	7.98

6.0 MAXIMIZING THE METASTABILITY OF HIGH-STRENGTH NANOSTRUCTURED METALS FROM SEVERE PLASTIC DEFORMATION

Progressive microstructure refinement during Severe Plastic Deformation (SPD) follows the familiar progression through the creation of dislocation entanglements that involve small crystal misorientations. Progressive deformation leads to these interfaces that become increasingly refined and misoriented and thus, constituting effective barriers of dislocation slip, which strengthens the material. This strengthening at smaller levels of strain (usually < 4) is monotonic, but at larger strain values, saturates to a characteristic values of yield strength and hardness. However, from a stability point of view, highly refined interfaces characterized by large misorientations are readily available nuclei for recrystallization when exposed to thermal agitation. Thermally induced growth of these nuclei leads to degradation of the material strength and compromises the utility of the Ultrafine Grained (UFG) and nanostructured materials from SPD. It is self evident that postponing the nucleation and growth of the incipient nuclei is crucial for suppressing thermal degradation of material strength. Rampant growth of the nuclei during thermally induced coarsening microstructures leads to recrystallization of increasing fractions of the material, which involve large declines of material strength. According to this explanation, the question we seek to answer here is the possibility to create nanostructured materials with maximize strength, but still suppressing the availability of nuclei for future recrystallization.

Microstructure control in plastic deformation systems relies on combinatorial approaches involving suitable choices of deformation strain, strain-rate and temperatures. In our previous models, the effects of strain-rate and temperature have been coupled using the parameter R in Equation 5.8 which was used to create phase spaces parameterized as functions of strain

and R mapping thermomechanical conditions to unique deformed microstructures. A versatile microstructure response test by SPD across a swathe of $R - \epsilon$ combinations within a simple-shear, plane-strain deformation configuration was suggested by the utilization of the large strain machining (LSM) process.

Now, reliably scanning across the ranges of R and ϵ values in a prototypical material like Cu can be utilized to manipulate the density of defects and the level of microstructure deformation. We chose to focus only on those conditions, which impose a strain > 2 in Cu. Usually, this is the SPD level beyond which, the Hardness value (or yield strength) saturates to a value of $\sim 1.5\ GPa$. Much of the existing research on nanostructured metals from SPD has focused on the imposition of large strains at small strain-rates, nominally at room temperatures to create highly refined grain structures encompassed by high angle boundaries. It has also become apparent that while large strains are necessary to achieve this saturation strength, the concomitant refinement inevitably makes available the nuclei for future recrystallization. Therefore, instability is congenital to high strength nanostructured metals from conventional SPD. With this knowledge, we sought to focus on moderate levels of strain, at somewhat higher strain-rates and temperatures to pursue the creation of strong materials, where the accumulation of dislocations is encouraged at large strains, but their progressive storage into refined high angle misoriented structures is inhibited by dynamic recovery. It is notable that lower strain-rates replicate conventional SPD samples and higher rates lead to dynamically recrystallized structures. This investigation is studied in the following sections of current chapter.

6.1 DYNAMIC RECOVERY CRITERION (R_{CRIT}) CALCULATION

In order to examine the possibility of creating microstructures with above conditions (highly refined, with high strength), we sought to focus on imposing high levels of deformation at somewhat high strain-rates and the coupled temperatures to pursue the creation of strong materials, where the accumulation of dislocations is encouraged at large strains, but their progressive storage into refined high angle misoriented structures is inhibited by dynamic recovery. Hence, the aforementioned condition can be written as:

$$\frac{dH}{dt} >> \frac{d\rho_i^-}{d\gamma} \tag{6.1}$$

with H being the grain thickness in the normal direction. The idea here is to accomplish the microstructure refinement condition through thinning of the grains/subgrains and high strength condition by imposing the thinning rate to occur before rampant dynamic recovery takes place.

Dynamic recovery leads the "serration" of the grain boundaries. The serrated grain boundaries are a critical step in Geometric Dynamic Recrystallization (GDRX). The HAGBs surrounding the refined grain are the preferred nuclei for subsequent recrystallization during heat treatment. Consequently, if we prevent the "serration" phenomenon, we are inherently eliminating GDRX and preventing the formation of nuclei.

We started examining this by starting from the thinning process while high levels of deformation are imposed. In deformation of a polycrystalline metal, the following geometric relationship explains the relationship between the grain thickness in the normal direction (H), strain (ϵ) and the initial grain size D_0:

$$H = D_0 \exp(-\epsilon) \tag{6.2}$$

It would be desirable that the microstructure refinement through thinning of the subgrain sizes occurs before rampant dynamic recovery phenomenon, 6.1. This condition can be expressed as the rate of thinning to be faster than the dynamic recovery rate described by the derivative of Equation 6.2 as:

$$\begin{aligned} \ln(\frac{H}{D_0}) &= -\epsilon \\ \frac{1}{H}\frac{dH}{dt} &= -\dot{\epsilon} \\ \frac{dH}{dt} &= -\dot{\epsilon}H \end{aligned} \tag{6.3}$$

The thinning rate can be described by Equation 6.3, while the dynamic recovery rate, with the assumption of dislocation climb as the controlling reaction which leads the "serration" of the grain boundaries, is given by Equation 6.4 as a function of density of free dislocations inside subgrains (ρ_i) [94]:

$$\frac{d\rho_i^-}{d\gamma} = -2\rho_i^2 b^2 \xi_\rho B_\rho \frac{\nu_D}{\dot{\gamma}} \exp(\frac{U_{SD}}{kT}) 2\sinh(\frac{\xi_\rho G B^4 \sqrt{\rho_i}}{kT}) \tag{6.4}$$

where b is the burgers vector, ξ_ρ is a dynamic stress intensity factor, B_ρ is a constant, ν_D is the Debye frequency, U_{SD} is activation energy of self-diffusion in Cu equal to 3.271×10^{-19} $J/atom$ [77], k is Boltzmann's constant, T the deformation temperature and G the shear modulus [94].

Substituting Equations 6.3 and 6.4 in Equation 6.1 we will have:

$$H >> 2\rho_i^2 b^2 \xi_\rho B_\rho \frac{\nu_D}{\dot{\gamma}} \exp(\frac{U_{SD}}{kT}) 2\sinh(\frac{\xi_\rho G B^4 \sqrt{\rho_i}}{kT}) \tag{6.5}$$

Using the result of dislocation densities within subgrains from section 5.4, we calculated the right side of Equation 6.5 as R_{crit} listed in Table 5.

As R_{crit} is a criterion for the dynamic recovery to happen, the sample with the smallest value of R_{crit} with respect to H is expected to include the least nuclei. We sought to encapsulate the variation of $\log R_{crit}$ across the themomechanical conditions as a function of ϵ and R according to:

$$(\log R_{crit})_r = 140 + 10\epsilon - 30R \tag{6.6}$$

The values calculated from Equation 6.6 are enumerated in Table 5 confirming a good agreement with the measurements. We are interested in refined microstructure (deformation > 2) with lowest value of R_{crit} and among the samples created; 30 and 40 rake angle samples can best fit into these conditions. Hence, we try to find the optimized thermomechanical condition in order to create microstructure with highest refinement possible, while lowest R_{crit} (comparable to 30 and 40 rake angle conditions) in the range of achievable machining thermomechanical parameters. In section 6.2, we applied $Kuhn - Tucker$ (or $Karush - Kuhn - Tucker$) optimality necessary conditions to solve this problem.

6.2 KARUSH-KUHN-TUCKER OPTIMALITY NECESSARY CONDITIONS

The objective in this problem is to minimize the subgrain size function in order to achieve the maximum refinement possible according to:

$$\delta(\epsilon, R) = 0.25 - 0.03\epsilon + 0.058R + 0.0003\epsilon R \tag{6.7}$$

subject to the dynamic recovery rate criterion constraint:

$$\log(R_{crit}) = 140 + 10\epsilon - 30R = 48.61 \tag{6.8}$$

(note that this constraint is obtained through equating the dynamic recovery relation, Equation 6.6), with the average $\log R_{crit}$ values for 30 and 40 rake angle sample conditions.)

Table 5: R_{crit} as a criterion for the dynamic recovery to happen. $\log(R_{crit})$ is calculated using Equation 6.5 and $(\log R_{crit})_r$ is estimated using Equation 6.6 for various sample conditions.

Samples	R_{crit}	$\log(R_{crit})$	$(\log R_{crit})_r$
0L	1.8E+107	107.3	102.6
0M	3.3E+73	73.5	69.7
0MH	7.2E+70	70.9	66.9
0H	9.2E+63	64.0	59.1
20L	5.4E+90	90.7	77.2
20M	1.1E+63	63.0	53.8
20MH	2.2E+60	60.3	51.4
20H	1.1E+56	56.0	47.9
30L	3.4E+75	75.5	60.0
30M	1.3E+53	53.1	44.4
30MH	1.7E+51	51.2	43.1
30H	4.1E+48	48.6	41.4
40L	1.3E+60	60.1	47.3
40M	1.7E+48	48.2	41.0
40MH	6.1E+46	46.8	40.2
40H	7.2E+42	42.9	37.9

And the achievable machining sector:

$$-37.1R^2 + 270R - 490.3 + \epsilon \leq 0 \tag{6.9}$$

$$-40.9R^2 - 326R + 652 - \epsilon \leq 0 \tag{6.10}$$

Writing the function in the standard form, we will have:

$$\max_{\epsilon,R} \quad f(\epsilon, R) = -0.25 + 0.03\epsilon - 0.058R - 0.0003\epsilon R \tag{6.11a}$$

$$\text{s.t.} \quad g(\epsilon, R) = -10\epsilon + 30R = 95.57 \tag{6.11b}$$

$$h_1(\epsilon, R) = -37.1R^2 + 270R - 490.3 + \epsilon \leq 0 \tag{6.11c}$$

$$h_2(\epsilon, R) = 40.9R^2 - 326R + 652 - \epsilon \leq 0 \tag{6.11d}$$

The Lagrangian for the KKT conditions is:

$$L(\epsilon, R, \lambda, \mu) = f(\epsilon, R) + \lambda(95.57 - g(\epsilon, R)) - \mu_1 h_1(\epsilon, R) - \mu_2 h_2(\epsilon, R) \tag{6.12}$$

Assuming (ϵ^*, R^*) to be the optimum solution, which maximize $f(\epsilon, R)$ subject to constraints $g(\epsilon, R)$, $h_1(\epsilon, R)$ and $h_2(\epsilon, R)$, then there exist $(\lambda^*, \mu_1^*, \mu_2^*)$ such that:

$$\nabla f(\epsilon^*, R^*) - \lambda^* \nabla g(\epsilon^*, R^*) - \mu_1^* \nabla h_1(\epsilon^*, R^*) - \mu_2^* \nabla h_2(\epsilon^*, R^*) = 0 \tag{6.13a}$$

$$\mu_i^* \nabla h_i(\epsilon^*, R^*) = 0 \qquad i = 1, 2 \quad \text{and} \quad \mu_i \geq 0 \tag{6.13b}$$

where the Equations 6.13a and 6.13b are the complementary equations. Constructing the Lagrangian function along with the above conditions we get:

$$\frac{\partial L}{\partial \epsilon} = 0.03 - 0.0003R + 25\lambda_1 - \mu_1 + \mu_2 = 0 \tag{6.14a}$$

$$\frac{\partial L}{\partial R} = -0.058 - 0.0003\epsilon - 150\lambda_1 + \mu_1(74.2R - 270) + \mu_2(-81.8R + 326) = 0 \tag{6.14b}$$

$$\mu_1(-37.1R^2 + 270R - 490.3 + \epsilon) = 0 \tag{6.14c}$$

$$\mu_2(40.9R^2 - 326R + 652 - \epsilon) = 0 \quad \text{for} \quad \mu_1, \mu_2 \geq 0 \tag{6.14d}$$

The above conditions are called *Kuhn-Tucker* (or *Karush-Kuhn-Tucker*) conditions. For (ϵ^*, R^*) to be optimal *some* of the inequalities must be tight among which those that are not tight will have the corresponding price $\mu_i^* = 0$. The tight constraints lead to equalities which correspond to the *Lagrangian multiplier* approach.

Now, we must partition the analysis into cases depending on the complementary conditions. Usually, to begin solving these type of problems, we can begin with complementary conditions and to do that we can assume either μ_i must be zero or $h_i(\epsilon^*, R^*) = 0$ for $i = 1, 2$. According to the various possibilities here, we consider the solution by solving the first constraint:

$$-10\epsilon + 30R = 95.5 \tag{6.15}$$

along with the complementary condition of $\mu_2 > 0$ which from Equation 6.14d results in the following:

$$40.9R^2 - 326R + 652 - \epsilon = 0 \tag{6.16}$$

Solving the last two equations, 6.15 and 6.16 we get: $(\epsilon_1^*, R_1^*) = (2.6, 4.06)$ and $(\epsilon_2^*, R_2^*) = (2.4, 3.98)$.

Now, using Equations 6.14a and 6.14b we can find μ_2 to check the optimality conditions (Note that μ_1 has been set to be zero in this case).

Using the first set of solutions $(\epsilon_1^*, R_1^*) = (2.6, 4.06)$ we get: $(\mu_1, \mu_2) = (0, 0.0086)$ which is feasible ($\mu_2 > 0$). However, solving for the second set of solution $(\epsilon_1^*, R_1^*) = (2.4, 3.98)$ we get: $(\mu_1, \mu_2) = (0, -0.0087)$, which is not feasible since $\mu_2 < 0$.

Checking other possibilities for complementary conditions along with feasibility constraints resulted in the optimal solution to be equal to $(\epsilon_1^*, R_1^*) = (2.6, 4.06)$. For example, checking for $(\mu_1, \mu_2) = (0, 0)$ resulted in $R^* < 0$ which is not accepted.

It should be stated that the problem solved here has also checked for being convex and hence the optimal solution is the global optimal. Also, the optimal solution leads to the optimal objective function of value: $\delta_r = 0.406\ \mu m$.

7.0 UNCERTAINTY TREATMENT OF SUBGRAIN SIZE MODEL FROM MACHINING USING BAYESIAN STATISTICS

It is well recognized that machining process is accompanied with various material and process uncertainties [129, 36]. To name a few, such uncertainties may be introduced due to material impurities, material property uncertainties of workpiece and cutting tool [26], machining parameters, tool geometry, tool wear, build-up edge and machining time [16]. Consequently, the model predictions of final material properties as well as the microstructure control can vary from time to time even under the same cutting conditions due to aforementioned uncertainties. These variations can be even more pronounced under worn tool cutting conditions [111] and therefore it would not be trustworthy to verify the validity of the developed model by simply comparing the experimental measurements with the model predictions or vice versa. Alternatively, a new model validation methodology needs to be explored to fully account for the possible effects of machining process uncertainties. The non-linearity of the machining process demands robust and reliable algorithms to deal with all the invisible trends presented when a workpiece is machined [35]. Hence, the expended effort in establishing the Rate-Strain-Microstructure (RSM) models can overcome this limitation if a quantitative evaluation of the uncertainties is performed [129, 36]. Traditional model building practices involve extensive Design of Experiments (DOE) and using linear or nonlinear regression, fuzzy or neural network based approaches. In this research work, we aim to apply Bayesian statistical methods to account for the existing uncertainties.

7.1 UNCERTAINTY IN ENGINEERING PROBLEMS

There are two types of uncertainties in engineering problems named aleatory uncertainty and epistemic variability. Aleatory variability refers to natural variations of a quantity, while epistemic uncertainty refers to the uncertainty resulting from lack of knowledge about underlying physics of a certain system [18, 81]. Usually, both classes exist in engineering problems. For example, the present work, definitely include epistemic uncertainties as the input-output relationship involves uncertainty about the fundamental mechanism that produces outputs. Additionally, there exist aleatory uncertainties in measurement of the output, and variation of process parameters in machining. Both variations need to be accounted through uncertainty quantification and propagation methods rooted in probability and decision theories.

7.2 BAYESIAN VS. FREQUENTIST APPROACH

There are two approaches in probability theory: Frequentist approach and Bayesian approach. Frequentist (or classical) approach, as the name says, views probability of an event as an expected frequency when event occurs for a large number of times. The Bayesian (or non-Frequentist) approach interprets probability of an event as a degree of belief, and hence is subjective. The appropriateness of Frequentist and Bayesian interpretations of probability has been long debated [17, 81]. However, for scientists and engineers, the Bayesian interpretation is more attractive.

It is notable why the Bayesian approach has been preferred and used here to address the variations in subgrain size model. The Bayesian methods provide a unifying framework for identification, control, decision making and optimization. As far as machining process modeling is concerned, there are very limited measurable variables and the measurements involve high uncertainty. The empirical models involve large number of parameters to be identified and since the experiments are time consuming and expensive, the large dimensional Design of Experiments (DOE) may be impractical.

It is recognized that the Bayesian approach methodology provides a promising alternative to the conventional models introducing opportunities to accommodate these shortcomings [44]. For example, Bayesian-based credible interval can be defined where each measurement should fall within a range defined by the significance level and credible interval [44]. Also, Bayes theorem can be used to update the user's beliefs about the microstructure outcomes given new information (new measurement result) in order to moderate the overall variations [44, 111].

7.3 BAYESIAN MODEL OF SUBGRAIN SIZE

The Bayesian approach incorporates information, preferences, and available alternatives to derive the best decision alternative. Information is described in terms of a joint probability distribution that captures the uncertainty about the possible outcomes for each alternative and uses Bayesian analysis to improve knowledge when new information is revealed. In this framework, a prior is used that captures the available information. This prior is established through incorporating all data and developed model, if existed; this makes it an attractive candidate to update information in experimental settings. The Bayesian approach can then be used in aggregating experimental results and can determine a posterior distribution based on all data or models that are collected. These three updating steps of the approach are illustrated schematically in Figure 29.

For simplicity, the subgrain size equation is approximated as a linear equation of strain and R:

$$\delta_r = A_0 + A_1\epsilon + A_2R \tag{7.1}$$

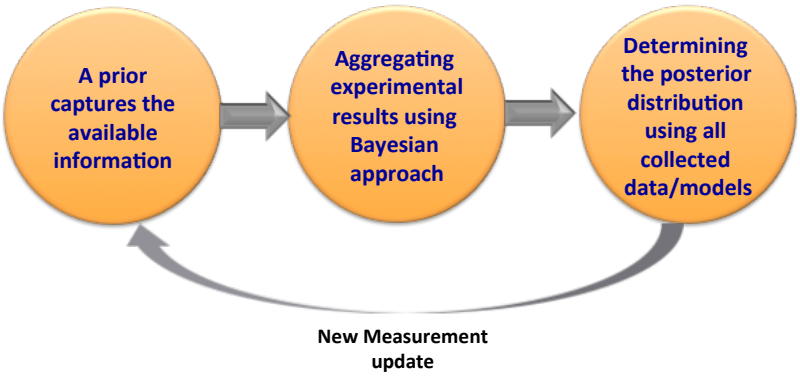

Figure 29: The updating process in Bayesian Approach.

Note that this equation of subgrain size in comparison with Equation 5.9, approximates the subgrain size measurements relatively well enough and this is due to the weak contributions of the strain and R interaction in subgrain size evolution model. Also, as A_0 can be interpreted as the initial value of subgrain size in annealed copper, it is considered here as constant during the Bayesian updating process. Doing this, the Bayes theorem is used to develop the posterior distributions of subgrain size as the following:

$$P(\delta|A_1, A_2) = \frac{P(A_1, A_2)P(A_1, A_2|\delta)}{\int\int P(A_1, A_2)P(A_1, A_2|\delta)dA_1dA_2} \tag{7.2}$$

In Equation 7.2, the terms can be identified as:

- $P(A_1, A_2)$: Prior joint distribution of the coefficients
- $P(A_1, A_2|\delta)$: Data likelihood
- $P(\delta|A_1, A_2)$:Posterior distribution of the subgrain size

In Equation 7.2, the denominator is the normalizing factor and since is not a function of the coefficients A_1 and A_2, we can write the posterior ($f_\delta(\delta|A_1, A_2)$) as being proportional to the prior (f_{A_1,A_2}) times the likelihood ($l(\delta|A_1, A_2)$):

$$f_\delta(\delta|A_1, A_2) \propto f_{A_1,A_2} l(\delta|A_1, A_2) \tag{7.3}$$

we can see from Equation 7.2 that the posterior is a conditional distribution for subgrain size given the observed data, here the coefficients of subgrain size equation. To begin, the prior distribution of the coefficients is determined using the experimental values of the subgrain size for sample conditions. Using the available experimental measurements, a Bivariate Gaussian distribution with no covariance as below is considered for which the joint probability distribution is shown in Figure 30.

$$P(A_1, A_2) \sim N\left(\begin{bmatrix} 0.025 \\ 0.055 \end{bmatrix}, \begin{bmatrix} 0.0008 & 0 \\ 0 & 0.0029 \end{bmatrix}\right)$$

It is crucial that the prior distribution parameters be as close as possible to the actual values to help with the efficiency of the convergence process. Therefore, we have opted for normal prior from the values obtained by the linear regression using the data point measurements of sample conditions as listed in Table 1.

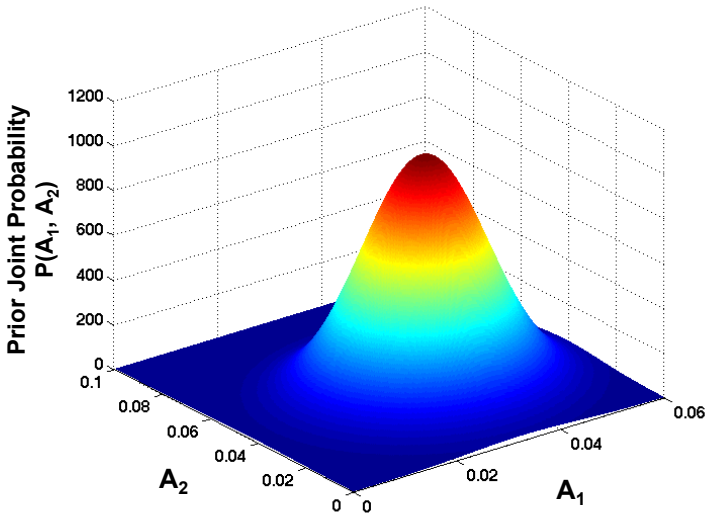

Figure 30: Prior Distribution of the coefficients.

After establishing the prior distributions, the next step is to calculate the data likelihood function required for Bayesian inference. The data likelihood is found, deploying the technique called Discrete Grid Method [111, 81]. In this method, to determine the likelihood function for a measured value of subgrain size, δ_m, first, using the values of the coefficients, a grid of 300 points is created, for which the ranges $(0.0002 - 0.06)$ for A_1 and $(0.0003 - 0.1)$ for A_2 were selected. Second, with the measured subgrain size value obtained for a new 0L condition, $\delta_m = 0.23$, all possible values of coefficients are calculated that will result in that subgrain size value. In these calculations, the measured value of subgrain size is assumed to have measurement noise equal to 2% of the measured value. This way, we get the likelihood function, which can be interpreted as "given the new measurement and the model, what is the probability that the prior distribution of the coefficients result in the new measurement data". Figure 31 demonstrate the obtained likelihood.

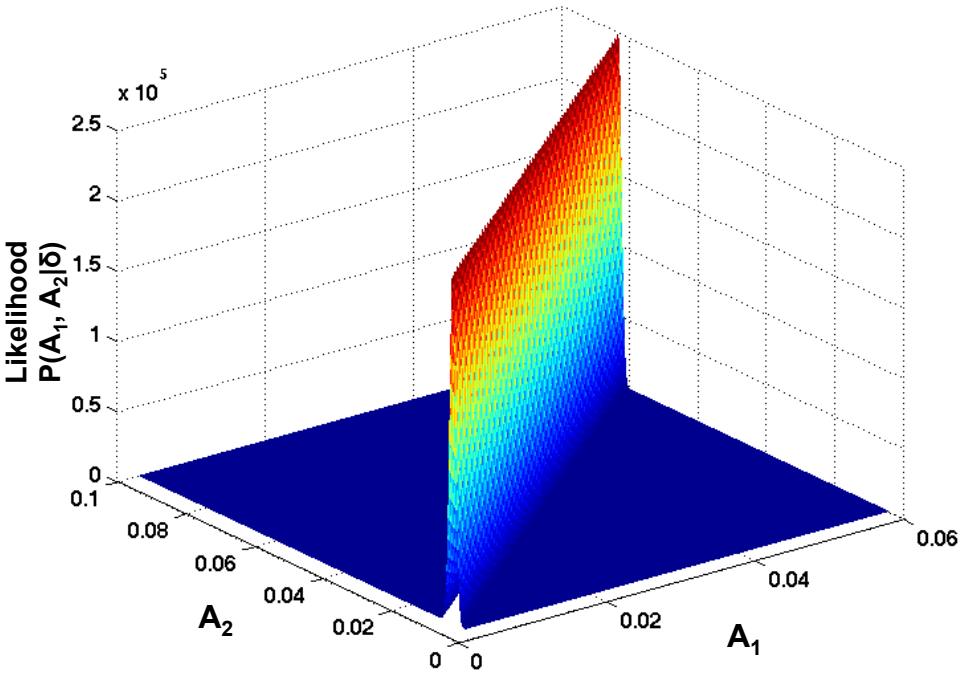

Figure 31: Data Likelihood.

After calculating the data likelihood, multiplying the prior distribution and the likelihood function (point by point), the posterior distribution is obtained. A matrix will be generated which shows the posterior distribution in Figure 32. Note that the resulting posterior distribution was normalized to obtain a unit volume under the pdf area. Sampling from the posterior is not usually possible and straightforward, and consequently, we use Markov Chain Monte Carlo (MCMC) methods to collect samples that can be used to obtain the parameters of the posterior distribution.

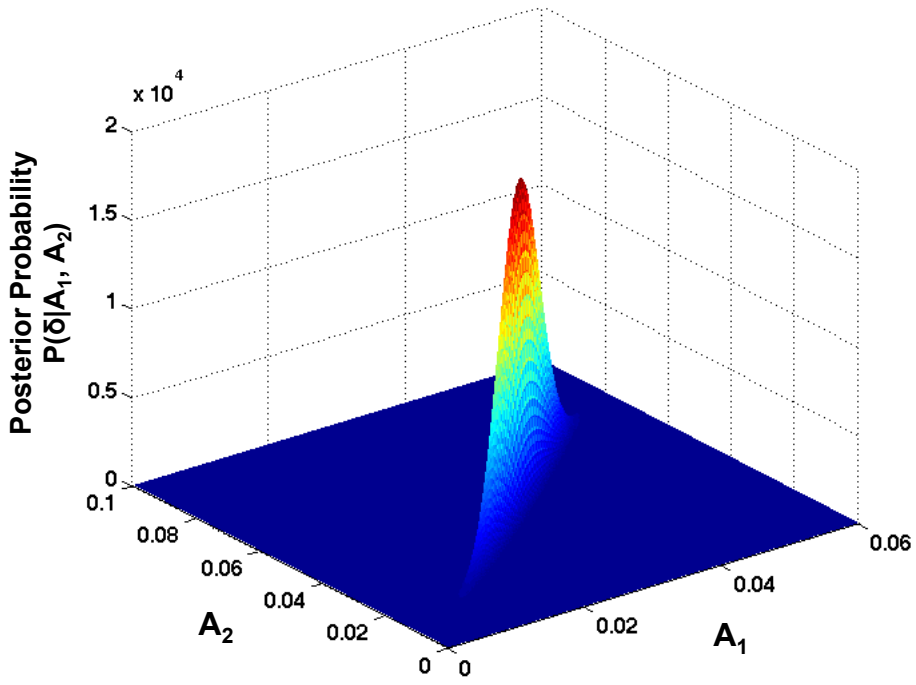

Figure 32: Posterior distribution of coefficients.

In statistics, MCMC methods consist of algorithms for sampling from a probability distribution based on constructing a Markov chain that has the desired distribution as its equilibrium distribution. This technique has extensive applications in biostatistics; image and video processing, and machine learning fields [46]. In this work, we are going to apply this method to generate sample from the posterior distribution for which there are various algorithms such as Gibbs Sampling, Metropolis algorithm and Metropolis Hastings Algorithm [46, 81].

In the present work, we apply Metropolis-Hastings algorithm in order to produce samples from the posterior distribution of regression coefficients. The Metropolis sampler, the independence sampler, and the random walk are different types of the Metropolis- Hastings method. Metropolis-Hastings algorithm obtains the state of the chain at $t+1$ by sampling a candidate point Y from a proposal distribution $p(.|X_t)$, which depends only on the previous state X_t and can have any form subject to regularity conditions [72]. It should be noted that the proposal distribution should be such that it can be easily used to generate sample from and it satisfies the necessary regularity conditions being irreducibility and aperiodicity [72]. The generated candidate point is accepted in the chain with probability given by:

$$\alpha(X_t, Y) = min\{1, \frac{\pi(Y)p(X_t|Y)}{\pi(X_t)p(Y|X_t)} \tag{7.4}$$

If the point Y is not accepted, then the next point will remain the same and $X_t+1 = X_t$. These steps are as following:

1. Starting the chain at X_0 for $t = 0$.
2. Generating a point Y from $p(.|X_t)$.
3. Generating U from a uniform $(0, 1)$ distribution.
4. If $U \leq alpha$, then $X_{t+1} = Y$, else $X_{t+1} = X_t$.
5. For $t = t + 1$ steps 2 through 5 should be repeated.

When for the proposal distribution we have $p(Y|X) = P(|X - Y|)$, the algorithm is random walk Metropolis. Since in this case, we are dealing with symmetric distribution, the probability of moving will be $P(Y)/P(Xt)$. If $P(Y) \geq P(X_t)$, then the next state of the chain will be Y because $\alpha(X_t, Y)$ equates 1, which means that a move that jumps up the trend will be always accepted. A move that goes downhill will be accepted with the probability $P(Y)/P(X_t)$.

To obtain the updated distribution of the coefficients, MCMC using random walk Metropolis is applied using the generated samples from the posterior distribution of the coefficients. Since the posterior distributions of the regression coefficients is a conjugate bivariate normal distribution, random samples were drawn from the distribution using the MATLAB command "mvnrnd". One input to this function is the covariance matrix. This matrix was identified using the MATLAB command "cov" based on the A_1 and A_2 values. 3000 random samples were obtained from the posterior distributions.

Plots of sequences of the coefficients are shown in Figure 33. On these figures, the vertical lines, represent the "burn-in" time that has been considered for convergence estimation. Figure 32 shows the posterior distribution of the coefficients. We have repeated this process for four updates of subgrain size measurement and in Figure 34, the distributions are compared for the first, second, third, and forth update. Note that the uncertainty (standard deviation) decreases with additional data. This indicates the improvement in knowledge with available information which is due to the fact that the variance of the coefficients is decreased and the distribution is sharper after the each update.

The results of the four updates using the four measurements are summarized in Table 6 for the coefficients of subgrain size model and Table 7 where the sample conditions and the subgrain sizes are compared for measurements, prior, and the posterior values. As shown, in these Tables, the decreasing trend of variation in coefficients and hence in posterior of subgrain size values are in good agreement with Figure 34.

This work is expected to complement the accomplished work in previous chapters and the premise of the ongoing research is to capture the evolution of the complex interactions

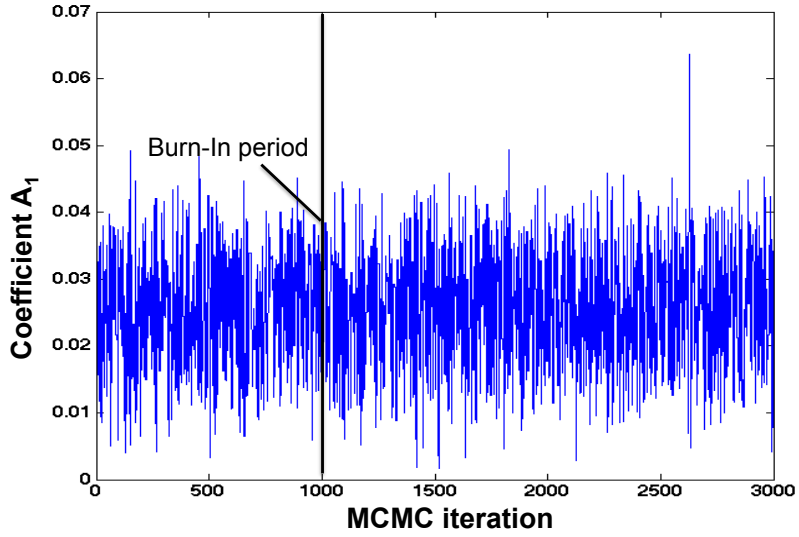

(a)

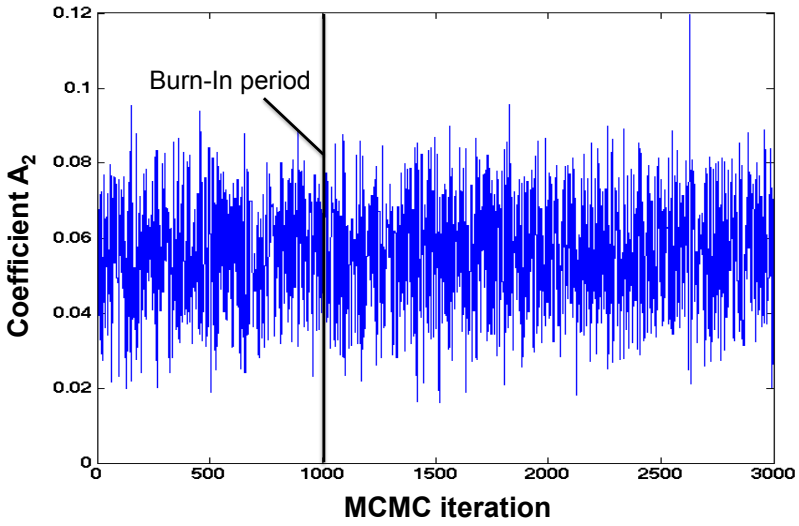

(b)

Figure 33: Markov Chain Monte Carlo simulations results a) A_1, b) A_2.

between the existing uncertainties and the distribution of bulk microstructure leading to other surface microstructure as well. Identifying this evolution will probably link the effect of unknown variations to the modification of thermomechanical conditions of SPD during chip formation, and its effect via the Rate-Strain-Microstructure (RSM) maps on the resulting microstructure. As a result, Bayesian inference, through a rigorous mathematical treatment of uncertainty, is envisaged to propose a powerful and flexible tool in this study. Also, this step will be an important advance towards achieving optimal machining conditions providing substantial economic benefits to the industry and enhance the competitiveness of the manufacturing sector.

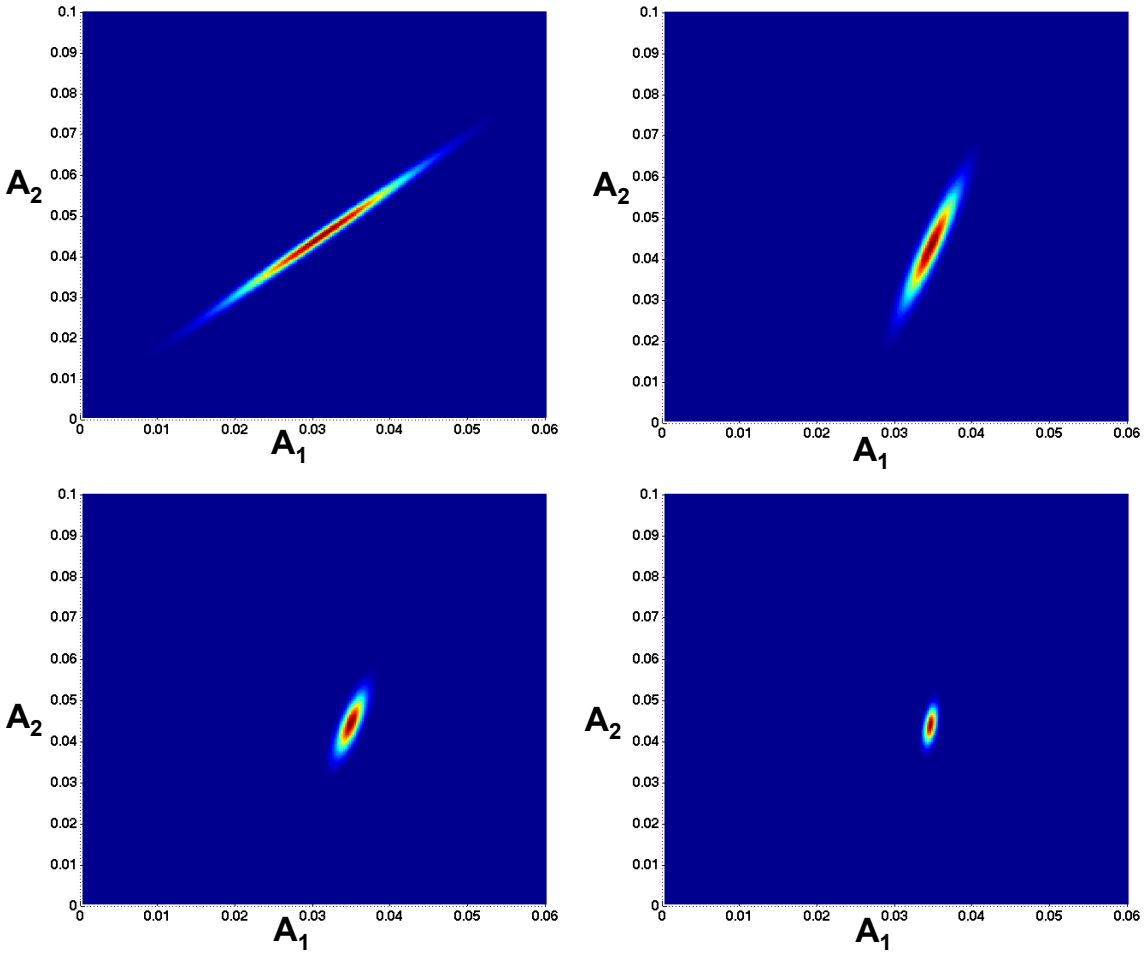

Figure 34: Posterior joint distributions of the coefficients for subgrain size model after the first update (top left), second update (top right), third update (bottom left), and fourth update (bottom right).

Table 6: Results of MCMC simulation for coefficients of subgrain size model (Equation 7.1).

Update #	A_1	A_2
1	0.025 ± 0.00071	0.055 ± 0.0023
2	0.026 ± 0.00029	0.056 ± 0.0008
3	0.027 ± 0.00005	0.057 ± 0.00015
4	0.028 ± 0.00006	0.058 ± 0.00017

Table 7: Summary of the subgrain size for four updates. In each update, the prior and posterior of subgrain size $\pm$ the standard deviation is calculated using the results of MCMC simulation in Table 6.

#	ϵ	R	Subgrain Size (δ)		
			Measured δ_m (μm)	Prior (μm)	Posterior (μm)
1	8.6	4.14	0.23	0.26 ± 0.00471	0.26 ± 0.00350
2	2.6	3.95	0.41	0.40 ± 0.00726	0.40 ± 0.00240
3	5.9	4.07	0.30	0.33 ± 0.00154	0.32 ± 0.00030
4	3.9	4.15	0.36	0.38 ± 0.00041	0.38 ± 0.00047

8.0 CONCLUSIONS AND FUTURE WORK

Large Strain Machining (LSM) was utilized as a test of microstructure response in Cu under deformation conditions characterized by strains, $\epsilon \sim (1-10)$, strain-rates, $\dot{\epsilon} \sim (10-10^3\ /s)$ and thermomechanically-coupled temperatures ranging from ambient to $\sim 470\ K$. Since, the deformation zone in LSM is not occluded, an *in situ* characterization of the deformation field was performed using high-speed digital image correlation and infrared thermography. The resulting "chip" material, as an alternative solution to study the severely deformed machined surface was examined via Orientation Imaging Microscopy (OIM) using Electron Back-Scattered Diffraction (EBSD) in a Scanning Electron Microscope (SEM).

A preliminary first model in section 5.1 presents a framework for microstructure control in SPD by orthogonal machining that maps resulting nanostructural characteristics such as grain size distribution and misorientation distribution to unique regions of a suitably defined phase-space. A strain-ln(Z) space, as in Figure 11 is proposed as a candidate space for developing these interconnections to ultimately encapsulate the relationships within a Rate-Strain-Microstructure (RSM) map. The map captures the relevant process-microstructure relationships under strain, strain-rate and temperature conditions that are relevant to the orthogonal machining process. Particular focus is devoted to quantitative microstructural

characteristics including, average grain size and average fraction of LAGBs. These microstructural characteristics offer direct means to predict an array of performance attributes because a) average grain size from SPD essentially controls the flow strength of the resulting material via the usual Hall-Petch relationship [118, 117] and b) Grain Boundary (GB) characteristics are encapsulated by the LAGB fraction can be used to determine properties like effective diffusion, mobility and grain growth behaviours. The map can also be used to determine whether the resulting microstructure will be unimodal or multimodal and potentially estimate the ductility of the components.

In an alternative yet physical-base model, in section 5.2, analogous parametrizations is developed (Figure 13), on which the evolution of the subgrain size under similar conditions is captured from two parameters: the strain and the parameter "R" that is a function of the strain-rate, temperature and material constants. The idea behind the focus on the subgrain size was our expectation of this as a microstructural variable that is at the nexus of other microstructural characteristics. For example, the subgrain size is often found to co-vary with the dislocation density in consonance with expectations of similitude [117, 94]. Also, it is anticipated that similar parametrizations can be accomplished for other microstructural characteristics, including that for dislocation densities to delineate two orthogonal axes, from a mechanism-based analysis akin to that shown here for subgrain size model. Consequently, in section 5.4, we anticipated the "athermal" y axis to still be the effective strain, although the parametrization for x axis for dislocation densities being a function of the parameter R according to the similitude relationship, relating the dislocation densities to the average subgrain size. Figure 27 depicts the evolution of dislocation densities which is in good agreement with the experimental values overlaid on the contour map. Calculating the dislocation densities within the cells, the results of similitude are shown in Figure 28 which confirms well with the range ($\sim 5 - 10$) reported in Ref [94].

Furthermore, the onset of Geometric Dynamic Recrystallization (GDRX) is closely tied-in with the evolution of the subgrain size [107] and here, we utilized our earlier model for subgrain size to evolve a model for identifying the criterion for the dynamic recrystallization mechanism. An examination of the Grain Orientation Spread (GOS) revealed a continuum of microstructures across the deformation conditions examined here, with the exception of a

sample that involved a deformation temperature of $\sim 485\ K$. This outlier sample was characterized by rampant recrystallization, a fully-coarsened micro-scale grain structure and a low hardness value that indicated a completion of Discontinuous Dynamic Recrystallization (DDRX) and a complete loss of ultrafine grains. Nonetheless, this sample provides a threshold of the GOS that characterizes a nearly dislocation-free, recrystallized structure, which was then used to segregate the microstructures and to calculate the fraction of recrystallized grains in the other deformation conditions. As expected, we found a correlation between the area fraction of the recrystallized portions of the microstructure and the deformation strains for all samples created at temperatures $< 485\ K$. Furthermore, for these samples a correlation is found between the fraction of recrystallization and the fraction of high angle boundaries. Noting the gradual evolution of microstructures across these samples, we hypothesized the role of Geometric Dynamic Recrystallization (GDRX) as a mechanism that determines the formation of the recrystallized fractions. At $485\ K$ however, the sufficient mobilities likely allowed for the discontinuous dynamic recrystallization via the migration of the grain boundaries. Consequently, a model is proposed for the onset of GDRX using a model for subgrain sizes for these deformation conditions that is shown to be in reasonable agreement with earlier models for GDRX that utilize a Zener-Hollomon parameter-based approach. By mapping the onset and progression of dynamic recrystallization on a map-space parameterized as a function of the thermomechanics of severe shear, this approach may help design and control microstructures resulting from shear-based metal cutting and surface generation processes that are the mainstay of the manufacture of metallic components, including in milling, drilling, turning, shaping, etc.

RSM map also delineates regions where recrystallization will occur and was used to determine conditions to produce relatively coarse grained, low strength microstructure albeit thermally stable, and hence can be employed for high temperature applications. In section 6.2, the thermomechanical conditions of the optimum sample with aforementioned attributes was developed. Together, the overarching vision of the development of such maps envisages a process design tool for creating customizable fine grained materials and surfaces using SPD processes such as orthogonal machining to enable the design of enhanced multifunctional materials and products.

Such analysis can enable process design tools by relating microstructural characteristics to subregions of a parameterized RSM space. This can be useful for controlling deformed microstructures in an array of severe shear-based manufacturing processes, including the ubiquitous machining processes that bequeath a severely shear-deformed surface on manufactured components. As we had pointed out earlier, the deformation zone that produces the chip also bequeaths a severely deformed surface microstructure to the machined surface. Controlling the microstructure on machined surfaces to achieve tunable levels of refinements may be useful considering recent demonstrations of modification of surface phenomena as a function of the underlying grain size. These include the observation of enhanced proliferation of osteoblasts at surfaces of nanostructured metals [98] and the modification of corrosion properties in the grain refined states [87]. To achieve such enhanced functionalities inherited from the fine-grained state, RSM mappings developed in this work can be utilized to identify the thermomechanical parameters of SPD to endow the desired microstructural characteristics using processes, including machining. Accomplishment of such broader aims however, would require a recursive enhancement of the fidelity of the mappings through the accumulation of more empirical data. This is also necessary for analyzing the coefficients of the microstructure response equations to offer a better understanding of the interplay of phenomena leading to microstructure refinement under such SPD conditions.

Finally, to account for the underlying uncertainties in machining Bayesian approach has been applied to the subgrain size model based on the application of decision theory to manufacturing models. The beliefs about the distributions of the coefficients of subgrain size evolution was updated using measured values of the subgrain size through three steps. First, the prior distribution (initial belief) is established. Then, the likelihood was determined using the Discrete Grid Method, where the range of values for the variables of interest (coefficients of subgrain size model) is divided into a grid of points. Using the new measured value of the subgrain size, all possible values of the coefficients were calculated considering bivariate normal distribution of coefficients. The value of the distribution at the measured value was taken to be the likelihood, which gives the probability that the selected variable values would produce the measured value taking into account the considered uncertainty. The posterior distribution was calculated by multiplying the prior and likelihood functions and this process

was repeated for multiple test measurements to obtain a final posterior distribution for the coefficients. The process is shown to have decreased variability in the distribution of the coefficients and hence in the estimation of the subgrain size value as illustrated in Figure 34 for four updates.

The presented research work can be extended with the aim of making this study more practically applicable towards which, the following directions are proposed:

1. Towards better uncertainty treatment in LSM:

   The Bayesian framework discussed in the work is unifying framework for model identification, control, and decision support. The decision support problem of identifying the subgrain size response was demonstrated using Naive Bayes Classifier. However, the developed model can be progressed considering the hierarchical Bayesian approach where the effect of tool rake angle and cutting velocity would establish the basis for the thermomechanical conditions, strain, strain-rate, and temperature leading to the final microstructure results in a probabilistic framework.

2. Towards the uncertainty treatment for other microstructure responses:

   Progressing with the improvements in implementation of the Bayesian statistic, the aim is to account for the existing uncertainties for other RSM mappings: grain size, LAGB fraction, recrystallization fraction, and dislocation density as well. Also, it would be trustworthy to study the possible interactions among these microstructural attributes and their effects on the microstructure evolution in a recursive statistical framework.

3. Towards accounting for the effect of tool wear on the microstructure evolution from LSM:

   Tool wear is of foremost importance in metal cutting techniques. Owing to its direct impact on the final microstructure, tool wear effect must be accounted in the RSM mappings. The premise of the ongoing research with regard to the effect of tool wear is that machining under realistic conditions is characterized by a stochastic system wherein the temporal evolution of the tool-tip geometry and the distributions of the bulk microstructure would interact in complex ways, while leading to the evolution of surface microstructures. Identifying this evolution would still involve a Bayesian framework to link the effect

of tool-wear to the modification of thermomechanical conditions of severe plastic deformation during chip formation, and its effect via the Rate-Strain-Microstructure maps on the resulting microstructure.

BIBLIOGRAPHY

[1] American association of orthopaedic surgeons. www.aaos.org.

[2] S. Abolghasem, S. Basu, and M.R. Shankar. Quantifying the progression of dynamic recrystallization in severe shear deformation at high strain rates. *Journal of Materials Research*, 28(15):2056–2069, 2013.

[3] S. Abolghasem, S. Basu, S. Shekhar, J. Cai, and M.R. Shankar. Mapping subgrain sizes resulting from severe simple shear deformation. *Acta Materialia*, 60(1):376–386, 2012.

[4] H. Abrams. Grain size measurement by the intercept method. *Metallography*, 4(1):59–78, 1971.

[5] A.H. Adibi Sedeh, V. Madhavan, and B. Bahr. Extension of oxleys analysis of machining to use different material models. *Journal of manufacturing science and engineering*, 125(4):656–666, 2003.

[6] H. Ahlborn, E. Hornbogen, and U. Köster. Recrystallisation mechanism and annealing texture in aluminium-copper alloys. *Journal of Materials Science*, 4(11):944–950, 1969.

[7] G.H. Akbari, C.M. Sellars, and J.A. Whiteman. Microstructural development during warm rolling of an if steel. *Acta materialia*, 45(12):5047–5058, 1997.

[8] S. Akcan, W.I.S. Shah, S.P. Moylan, S. Chandrasekar, P.N. Chhabra, and H.T.Y. Yang. Formation of white layers in steels by machining and their characteristics. *Metallurgical and Materials Transactions A*, 33(4):1245–1254, 2002.

[9] M.H. Alvi. *Recrystallization Kinetics and Microstructural Evolution in Hot Rolled Aluminum Alloys*. PhD thesis, Carnegie Mellon University, 2005.

[10] M.H. Alvi, S.W. Cheong, H. Weiland, and A.D. Rollett. Recrystallization and texture development in hot rolled 1050 aluminum. In *Materials Science Forum*, volume 467, pages 357–362. Trans Tech Publ, 2004.

[11] Y. Amouyal, S.V. Divinski, L. Klinger, and E. Rabkin. Grain boundary diffusion and recrystallization in ultrafine grain copper produced by equal channel angular pressing. *Acta Materialia*, 56(19):5500–5513, 2008.

[12] U. Andrade, M.A. Meyers, K.S. Vecchio, and A.H. Chokshi. Dynamic recrystallization in high-strain, high-strain-rate plastic deformation of copper. *Acta metallurgica et materialia*, 42(9):3183–3195, 1994.

[13] K. Anselme. Osteoblast adhesion on biomaterials. *Biomaterials*, 21(7):667–681, 2000.

[14] W.J. Arbegast, Z. Jin, A. Beaudoin, T.A. Bieler, and B. Radhakrishnan. Hot deformation of aluminum alloys iii. *TMS, Warrendale, PA*, pages 313–327, 2003.

[15] J.E. Bailey and P.B. Hirsch. The dislocation distribution, flow stress, and stored energy in cold-worked polycrystalline silver. *Philosophical Magazine*, 5(53):485–497, 1960.

[16] D. Bajić and A. Belaić. Mathematical modeling of surface roughness in milling process. In *Proceedings of the 1st International Scientific Conference on Production Engineering (ISC), Lumbarda, Croatia*, pages 109–115, 2006.

[17] M.J. Bayarri and J.O. Berger. The interplay of bayesian and frequentist analysis. *Statistical Science*, pages 58–80, 2004.

[18] M.A. Bilal and G.J. Klir. *Uncertainty modeling and analysis in engineering and the sciences*. CRC Press, 2006.

[19] W. Blum. High-temperature deformation and creep of crystalline solids. *Materials science and technology*, 1993.

[20] B. Bokstein, V. Ivanov, O. Oreshina, A. Peteline, and S. Peteline. Direct experimental observation of accelerated zn diffusion along triple junctions in al. *Materials Science and Engineering: A*, 302(1):151–153, 2001.

[21] A. Borbély and J.H. Driver. Dislocation density measurements by x-ray profile analysis in texture components of deformed metals. *Archives of Metallurgy and Materials*, 50(1):65–76, 2005.

[22] A. Borbely and I. Groma. Variance method for the evaluation of particle size and dislocation density from x-ray bragg peaks. *Applied Physics Letters*, 79(12):1772–1774, 2001.

[23] L.M. Brown and W.M. Stobbs. The work-hardening of copper-silica. *Philosophical Magazine*, 23(185):1201–1233, 1971.

[24] G. Buffa, J. Hua, R. Shivpuri, and L. Fratini. A continuum based fem model for friction stir weldingmodel development. *Materials Science and Engineering: A*, 419(1):389–396, 2006.

[25] G. Buffa, J. Hua, R. Shivpuri, and L. Fratini. Design of the friction stir welding tool using the continuum based fem model. *Materials Science and Engineering: A*, 419(1):381–388, 2006.

[26] TH. Buranathiti, J. Cao, W. Chen, L. Baghdasaryan, and Z.C. Xia. Approaches for model validation: methodology and illustration on a sheet metal flanging process. *Journal of Manufacturing Science and Engineering*, 128(2):588–597, 2006.

[27] R.W. Cahn and P. Haasen. Physical metallurgy, part ii. *Elsevier Science Publishers*, 3:987–990, 1983.

[28] J. Cai, S. Shekhar, J. Wang, and M.R. Shankar. Nanotwinned microstructures from low stacking fault energy brass by high-rate severe plastic deformation. *Scripta Materialia*, 60(8):599–602, 2009.

[29] R. Calistes, S. Swaminathan, T.G. Murthy, C. Huang, C. Saldana, M.R. Shankar, and S. Chandrasekar. Controlling gradation of surface strains and nanostructuring by large-strain machining. *Scripta Materialia*, 60(1):17–20, 2009.

[30] C.E. Campbell, L.A. Bendersky, W.J. Boettinger, and R. Ivester. Microstructural characterization of al-7075-t651 chips and work pieces produced by high-speed machining. *Materials Science and Engineering: A*, 430(1):15–26, 2006.

[31] E.K. Cerreta, I.J. Frank, G.T. Gray, C.P. Trujillo, D.A. Korzekwa, and L.M. Dougherty. The influence of microstructure on the mechanical response of copper in shear. *Materials Science and Engineering: A*, 501(1):207–219, 2009.

[32] E. Cerri, E. Evangelista, A. Forcellese, and H.J. McQueen. Comparative hot workability of 7012 and 7075 alloys after different pretreatments. *Materials Science and Engineering: A*, 197(2):181–198, 1995.

[33] S.W. Cheong and H. Weiland. Understanding a microstructure using gos (grain orientation spread) and its application to recrystallization study of hot deformed al-cu-mg alloys. In *Materials Science Forum*, volume 558, pages 153–158. Trans Tech Publ, 2007.

[34] T. Childs. *Metal machining: theory and applications*. Butterworth-Heinemann, 2000.

[35] M. Correa, C. Bielza, M.J. Ramirez, and J.R. Alique. A bayesian network model for surface roughness prediction in the machining process. *International Journal of Systems Science*, 39(12):1181–1192, 2008.

[36] Bureau International des Poids et Mesures, Commission électrotechnique internationale, and Organisation internationale de normalisation. *Guide to the Expression of Uncertainty in Measurement*. International Organization for Standardization, 1995.

[37] O. Engler and M.Y. Huh. Evolution of the cube texture in high purity aluminum capacitor foils by continuous recrystallization and subsequent grain growth. *Materials Science and Engineering: A*, 271(1):371–381, 1999.

[38] Y. Estrin, E.P. Ivanova, A. Michalska, V.K. Truong, R. Lapovok, and R. Boyd. Accelerated stem cell attachment to ultrafine grained titanium. *Acta biomaterialia*, 7(2):900–906, 2011.

[39] Y. Estrin, C. Kasper, S. Diederichs, and R. Lapovok. Accelerated growth of pre-osteoblastic cells on ultrafine grained titanium. *Journal of Biomedical Materials Research Part A*, 90(4):1239–1242, 2009.

[40] SH. Faghihi, F. Azari, A.P. Zhilyaev, J.A. Szpunar, H. Vali, and M. Tabrizian. Cellular and molecular interactions between mc3t3-e1 pre-osteoblasts and nanostructured titanium produced by high-pressure torsion. *Biomaterials*, 28(27):3887–3895, 2007.

[41] P.S. Follansbee and U.F. Kocks. A constitutive description of the deformation of copper based on the use of the mechanical threshold stress as an internal state variable. *Acta Metallurgica*, 36(1):81–93, 1988.

[42] R.W. Fonda and J.F. Bingert. Precipitation and grain refinement in a 2195 al friction stir weld. *Metallurgical and materials Transactions A*, 37(12):3593–3604, 2006.

[43] H. Gao and Y. Huang. Geometrically necessary dislocation and size-dependent plasticity. *Scripta Materialia*, 48(2):113–118, 2003.

[44] A. Gelman, J.B. Carlin, H.S. Stern, and D.B. Rubin. *Bayesian data analysis*, volume 2. Taylor & Francis, 2014.

[45] PH. Gerber, J. Tarasiuk, TH. Chauveau, and B. Bacroix. A quantitative analysis of the evolution of texture and stored energy during annealing of cold rolled copper. *Acta materialia*, 51(20):6359–6371, 2003.

[46] W.R. Gilks, S. Richardson, and D.J. Spiegelhalter. *Introducing markov chain monte carlo*. London: Chapman and Hall, 1996.

[47] G. Gottstein. *Physikalische grundlagen der materialkunde*. Springer-Verlag, 2007.

[48] G. Gottstein, A.H. King, and L.S. Shvindlerman. The effect of triple-junction drag on grain growth. *Acta materialia*, 48(2):397–403, 2000.

[49] G. Gottstein, D. Zabardjadi, and H. Mecking. Dynamic recrystallization in tension-deformed copper single crystals. *Metal Science*, 13(3-4):223–227, 1979.

[50] R.K. Gupta, R.K.S. Raman, and C.C. Koch. Fabrication and oxidation resistance of nanocrystalline fe10cr alloy. *Journal of materials science*, 45(17):4884–4888, 2010.

[51] E.O. Hall. The deformation and ageing of mild steel: Iii discussion of results. *Proceedings of the Physical Society. Section B*, 64(9):747, 1951.

[52] B.O. Han, E.J. Lavernia, Z. Lee, S. Nutt, and D. Witkin. Deformation behavior of bimodal nanostructured 5083 al alloys. *Metallurgical and Materials Transactions A*, 36(4):957–965, 2005.

[53] N. Hansen, D.J. Jensen, Y.L. Liu, and B. Ralph. Microstructural and crystallographic aspects of recrystallization. Technical report, Risoe National Lab., Roskilde (Denmark). Materials Dept, 1995.

[54] J. Harding. The effect of high strain rate on material properties. *Materials at high strain rates*, pages 133–186, 1987.

[55] H.J. Höfler, R.S. Averback, H. Hahn, and H. Gleiter. Diffusion of bismuth and gold in nanocrystalline copper. *Journal of applied physics*, 74(6):3832–3839, 1993.

[56] Y. Huang and F.J. Humphreys. Measurements of grain boundary mobility during recrystallization of a single-phase aluminium alloy. *Acta Materialia*, 47(7):2259–2268, 1999.

[57] D.A. Hughes and N. Hansen. Microstructure and strength of nickel at large strains. *Acta Materialia*, 48(11):2985–3004, 2000.

[58] F.J. Humphreys. Review grain and subgrain characterisation by electron backscatter diffraction. *Journal of materials science*, 36(16):3833–3854, 2001.

[59] P. Iglesias, M.D. Bermudez, W. Moscoso, B.C. Rao, M.R. Shankar, and S. Chandrasekar. Friction and wear of nanostructured metals created by large strain extrusion machining. *Wear*, 263(1):636–642, 2007.

[60] K.V. Jata and S.L. Semiatin. Continuous dynamic recrystallization during friction stir welding of high strength aluminum alloys. *Scripta materialia*, 43(8):743–749, 2000.

[61] H. Jazaeri and F.J. Humphreys. Quantifying recrystallization by electron backscatter diffraction. *Journal of microscopy*, 213(3):241–246, 2004.

[62] H. Jazaeri and J.F. Humphreys. The effect of initial grain size on transition from discontinuous to continuous recrystallization in a highly cold rolled al-fe-mn alloy. In *Materials Science Forum*, volume 396, pages 551–556. Trans Tech Publ, 2002.

[63] S. Jeelani and M.A. Scott. How surface damage removal affects fatigue life. *International Journal of Fatigue*, 10(4):257–260, 1988.

[64] G.R. Johnson and W.H. Cook. A constitutive model and data for metals subjected to large strains, high strain rates and high temperatures. In *Proceedings of the 7th International Symposium on Ballistics*, volume 21, pages 541–547. The Netherlands, 1983.

[65] J.J. Jonas, C.M. Sellars, and W.J.M. Tegart. Strength and structure under hot-working conditions. *Metallurgical Reviews*, 14(1):1–24, 1969.

[66] F.W. Jones. The measurement of particle size by the x-ray method. In *Proceedings of the Royal Society of London A: Mathematical, Physical and Engineering Sciences*, volume 166, pages 16–43. The Royal Society, 1938.

[67] M. Kawasaki, B. Ahn, and T.G. Langdon. Microstructural evolution in a two-phase alloy processed by high-pressure torsion. *Acta Materialia*, 58(3):919–930, 2010.

[68] U.F. Kocks and H. Mecking. Physics and phenomenology of strain hardening: the fcc case. *Progress in materials science*, 48(3):171–273, 2003.

[69] D. Kuhlmann-Wilsdorf. A critical test on theories of work-hardening for the case of drawn iron wire. *Metallurgical Transactions*, 1(11):3173–3179, 1970.

[70] D. Kuhlmann-Wilsdorf and A.W. Thompson. Work hardening in tension and fatigue. *AIME, New York*, pages 1–43, 1977.

[71] A. Kuper, H. Letaw Jr, L. Slifkin, E. Sonder, and C.T. Tomizuka. Self-diffusion in copper. *Physical Review*, 96(5):1224, 1954.

[72] T.L. Lai. *Introduction to Hastings Monte Carlo Sampling Methods Using Markov Chains and Their Applications*. Springer, 1997.

[73] R. Lapovok, P.W.J. McKenzie, P.F. Thomson, and S.L. Semiatin. Processing and properties of ultrafine-grain aluminum alloy 5005 sheet. *Journal of materials science*, 42(5):1649–1659, 2007.

[74] Y.S. Li, Y. Zhang, N.R. Tao, and K. Lu. Effect of the zener–hollomon parameter on the microstructures and mechanical properties of cu subjected to plastic deformation. *Acta Materialia*, 57(3):761–772, 2009.

[75] C.V.S. Lim. *Length Scale Effect on the Microstructural Evolution of Cu layers in a Roll-bonded CuNb Composite*. PhD thesis, Carnegie Mellon University, 2008.

[76] U.S. Lindholm, A. Nagy, G.R. Johnson, and J.M. Hoegfeldt. Large strain, high strain rate testing of copper. *Journal of engineering materials and technology*, 102(4):376–381, 1980.

[77] Z.Y. Ma and S.C. Tjong. High temperature creep behavior of in-situ tib 2 particulate reinforced copper-based composite. *Materials Science and Engineering: A*, 284(1):70–76, 2000.

[78] H.J. McQueen. Materials technology-an inter-american approach. *ASME NY*, pages 379–388, 1968.

[79] H.J. McQueen and S. Bergerson. Dynamic recrystallization of copper during hot torsion. *Metal Science*, 6(1):25–29, 1972.

[80] H.J. McQueen, S. Yue, N.D. Ryan, and E. Fry. Hot working characteristics of steels in austenitic state. *Journal of Materials Processing Technology*, 53(1):293–310, 1995.

[81] P. Mehta. *Model Based Control of MAchining Processes: Exploration of Bayesian Statistical Methods for Identification and Control*. PhD thesis, Clemson University, 2013.

[82] M.A. Meyers. *Dynamic behavior of materials*. John Wiley & Sons, 1994.

[83] A. Mishra, B.K. Kad, F. Gregori, and M.A. Meyers. Microstructural evolution in copper subjected to severe plastic deformation: Experiments and analysis. *Acta Materialia*, 55(1):13–28, 2007.

[84] A. Mishra, V. Richard, F. Gregori, R.J. Asaro, and M.A. Meyers. Microstructural evolution in copper processed by severe plastic deformation. *Materials Science and Engineering: A*, 410:290–298, 2005.

[85] R. Mishra and R. Balasubramaniam. Effect of nanocrystalline grain size on the electrochemical and corrosion behavior of nickel. *Corrosion Science*, 46(12):3019–3029, 2004.

[86] R.D.K. Misra, W.W. Thein-Han, T.C. Pesacreta, K.H. Hasenstein, M.C. Somani, and L.P. Karjalainen. Cellular response of preosteoblasts to nanograined/ultrafine-grained structures. *Acta biomaterialia*, 5(5):1455–1467, 2009.

[87] R.D.K. Misra, W.W. Thein-Han, T.C. Pesacreta, K.H. Hasenstein, M.C. Somani, and L.P. Karjalainen. Favorable modulation of pre-osteoblast response to nanograined/ultrafine-grained structures in austenitic stainless steel. *Advanced Materials*, 21(12):1280–1285, 2009.

[88] S. Mitsche, P. Poelt, and C. Sommitsch. Recrystallization behaviour of the nickel-based alloy 80 a during hot forming. *Journal of microscopy*, 227(3):267–274, 2007.

[89] S. Mitsche, P. Pölt, C. Sommitsch, and M. Walter. Quantification of the recrystallized fraction in a nickel-base-alloy from ebsd-data. *Microscopy and microanalysis*, 9(S03):344–345, 2003.

[90] X. Molodova, G. Gottstein, M. Winning, and R.J. Hellmig. Thermal stability of ecap processed pure copper. *Materials Science and Engineering: A*, 460:204–213, 2007.

[91] F. Montheillet and L.J. Coze. Influence of purity on the dynamic recrystallization of metals and alloys. *physica status solidi (a)*, 189(1):51–58, 2002.

[92] R. M'Saoubi and L. Ryde. Application of the ebsd technique for the characterisation of deformation zones in metal cutting. *Materials Science and Engineering: A*, 405(1):339–349, 2005.

[93] T. Nairong, T. Weiping, W. Zhenbo, W. Wei, S. Manling, L. Jian, and L. Ke. Mechanical and wear properties of nanostructured surface layer in iron induced by surface mechanical attrition treatment. *Journal of Materials Science and Technology*, 19(6), 2003.

[94] E. Nes. Modelling of work hardening and stress saturation in fcc metals. *Progress in Materials Science*, 41(3):129–193, 1997.

[95] E. Nes, K. Marthinsen, and Y. Brechet. On the mechanisms of dynamic recovery. *Scripta Materialia*, 47(9):607–611, 2002.

[96] E. Nes, T. Pettersen, and K. Marthinsen. On the mechanisms of work hardening and flow-stress saturation. *Scripta materialia*, 43(1):55–62, 2000.

[97] F.L. Nie, Y.F. Zheng, Y. Cheng, S.C. Wei, and R.Z. Valiev. In vitro corrosion and cytotoxicity on microcrystalline, nanocrystalline and amorphous niti alloy fabricated by high pressure torsion. *Materials Letters*, 64(8):983–986, 2010.

[98] C. op't Hoog, N. Birbilis, and Y. Estrin. Corrosion of pure mg as a function of grain size and processing route. *Advanced Engineering Materials*, 10(6):579–582, 2008.

[99] Ch.H. Park, Ch.S. Lee, Y.J. Kim, J.H. Jang, J.Y. Suh, and J.W. Park. Improved pre-osteoblast response and mechanical compatibility of ultrafine-grained ti–13nb–13zr alloy. *Clinical oral implants research*, 22(7):735–742, 2011.

[100] J.W. Park, Y.J. Kim, Ch.H. Park, D.H. Lee, Y.G. Ko, J.H. Jang, and Ch.S. Lee. Enhanced osteoblast response to an equal channel angular pressing-processed pure titanium substrate with microrough surface topography. *Acta biomaterialia*, 5(8):3272–3280, 2009.

[101] W.J. Parker, R.J. Jenkins, C.P. Butler, and G.L. Abbott. Flash method of determining thermal diffusivity, heat capacity, and thermal conductivity. *Journal of applied physics*, 32(9):1679–1684, 1961.

[102] N.J. Petch. The cleavage strength of polycrystals. *J. Iron Steel Inst.*, 174:25–28, 1953.

[103] P. Poelt, C. Sommitsch, S. Mitsche, and M. Walter. Dynamic recrystallization of ni-base alloysexperimental results and comparisons with simulations. *Materials Science and Engineering: A*, 420(1):306–314, 2006.

[104] R.K.S. Raman and R.K. Gupta. Oxidation resistance of nanocrystalline vis-à-vis microcrystalline fe–cr alloys. *Corrosion science*, 51(2):316–321, 2009.

[105] V. Randle and O. Engler. *Introduction to texture analysis: macrotexture, microtexture and orientation mapping*. CRC Press, 2000.

[106] Th. Roland, D. Retraint, K. Lu, and J. Lu. Fatigue life improvement through surface nanostructuring of stainless steel by means of surface mechanical attrition treatment. *Scripta Materialia*, 54(11):1949–1954, 2006.

[107] A. Rollett, F.J. Humphreys, G.S. Rohrer, and M. Hatherly. *Recrystallization and related annealing phenomena*. Elsevier, 2004.

[108] J.P. Sah, G.J. Richardson, and C.M. Sellars. Recrystallization during hot deformation of nickel. *Journal of the Australian Institute of Metals*, 14(4):292–297, 1969.

[109] T. Sakai and J.J. Jonas. Dynamic recrystallization: Mechanical and microstructural considerations. *Acta Metallurgica*, 32(2):189–209, 1984.

[110] C. Saldana, S. Swaminathan, T.L. Brown, W. Moscoso, J.B. Mann, W.D. Compton, and S. Chandrasekar. Unusual applications of machining: controlled nanostructuring of materials and surfaces. *Journal of manufacturing science and engineering*, 132(3):030908, 2010.

[111] T.L. Schmitz, J. Karandikar, N.H. Kim, and A. Abbas. Uncertainty in machining: Workshop summary and contributions. *Journal of Manufacturing Science and Engineering*, 133(5):051009, 2011.

[112] A.J. Schwartz, M. Kumar, B.L. Adams, and D.P. Field. *Electron backscatter diffraction in materials science*, volume 2. Springer, 2009.

[113] A. Seeger and P. Haasen. Density changes of crystals containing dislocations. *Philosophical Magazine*, 3(29):470–475, 1958.

[114] C.M. Sellars and W.J. McTegart. On the mechanism of hot deformation. *Acta Metallurgica*, 14(9):1136–1138, 1966.

[115] J.G. Sevillano and E. Aernoudt. Low energy dislocation structures in highly deformed materials. *Materials Science and Engineering*, 86:35–51, 1987.

[116] J.G. Sevillano and J. Aldazabal. Ductilization of nanocrystalline materials for structural applications. *Scripta materialia*, 51(8):795–800, 2004.

[117] M.R. Shankar, S. Chandrasekar, A.H. King, and W.D. Compton. Microstructure and stability of nanocrystalline aluminum 6061 created by large strain machining. *Acta Materialia*, 53(18):4781–4793, 2005.

[118] M.R. Shankar, B.C. Rao, S. Chandrasekar, W.D. Compton, and A.H. King. Thermally stable nanostructured materials from severe plastic deformation of precipitation-treatable ni-based alloys. *Scripta Materialia*, 58(8):675–678, 2008.

[119] M.C. Shaw and J.O. Cookson. Metal cutting principles, 1985.

[120] S. Shekhar, S. Abolghasem, S. Basu, J. Cai, and M.R. Shankar. Effect of severe plastic deformation in machining elucidated via rate-strain-microstructure mappings. *Journal of Manufacturing Science and Engineering*, 134(3):031008, 2012.

[121] S. Shekhar, J. Cai, S. Basu, S. Abolghasem, and M.R. Shankar. Effect of strain rate in severe plastic deformation on microstructure refinement and stored energies. *Journal of Materials Research*, 26(03):395–406, 2011.

[122] S. Shekhar, J. Cai, S. Lee, J. Wang, and M.R. Shankar. How strains and strain-rates are accommodated by dislocations and twins during chip formation by machining. *Transactions of North American Manufacturing Research Institute/Society of Manufacturing Engineers (NAMRI/SME)*, 37:637–644, 2009.

[123] S. Shekhar, J. Cai, J. Wang, and M.R. Shankar. Multimodal ultrafine grain size distributions from severe plastic deformation at high strain rates. *Materials Science and Engineering: A*, 527(1):187–191, 2009.

[124] S. Shekhar and A.H. King. Strain fields and energies of grain boundary triple junctions. *Acta Materialia*, 56(19):5728–5736, 2008.

[125] L.S. Shvindlerman and G. Gottstein. Grain boundary and triple junction migration. *Materials Science and Engineering: A*, 302(1):141–150, 2001.

[126] G. Subhash, M.A. Meyers, B.K. Kad, and L. Prasad. Evolution of microstructure and shear band formation in a-hcp titanium. *Mechanics of Materials*, 17:318–324, 1994.

[127] S. Swaminathan, M.R. Shankar, S. Lee, J. Hwang, A.H. King, F.K. Renae, B.C. Rao, T.L. Brown, S. Chandrasekar, W.D. Compton, and K.P. Trumble. Large strain deformation and ultra-fine grained materials by machining. *Materials Science and Engineering: A*, 410:358–363, 2005.

[128] J. Tarasiuk, PH. Gerber, and B. Bacroix. Estimation of recrystallized volume fraction from ebsd data. *Acta materialia*, 50(6):1467–1477, 2002.

[129] B.N. Taylor and CH.E. Kuyatt. Nist technical note 1297. *Guidelines for evaluating and expressing the uncertainty of NIST measurement results*, page 24, 1994.

[130] G.I. Taylor. The mechanism of plastic deformation of crystals. part i. theoretical. *Proceedings of the Royal Society of London. Series A, Containing Papers of a Mathematical and Physical Character*, pages 362–387, 1934.

[131] J.W. Taylor. Dislocation dynamics and dynamic yielding. *Journal of Applied Physics*, 36(10):3146–3150, 1965.

[132] N. Theodore. Tensile testing of materials at high rates of strain. *Experimental Mechanics*, 21(5):177–185, 1981.

[133] T.R. Thomas. Characterization of surface roughness. *Precision Engineering*, 3(2):97–104, 1981.

[134] D.M. Turley and L.E. Samuels. The nature of mechanically polished surfaces of copper. *Metallography*, 14(4):275–294, 1981.

[135] R.Z. Valiev. Applications of severe plastic deformations for materials nanostructuring aimed at advanced properties. In *Nanostructured Materials by High-Pressure Severe Plastic Deformation*, pages 29–37. Springer, 2006.

[136] R.Z. Valiev, I.V. Alexandrov, Y.T. Zhu, and T.C. Lowe. Paradox of strength and ductility in metals processed bysevere plastic deformation. *Journal of Materials Research*, 17(01):5–8, 2002.

[137] R.Z. Valiev, R.K. Islamgaliev, and I.V. Alexandrov. Bulk nanostructured materials from severe plastic deformation. *Progress in materials science*, 45(2):103–189, 2000.

[138] R.Z. Valiev and T.G. Langdon. Principles of equal-channel angular pressing as a processing tool for grain refinement. *Progress in Materials Science*, 51(7):881–981, 2006.

[139] R.Z. Valiev, I.P. Semenova, V.V. Latysh, H. Rack, T.C. Lowe, J. Petruzelka, L. Dluhos, D. Hrusak, and J. Sochova. Nanostructured titanium for biomedical applications. *Advanced engineering materials*, 10(8):B15–B17, 2008.

[140] R.Z. Valiev, M.J. Zehetbauer, Y. Estrin, H.W. Höppel, Y. Ivanisenko, H. Hahn, G. Wilde, H.J. Roven, X. Sauvage, and T.G. Langdon. The innovation potential of bulk nanostructured materials. *Advanced Engineering Materials*, 9(7):527–533, 2007.

[141] R.A. Vandermeer and D.J. Jensen. Recrystallization in hot vs cold deformed commercial aluminum: a microstructure path comparison. *Acta materialia*, 51(10):3005–3018, 2003.

[142] Y. Wang, M. Chen, F. Zhou, and E. Ma. High tensile ductility in a nanostructured metal. *Nature*, 419(6910):912–915, 2002.

[143] G.K. White and S.J. Collocott. Heat capacity of reference materials: Cu and w. *Journal of physical and chemical reference data*, 13(4):1251–1257, 1984.

[144] H. Wilman. Abrasion and surface structure. *Wear*, 14(4):249–254, 1969.

[145] A.J.C. Wilson. On variance as a measure of line broadening in diffractometry general theory and small particle size. *Proceedings of the Physical Society*, 80(1):286, 1962.

[146] D. Witkin, Z. Lee, R. Rodriguez, S. Nutt, and E. Lavernia. Al–mg alloy engineered with bimodal grain size for high strength and increased ductility. *Scripta Materialia*, 49(4):297–302, 2003.

[147] G.H. Xiao, N.R. Tao, and K. Lu. Effects of strain, strain rate and temperature on deformation twinning in a cu–zn alloy. *Scripta Materialia*, 59(9):975–978, 2008.

[148] Y.B. Xu, W.L. Zhong, Y.J. Chen, L.T. Shen, Q. Liu, Y.L. Bai, and M.A. Meyers. Shear localization and recrystallization in dynamic deformation of 8090 al–li alloy. *Materials Science and Engineering: A*, 299(1):287–295, 2001.

[149] C. Zener and J.H. Hollomon. Effect of strain rate upon plastic flow of steel. *Journal of Applied physics*, 15(1):22–32, 1944.

[150] F.J. Zerilli and R.W. Armstrong. Dislocation-mechanics-based constitutive relations for material dynamics calculations. *Journal of Applied Physics*, 61(5):1816–1825, 1987.

[151] W.S. Zhao, N.R. Tao, J.Y. Guo, Q.H. Lu, and K. Lu. High density nano-scale twins in cu induced by dynamic plastic deformation. *Scripta materialia*, 53(6):745–749, 2005.

[152] Y. Zhao, T. Topping, J.F. Bingert, J.J. Thornton, A.M. Dangelewicz, Y. Li, W. Liu, Y. Zhu, Y. Zhou, and E.J. Lavernia. High tensile ductility and strength in bulk nanostructured nickel. *Advanced Materials*, 20(16):3028–3033, 2008.

[153] Y.H. Zhao, J.F. Bingert, X.Z. Liao, B.Z. Cui, K. Han, A.V. Sergueeva, A.K. Mukherjee, R.Z. Valiev, T.C. Langdon, and Y.T. Zhu. Simultaneously increasing the ductility and strength of ultra-fine-grained pure copper. *Advanced Materials*, 18(22):2949–2953, 2006.